Novel Hierarchical N-point Polytope Functions for Quantifying, Modeling and Reconstructing Complex Heterogeneous Materials

by

Pei-En Chen

A Dissertation Presented in Partial Fulfillment
of the Requirements for the Degree
Doctor of Philosophy

Approved March 2021 by the
Graduate Supervisory Committee:

Yang Jiao, Co-Chair
Yi Ren, Co-Chair
Yongming Liu
Houlong Zhuang
Qiong Nian

ARIZONA STATE UNIVERSITY

May 2021

ABSTRACT

How to effectively and accurately describe, character and quantify the microstructure of the heterogeneous material and its 4D evolution process with time suffered from external stimuli or provocations is very difficult and challenging, but it's significant and crucial for its performance prediction, processing, optimization and design. The goal of this research is to overcome these challenges by developing a series of novel hierarchical statistical microstructure descriptors called "n-point polytope functions" which is as known as P_n functions to quantify heterogeneous material's microstructure and creating P_n functions related quantification methods which are Omega Metric and Differential Omega Metric to analyze its 4D processing.

In this dissertation, a series of powerful programming tools are used to demonstrate that P_n functions can be used up to n=8 for chaotically scattered images which can hardly be distinguished by our naked eyes in chapter 3 to find or compare the potential configuration feature of structure such as symmetry or polygon geometry relation between the different targets when target's multi-modal imaging is provided. These n-point statistic results calculated from P_n functions for features of interest in the microstructure can efficiently decompose the structural hidden features into a set of "polytope basis" to provide a concise, explainable, expressive, universal and efficient quantifying manner.

In Chapter 4, the P_n functions can also be incorporated into material reconstruction algorithms readily for fast virtualizing 3D microstructure regeneration and also allowing instant material property prediction via analytical structure-property mappings for material design.

In Chapter 5, Omega Metric and Differential Omega Metric are further created and used to provide a time-dependent reduced-dimension metric to analyze the 4D evaluation

processing instead of using P_n functions directly because these 2 simplified methods can provide undistorted results to be easily compared. The real case of vapor-deposition alloy films analysis are implemented in this dissertation to demonstrate that One can use these methods to predict or optimize the design for 4D evolution of heterogeneous material.

The advantages of the all quantification methods in this dissertation can let us economically and efficiently quantify, design, predict the microstructure and 4D evolution of the heterogeneous material in various fields.

ACKNOWLEDGEMENTS

I am sincerely grateful to my advisor Dr. Yang Jiao, for his continued intellectual guidance and care throughout the years, without whom I could not possibly finish this project. I am also pretty grateful to my committees for their numerous help, guidance and advice on my project and research

Besides, I appreciate that I have priceless opportunity to cooperate with Professor Kumar Ankit and Rahul Raghavan. In their major research, I implement all the virtual quantification methods such as P_n functions, Omega Matric and Differential Omega metric into the real cases of film manufacture and simulation. All the results directly proof its universality, accuracy, reliability availability is undoubted.

Furthermore, I also want to appreciate my wife Ching-Yi Huo who sacrifices herself to take care of my kids and look after my family. She always give me immense support and countless encouragement I need. In addition, I want to thank all the team members of Jiao's group as well. I had a perfect experience and enriched learning throughout the years of my staying at Arizona State University because of the extraordinary research team.

Finally, I want to appreciate the God who gave me all his grace to let me finish my research because "his grace is sufficient for me" (Corinthians 12:9). God let me know that "I can do all this through him who gives me strength" (Philippians 4:13). May all the glory be to our highest almighty God!

TABLE OF CONTENTS

Page

LIST OF FIGURES vii

CHAPTER

1 INTRODUCTION AND OVERVIEW 1

1.1 Introduction of Heterogeneous Materials 4

1.2 Quantification of the Microstructure via Advanced Imaging 6

1.3 Reconstruction of Heterogeneous Materials 10

1.4 Summary of the Project 12

1.4.1 Introducing the N-Point Polytope Functions (P_n Functions) 12

1.4.2 Explaining the Utility and Verifying the Reliability of the P_n Functions 13

1.4.3 How to Use the P_n Functions to Execute the Reconstruction of the Complex Heterogeneous Materials. 14

1.4.4 Verifying the Reliability and Precision Result of Reconstruction. 14

1.4.5 P_n Functions' Application for Coupling Simulations and Experiments 16

2 STRUCTURAL QUANTIFICATION FOR HETEROGENEOUS MATERIAL AND ITS MICROSTRUCTURE EVOLUTION 17

2.1 Introduction of Correlation Functions 17

2.1.1 Conventional Statistical Microstructural Descriptors-Definition of the Correlation Functions 17

2.1.2 Two-Point Correlation Function 20

2.1.3 Lineal-Path Function 22

2.1.4 Two-Point Cluster Function 23

CHAPTER Page

2.2 The Introduction of N-Point Polytope Functions (P_n Functions) 24

3 P_n FUNCTIONS' PROCEDURE AND ITS APPLICATION 28

3.1 Computing P_n Functions from Imaging Data 29

3.2 Information Content of P_n Functions Based on Model Microstructures 33

3.2.1 P_n Functions for Separated Sphere Model 33

3.2.2 P_n Functions for Triangle Particles with Different Orientation and Arrangement. 34

3.3 Quantifying Microstructure of Heterogeneous Materials via P_n Functions 40

3.3.1 Quantification of Complex Microstructures 40

3.3.2 Quantification of Microstructure Evolution 45

3.4 Conclusions and Discussion of P_n Functions 48

4 MICROSTRUCTURE RECONSTRUCTION PROCEDURE AND ITS APPLICATION BASED-ON GIVEN P_n FUNCTION 50

4.1 Realization Rendering via Stochastic Optimization 51

4.2 Realization of Reconstruction of Simplified Model 55

4.3 Information Content of P_n Functions via Realization Rendering 58

4.3.1 Ordered Packing of Congruent Spheres 60

4.3.2 Disordered Packing of Congruent Spheres 62

4.3.3 Overlapping Congruent Spheres 65

4.3.4 Concrete Microstructure 67

4.3.5 Interpenetrating Metal-Ceramic Composite 69

4.4 Conclusions and Discussion of Reconstruction 71

CHAPTER Page

5 APPLICATO OF P_n FUNCTIONS FOR VAPOR-DEPOSITION ALLOY FILMS 73

5.1 The Procedures to Create Semiconductor 74

5.2 The Studies and Important Factors for Phase-Separating Films Making..... 77

5.2 The Basis of Simulation of Phase-Separating Alloy Films. 78

5.3 The Results and Conclusions of Simulation and Experiment. 80

5.4 Using P_n Functions to Couple Related Simulations and Experiments..... 86

5.5 Using Reduced-Dimension Methods to Efficiently Quantify 4D Evolution..... 88

5.5.1 The Concept of Omega Metrix 89

5.5.2 The Formula of Omega Metrix 91

5.5.3 The Analysis Results of Omega Metric of Vapor-Deposition of Phase-Separating Alloy Film. 91

5.5.3 Differential Omega Matric. 96

6 DISCUSSION AND FUTURE WORK..... 98

REFERENCES..... 101

LIST OF FIGURES

Figure Page

1. 1 Schematic Illustration of a Two-Phase Heterogeneous Material With General Phase Properties K_1 and K_2 and Phase Volume Fraction $\Phi 1$ and $\Phi 2$. 5

1. 2 Probability Map of Imaging. (The Black Pixels Are Interested Phase and They Are Set As the Value of 1. The Descriptors Within The Triangle Are Assigned the Valued of 1.) 13

1. 3 Schematic Illustration of the Difference Between $L(r)$ and P_2 Function. 15

2. 1 Schematic Illustration of the S_3 (R1, R2 and R3 Are Distance From A to B, B to C and C to A Point Respectively. They Don't Need to Be Given the Same Value.) 19

2. 2 Schematic Illustration of the Events That Contribute to Various Correlation Functions. The Two-Point Correlation Function S_2 Gives the Probably of Finding Two Points in the Phases of Interest. In (A), We Show Events That Contribute to $S_2(ij)$, Where i, j Can be Either Red Phase or Blue Phase. The Lineal-Path Function $L(r)$ Gives the Probability That a Randomly Chosen Line Segment of Length r Entirely Falls into The Phase of Interest. In (B), We Show Events That Contribute to $L(i)$. The Two-Point Cluster Function $C2$ (r) Gives the Probably of Finding Two Points Separated by r In The Same Cluster of The Phase of Interest. In (C), We Show Events That Contribute to $C2$ (i). 21

Figure Page

2. 3 (a) Schematic Illustration of Stochastic Events Contributing to the P_n Functions in the Case of Regular Polygons. (b) Examples of Regular Polygons (Triangle, Square, Pentagon, Hexagon, and Decagon) and Polyhedra (Including the Platonic Solids P1-P5, and Archimedean Solids A1-A13) For Computing the P_n Functions. 26

2. 4 The Tendency of the P_n Functions. 27

3. 1 Schematic Illustration of the Key Components of X-Ray Tomography and an Illustration of a 2D Projection of a 3D Hard Sphere Packing Structure. Different Colors in the 2D Projection Represent Different Attenuated Intensities. 29

3. 2 Schematic Illustration of Periodic Boundary Condition. 31

3. 3 Schematic Illustration of Different Sampling Templates for Computing P_n Functions (in the Case of n=3) From Images: (a) Directional Sampling, in Which Only the Location of the Template Is Randomly Selected. (b) Isotropic Sampling, in Which Both the Location and Orientation of the Polygon Template Are Randomly Selected. 32

3. 4 Schematic Illustration of P_2-r Curves. 34

Figure Page

3. 5 (a) Model Microstructures Composed of Congruent Equilateral Triangle Particles With Different Orientations Arranged on a Square Lattice. The Resolution of the Images Is 1048 by 1048 Pixels. (b) Directional 3-Point Polytope Functions P_3 for the Model Microstructures Associated With Vertically Oriented Triangular Sampling Templates. (c) Directional 3-Point Polytope Functions P_3 for the Model Microstructures Associated With Horizontally Oriented Triangular Sampling Templates. (d) 4-Point Polytope Functions P_4 for the Model Microstructures. (e) 6-Point Polytope Functions P_6 for the Model Microstructures. The Unit of Distance Is One Pixel Length. 36

3. 6 (a) Model Microstructures Composed of Congruent Equilateral Triangle Particles With Different Orientations Arranged on A Triangular Lattice. The Resolution of the Images Is 1048 by 1048 Pixels. (b) Directional 3-Point Polytope Functions P_3 for the Model Microstructures Associated With Vertically Oriented Triangular Sampling Templates. (c) Directional 3-Point Polytope Functions P_3 for the Model Microstructures Associated With Horizontally Oriented Triangular Sampling Templates. (d) 4-Point Polytope Functions P_4 for the Model Microstructures. (e) 6-Point Polytope Functions P_6 for the Model Microstructures. The Unit of Distance Is One Pixel Length. 38

3. 7 (a) 2D Microstructure Composed of Equal-Sized Hard Spheres in a Matrix. (b) The P_n Functions for the Particle Phase with n =2, 3, 4, 6 and 8. (c) The Corresponding Rescaled f_n Functions Highlighting the Spatial Correlations (c.f. Eq. (2.11)).....40

Figure Page

3. 8 (a) 2D Microstructure Composed of Equal-Sized Overlapping Spheres in a Matrix. (b) The P_n Functions for the Particle Phase With n =2, 3, 4, 6 and 8. (c) The Corresponding Rescaled f_n Functions Highlighting the Spatial Correlations (c.f. Eq. (2.11)). 41

3. 9 (a) 2D Image of a Concrete Microstructure Composed of Reinforcement Rocks (Shown in Black) and the Cement Paste (Shown in White). (b) The P_n Functions for the Rock (Black) Phase with n =2, 3, 4, 6 and 8. (c) The Corresponding Rescaled f_n Functions Highlighting the Spatial Correlations (c.f. Eq. (2.11)). 42

3. 10 (a) 2D Image of A Fontainebleau Sandstone Microstructure Composed of the Rock Phase (Shown in Black) and the Pore Phase (Shown in White). (b) The P_n Functions for the Rock (Black) Phase with n =2, 3, 4, 6 and 8. (c) The Corresponding Rescaled f_n Functions Highlighting the Spatial Correlations (c.f. Eq. (2.11)). 43

3. 11 (a) 2D Image of an Interpenetrating Metal-Ceramic Composite Microstructure Composed of the Boron-Carbide Phase (Shown in Black) and the Aluminum Phase (Shown in White). (b) The P_n Functions for the Boron-Carbide (Black) Phase with n =2, 3, 4, 6 and 8. (c) The Corresponding Rescaled f_n Functions Highlighting the Spatial Correlations (c.f. Eq. (2.11)). 44

3. 12 Representative Microstructures of the Lead-Tin Alloy (Pb37Sn63) at 175 ^{o}C for Different Times. The Dark Region Represents Lead-Rich Phase and White Region Represents Tin-Rich Phase. The Linear Size of the Microstructure Is 100 μm. The Resolution of the Image Is 600 by 600 Pixels. 45

Figure Page

3. 13 The P_n Functions Associated With the Pb-Sn Alloy Microstructures at Different Aging Times. 46

4. 1 Schematic Illustration of the Pixel Exchange Procedure for Generating A New Microstructure Based on An Old Microstructure. 53

4. 2 Schematic Illustration of the Simulated Annealing Optimization Procedure for Reconstruction. The Initial Uphill Moves Allow the System to Escape from Local Energy Minimum. 53

4. 3 Illustration of the Different Shapes of the Sampling Templates for the P_n Functions With Various Value n. 55

4. 4 Reconstruction Results of Imaging Which Contain Single (a) Equilateral Tringle, (b) Square, (c) Regular Hexogen and (d)Regular Octagon Particles by Using Their Related P_3, P_4, P_6, and P_8 Separately. 56

4. 5 Reconstruction Results of Figure 4. 4 (b) Under Periodic Boundary Conditions. 57

4. 6 Reconstruction Results of Figure 4. 4(d) Under Periodic Boundary Conditions. 58

4. 7 A simple 2D Crystalline Packing of Congruent Spheres on A Square Lattice (Left) and the Associated P_n Function for the Particle Phase (Right). 60

4. 8 Realizations of 2D Crystalline Packing of Congruent Spheres on A Square Lattice (Upper Panels) and the Associated Lineal-Path Functions (Lower Panels) Obtained via Stochastic Reconstruction by Successively Incorporating Higher-Order P_n Functions. The Functions Incorporated from Left to Right Are Respectively: P_2, $\{P_2, P_3\}$, $\{P_2, P_3, P_4\}$, $\{P_2, P_3, P_4, P_6\}$, and $\{P_2, P_3, P_4, P_6, P_8\}$. 60

Figure Page

4. 9 Accuracy Metric ψ Defined in Eq. (4) Associated with Reconstructions Incorporating Different Sets of P_n Functions. The Horizontal Axis Indicates the Number of Functions Incorporated in the Reconstruction. 61

4. 10 A 2D Disordered Packing of Congruent Hard Spheres Generated via Monte Carlo Simulations (left) and the Associated P_n Function for the Particle Phase (Right). 62

4. 11 Realizations of Disordered Packing of Congruent Hard Spheres (Upper Panels) and the Associated Lineal-Path Functions (Lower Panels) Obtained via Stochastic Reconstruction by Successively Incorporating Higher-Order P_n Functions. The Functions Incorporated from Left to Right Are Respectively: P_2, $\{P_2, P_3\}$, $\{P_2, P_3, P_4\}$, $\{P_2, P_3, P_4, P_6\}$, and $\{P_2, P_3, P_4, P_6, P_8\}$. 63

4. 12 Accuracy Metric ψ Defined in Eq. (4) Associated with Reconstructions Incorporating Different Sets of P_n Functions. The Horizontal Axis Indicates the Number of Functions Incorporated in the Reconstruction. 64

4. 13 A 2D Disordered Packing of Congruent Overlapping Spheres With a Poisson Distribution of the Particle Centers (Left) and the Associated P_n Function for the Particle Phase (Right) 65

4. 14 Realizations of Overlapping Sphere Packing (Upper Panels) and the Associated Lineal-Path Functions (Lower Panels) Obtained via Stochastic Reconstruction by Successively Incorporating Higher-Order P_n Functions. The Functions Incorporated from Left to right Are Respectively: P_2, $\{P_2, P_3\}$, $\{P_2, P_3, P_4\}$, $\{P_2, P_3, P_4, P_6\}$, and $\{P_2, P_3, P_4, P_6, P_8\}$. 66

Figure Page

4. 15 Accuracy Metric ψ Defined in Eq. (4) Associated with Reconstructions Incorporating Different Sets of P_n Functions. The Horizontal Axis Indicates the Number of Functions Incorporated in the Reconstruction. 67

4. 16 A 2D Slice of a Concrete Microstructure in Which the Cement Paste Is Shown in White and the Rocks Are Shown in Black (Left) and the Associated P_n Function for the Rock Phase (Right).....67

4. 17 Realizations of Concrete Microstructures (Upper Panels) and the Associated Lineal-Path Functions (Lower Panels) Obtained via Stochastic Reconstruction by Successively Incorporating Higher-Order P_n Functions. The Functions Incorporated from Left to Right Are respectively: P_2, $\{P_2, P_3\}$, $\{P_2, P_3, P_4\}$, $\{P_2, P_3, P_4, P_6\}$, and $\{P_2, P_3, P_4, P_6, P_8\}$. 68

4. 18 Accuracy Metric ψ Defined in Eq. (4) Associated with Reconstructions Incorporating Different Sets of P_n Functions. The Horizontal Axis Indicates the Number of Functions Incorporated in the Reconstruction. 69

4. 19 A 2D Slice of A Interpenetrating Microstructure of a Metal-Ceramic Composite Composed of the Boron-Carbide Phase (Black) and the Auminum Paste (White) (Left) and the Asociated P_n Function for the Boron-Carbide (Ceramic) Paste (Right).....69

Figure Page

4. 20 Realizations of the Interpenetrating Microstructure (Upper Panels) and the Associated Lineal-Path Functions (Lower Panels) Obtained via Stochastic Reconstruction by Successively Incorporating Higher-Order P_n Functions. The Functions Incorporated from Left to Right Are Respectively: P_2, $\{P_2, P_3\}$, $\{P_2, P_3, P_4\}$, $\{P_2, P_3, P_4, P_6\}$, and $\{P_2, P_3, P_4, P_6, P_8\}$. 70

4. 21 Accuracy Metric ψ Defined in Eq. (4) Associated With Reconstructions Incorporating Different Sets of P_n Functions. The Horizontal Axis Indicates the Number of Functions Incorporated in the Reconstruction. 71

5. 1 The Flow Chart of Fabrication of Semiconductor.....74

5. 2 Schematic Illustration of Vapor Disposition' Equipment.....75

5. 3 Schematic Illustration of the State Cycle of the Vapor-Decomposition Material. 75

5. 4 Schematic of Simulated Vapor Deposition of Phase-Separating Alloy Film With Steep Protuberances. (a) Protuberances Are Spherical With r = 17Δx. (b) Boundary Conditions Assumed Are Periodic Along x and y Axes, and No-Flux Along the Deposition Axis.....80

5. 5 Distinct Hillock Nanostructures that Evolve During Vapor Deposition of Phase Separating Alloy Film Depending on the Seed Morphology. (a) A Representative Volume of the Film Showing A Disconnected Hillock When Deposition Simulations Are Initialized from a Perturbed Seed That Comprises of Vertical Concentration Modulations. (b) Connected Hillocks That form When Deposition Simulations Are Initialized from a Random Seed, and (c) Segmented Film with Symmetrical Hillocks That form at Narrow Contact Angles When the Seed morphology is same as (a). ..81

Figure Page

5. 6 Simulated Vapor Deposition from An Initial Hillock Seed Condition for Protuberation Radius of 17 Δx and a Preset Contact-Angle ≈ 0◦ at Different Time-Steps (a) t=12, (b) t=612, (c) t=1212, (d) t=1812, and (e) t=2412.....82

5. 7 Simulated Vapor Deposition from an Initial Hillock Seed Condition for Protuberation Radius of 17 Δx and a Preset Contact Angle ≈ 47◦ at Different Time-Steps (a) t=12, (b) t=612, (c) t=1212, (d) t=1812, and (e) t=2412.....83

5. 8 Simulated Vapor Deposition from An Initial Hillock Seed Condition for Protuberating Radius of 17 Δx and a Preset Contact Aangle ≈ 63◦ at Different Time-Steps (a) t=12, (b) t=612, (c) t=1212, (d) t=1812, and (e) t=2412.....84

5. 9 Simulated Vapor Deposition from a Random Seed Condition at Contact Angles (a)≈0◦, (b)θ≈47◦, and (c) θ≈63◦.....85

5. 10 Quantification of Evolving Patterns of the Deposited Thin Film via Polytope Functions. The Functions Associated With Segmented Blue Phase Morphologies Are Computed from the Simulated Thin Film Samples for Three Contact Angles, (a) θ=0◦, (b) θ=47◦ and (c) θ=63◦. The Analyses Reveal Universal Hidden Correlations Across All Angles and All Times, Manifested as the Coinciding Length-Scales Associated with Peaks in the Functions.....87

5. 11 Quantification of the Morphology of the Deposited Films Resulted from Random Seeds Using the 2-Point Function P_2. 88

5. 12 The Concept of Omega Metric.....90

5. 13 The Results Shown the Evolution for Theta= 0 case. It Turns Out That the Omega n for Different n Yield Consistent Measure of the Microstructural Space. 92

Figure Page

5. 14 The Image of Every Limit point at Domain from Time=8 to Time=80. 93

5. 15 The Tendency of Curves. 94

5. 16 The Decreasing Tendency of Curves of Film at Different Angles. 94

5. 17 The Curve Tendency Results of Omega Metric Which Use Connected Image as the Reference Image 95

5. 18 The Tendency of Curves of DOM for Vapor-Deposition Film at Angle=0. 97

CHAPTER 1

INTRODUCTION AND OVERVIEW

One can pervasively find the heterogeneous material in nature such as polycrystals, and sandstone. Besides, lots of organism such as tooth, skin, bone, wood, and bamboo also belong to heterogeneous material. The characteristics of these organism is that they are composed with the strongest structure in some special area where often afford more force rather than other area. This is the outcome of revolution and optimization to let them can be evolved to burden more loading. That is why the progressed organism can reduce the probability of damage to sustain and survive in the severe environment.

With the advent of advanced science and technology, more and more heterogeneous materials were created for engineering application because they have more better and remarkable physical properties compared to the homogenous material. This process is similar to the evolution of organism. In fact, because heterogeneous materials play a significant role in these day, it attracts more and more people to analyze and research their characteristics and unique. Unlike homogeneous materials, heterogeneous materials are nor evenly composed or structured. One can easily changing its contained phases' arrangement and directional orientation, and its geometric structure during manufacture process to obtain pretty different material properties [1][20][70][80]. By repeating the procedures, one can create and design the most prosper heterogeneous material for specific use. Since this customized material can be used for miscellaneous purposes. However, it goes without saying that these repeating procedures are very sophisticated and arduous but the occurred benefits are tremendous for whole human beings. These days, so many novel heterogeneous materials are utilized in aircraft design and vehicle industry to boost up the durability of their product and cost down their cost. These are the best cases to be illustrated.

In the other words, from last paragraph, we can find out that the configuration of an object plays an important role for heterogeneous material. But how to accurately and technological compare and describe the configuration of it becomes a very essential and challenging question because it can help us to proverb and design the required material with designed material property in the future. How to quantify the microstructure is the most essential and fundamental part of material design. In order to obtain the most accurate and universal quantification results which can be further used for reliable material design, in this dissertation, I will focus on how to develop a series of precise quantification methods to quantify the configuration.

For a simple or not complicate model, one can easily discern and describe its structural characteristics but for a sophisticated one, it's impossible to tell and distinguish its structure from others. Especially, when it contain more than two phases. Since different material structure with assorted phase arrangement has different material properties, if we can completely quantify the heterogeneous materials, we can not only easily compare the different microstructures between several materials but also design the wanted heterogeneous materials.

Actually, in this dissertation, I will use a novel method to decompose the geometric information. Even more, I can reconstruct it from its most ideal organization to design the optimal material which is suitable for expected circumstance.

To express the multi-function and versatility of P_n functions, I will also use membrane generation as an example to illustrate that quantification method of P_n functions are valid and cogent tool to proof that not only 4D results of microstructures of different objects can be collated each other, but also the results and periodic pattern of the membrane's generation can be analyzed. From all the results of membrane cases, we can apply P_n functions to various

fields which cannot distinguished by our naked eyes. In fact, P_n functions do are very efficient and accurate tool which can decompose and organize images into a series of data set.

Before I start to introduce the n-point polytope functions, I would like to introduce the heterogeneous materials and the related information about its calculation.

1.1 Introduction of Heterogeneous Materials

As we have mentioned before, unlike homogeneous material, a heterogeneous material is composed of assorted materials or different phases, i.e. microstructure, such as concrete which is combined with cement, sand, stone, etc. or the same material in different states such as a polycrystalline which is composed of many crystallites of varying size and orientation. That is why, under the generally circumstance, two man-made materials which contain same content, same processing procedure but different in their microstructure may have opposite or different material properties. Since heterogeneous materials do not have uniform composition and configuration, it will let its application becomes more sophisticated.

Owing to its non-uniform composition and configuration characteristics, the manufactured one can be designed for specific use or purpose for various products with more benefits. Taking a bullet-proof vest for example, when designers design it, the designer's only concern is the bullet resistant ability of its normal direction. The designed product's lateral parts does not need to endure the same resistance of normal direction when bullet impacts it, so it can be designed thinner to get more flexibility by optimizing the arrangement of Kevlar fiber . Light weight and ergonomics/flexibility are very important factors of bullet-proof vest for the vest user. Heterogeneous material application does not only offer more benefits for user but also benefit the entrepreneur as well because of its low cost character. That is why heterogeneous materials are popular and prevail for industry application.

Generally speaking, Heterogeneous materials normally focus on the study in microscopic length scale, which is much larger than the molecular dimension, but much smaller than the size of length scale of a macroscopic sample. In such circumstances, a heterogeneous material can be viewed as a continuum on the microscopic scale, subjected to

classical analysis, and maintain macroscopic properties simultaneously as shown in Figure 1. 1. Typical examples can be easily found in synthetic materials, i.e., fiber and particulate composites, and natural environment, i.e. bones, tissue, sandstone, etc.

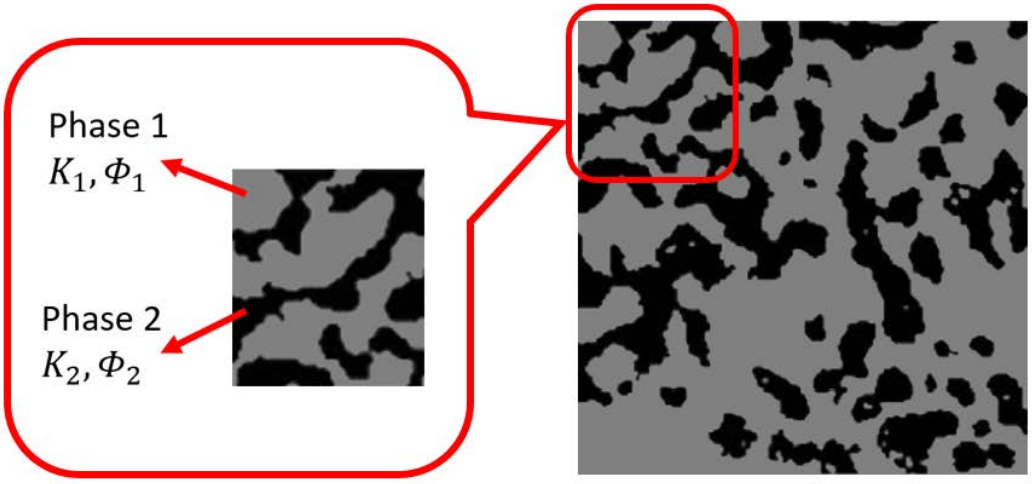

Figure 1. 1 Schematic Illustration of a Two-Phase Heterogeneous Material With General Phase Properties K_1 and K_2 and Phase Volume Fraction Φ_1 and Φ_2.

It is easy to imagine that an entity can change its material properties by altering its configuration or its geometric composition. Taking an arch bridge and honey-comb plate for example, the arch bridge and honey-comb plate can suffer higher loading than general bridge and solid flat plate because arch shape can distribute the loading more efficiently and hexagon configuration has more durability because its geometric configuration. When the heterogeneous material was researched with microscopic length scale, the conclusion shows that its physical properties and performance of heterogeneous materials are determined by their complex microstructures and how such microstructures evolve under various external stimuli [1][2]. Traditionally, the study of material microstructure has been limited by two dimensional (2D) imaging techniques. It frequently occurred the inaccurate or inadequate results of solving many cutting-edge problems and all the calculation procedures are laborious

and time-consuming. With the advent of advances in experimental methods, analytical techniques, and computational approaches enabled the development of three dimensional (3D) analyses to be executed [3]. In the following paragraph, I will relate about how to describe and quantify the microstructure of heterogeneous materials.

1.2 Quantification of the Microstructure via Advanced Imaging

Since different structures and configurations of heterogeneous material can seriously offer various material properties [1], that is why quantification is so crucial for heterogeneous material because the researcher can compare and distinguish the difference between materials which contain the same contents to consider which one will be used for certain situation through the result of quantification's results.

The procedure of quantification in this dissertation is that one need to obtain images such as X-ray results or objects' cross-section images or just several similar pictures first, then transfer all the interesting images into digitalized matrix and finally use quantification method to decompose all the matrixes of microstructures into diagrams or data sets. In such situation, one can efficient research the microstructure and configuration of different objects.

One need to acquire object's image to start to calculate its quantification results. For getting image part, before the advanced imaging technology was progressed, how to get an in situ characterization of the 3D microstructure containing features of interest on multiple length scales and the 4D evolution processes (3D microstructure plus temporal evolution) are actually impossible. This challenge has been partially solved by the improved development and successful application of advanced non-destructive in situ imaging techniques, such as x-ray micro-computed tomography [9][10]. Additionally, because of development of technology of the advanced imaging such as x-ray tomography microscopy, one can be easily allowed to

obtain detailed morphological feature data with sub-micrometer resolution and investigate microstructural evolution in situ under different external stimuli with different time these days [4]-[8].

Nowadays, X-ray tomography has already improved to a matured phase. X-ray tomography is a convenient, economic, non-destructive technique for characterizing microstructure in 3D and 4D [49][50][51]. X-ray tomography use extremely high brilliance and partially coherent synchrotron light to allow one to image multi-component materials from the sub-micrometer to nanometer range. X-ray tomography can be conducted in imaging modes based on light absorption or phase contrast. One can easily adjust small angular increments to obtain the interested 2D projections to proceed quantification process.

Not only imaging technology has boosted but quantitative method has grown by leaps and bounds as well. The improvement of quantitative method plays a vital role for heterogeneous material because how to accurately quantifying the microstructure of a heterogeneous material from obtainable image data is very crucial for its analysis and optimization design. For this purpose, several structure quantitative schemes and methods have been developed to overcome the challenges.

Basically, quantitative method is a mathematical frameworks and computational processes for quantitative representation, modeling and reconstruction of complex heterogeneous material microstructures and their evolution. From its results and diagrams, we can thoroughly control its construction and configuration status. Recently, quantitative microstructure representation (QMR) has been identified as a key technical gap in core areas of "Coupling Simulations and Experiments" and "Digital Representation and Visualization" [11]. Besides, a descriptor-based representations, a Hierarchical Materials Informatics, based on complete 2-point statistics and its lower dimensionally algorithmic method [12][13][14], can

accurate estimates of material properties [15]-[23] and thus, has been incorporated into various integrated computational material design frameworks. The representations of complete 2-point statistics for frameworks such as "low dimensional projections of the complete 2-point statistics space" and "the image-based decompositions" which are usually adopted to cope with very abstract and challenging cases which cannot be visualized and interpreted physically can be represented effectively and successfully in achieving conciseness, expressiveness and universality.

Another widely used descriptor-based representations involves the standard n-point correlation (or probability) function Sn, which provides the probability of occurrence of arbitrary n-point configurations in the material microstructure [1][24]-[26]. The complete set of Sn with n from 1 to infinity provides a concise quantitative microstructure representation which can thoroughly describe the physical properties and performance of the material system under external stimuli. The lower order function S_2 even can be employed to calculate a wide spectrum of different heterogeneous material systems [27]-[34]. In practice, it is very challenging to utilize Sn with $n \geq 3$ because arbitrary n-point means that millions of permutations should be considered. To put it another way, one needs to enumerate all distinct n-point configurations then can efficiently compute and store their probability of occurrence. It is pretty expensive and time-consuming for computer and computer cluster to execute n-point correlation (or probability) function because Sn's statistical data set results are typically much larger in size than S_2's outcomes.

Additionally, an alternative and auxiliary approach also used in this dissertation is non-standard lower-order correlation functions such as the cluster functions [35][36] or surface functions [37][38], which can be encoded to analyze the connected construction of interesting

phase in material. Although these two functions do not belong to stand n-point correlation function and only have the property of lower order correlation function by their original definition, these methods are very effective in capturing specific morphological features for clustering configuration to offer supplemental data of representation [39] but its results cannot be allowed to systematically incorporate hierarchical higher order structural information for microstructure quantification.

In this dissertation, it develops a set of novel hierarchical statistical microstructural descriptors, called the "n-point polytope functions" P_n, which use n-point regular polygon calculation model rather such as regular triangle, square and regular pentagon rather than any arbitrary n-point calculation model to calculate the target's imaging. Its conciseness, expressiveness, universality and interpretability for quantitative characterization, representation of configuration, and modeling of microstructural evolution during processing can proof it's an accurate and reliable quantitative method. P_n functions successively include higher-order n-point statistics of the features of interest in the microstructure, and can be directly computed from multi-modal imaging data, including x-ray tomographic radiographs, optical/SEM/TEM micrographs, and EBSD color maps for quantification of different features of interest.

In particular, the developed P_n functions is an efficient computational tools which can directly extract the statistical descriptors from multi-modal images to quantify different types of structural features and their evolution. Furthermore, we apply this functions to quantify and model for a variety of heterogeneous material systems, including particle-reinforced composites, metal-ceramic composites, concretes, porous materials; as well as the microstructural evolution in an aged lead-tin alloy. Our results indicate that the P_n functions can offer a practically complete, concise and accurate sets of basis for quantitative

microstructure representation (QMR) about both static 3D complex microstructure and 4D microstructural evolution of a wide spectrum of heterogeneous material systems.

1.3 Reconstruction of Heterogeneous Materials

Actually, the detailed and exactly results of correlation functions are powerful and useful information for heterogeneous material design. Different results of P_n functions of objects represent objects' different characteristics such as some object has higher yield stress in certain direction because it has more square microstructure. For this reason, the research can deduce and derive a required and proper P_n functions of the new heterogeneous material for certain need during its design phase. When the new heterogeneous material's P_n functions is confirmed, we can use the reconstruction skill to reverse it real configuration and microstructure in advance. These processes are really significant for heterogeneous material design. So if we can proof our reconstruction results are correct and valid, we can make huge progresses for material design field.

In the past decade, lots of researchers have been focused on conductivity estimation and material design with desired and supposed physical properties [67]-[70]. All these researchers were proposed using spatial correlation functions and strong contrast expansion formulism (SCE) to analyze the property of material. Besides, the directly extracting n-point correlation functions from limited x-ray tomography data were also used to immediately estimate the physical properties of the material of interest from limited data, once the corresponding properties of individual phases are known [[1][71][72].

From the past studies, we can know that an effective reconstruction procedure enables one to create and reverse blueprint of an object's real structures at will from its deduced P_n functions before it will be manufactured and its subsequent analysis can make sure that the

created materials can furnish designed material properties and microstructures of the interesting target. It will be helpful for material engineers to save time and cost down the cost to generate novel materials.

However, the most difficult challenge of reconstruction is that obtaining the accurate reconstructions of heterogeneous materials is so demanding because it is clear that even if the correlation functions of the reference and reconstructed systems are in good agreement, this does not ensure that the reconstructed structures of these two systems will match very well. However, the procedure of reconstruction in this dissertation overcomes all the challenges and can be used as a reliable method to forecast the real configuration from a designed object's P_n functions.

In this dissertation, reconstruction procedures are presented to reconstruct the structure for general random heterogeneous materials from a set of data which is calculated and acquired from real object's P_n functions for QMR. I will illustrate that the results of reconstruction method reconstructed from an object's P_n functions is efficient and valid by demonstrating the simulation results. After comparing the actual and reconstructed structure, a valid and reliable reconstruction structure can be acquired by using a reconstruction procedures which can be utilized with the data set of P_n function to benefit relating heterogeneous material design and analysis.

1.4 Summary of the Project

1.4.1 Introducing the N-Point Polytope Functions (P_n Functions)

In this dissertation, I will exhibit the ideals and functions of the hierarchical n-point polytope functions (P_n functions) which are the subset of spatial correlation functions. P_n functions allows one to directly extract key structural information from limited and chaotic x-ray tomographic data or similar images. Compared to the traditional "standard spatial correlation functions", this descriptor really can provide an efficient and valid way to quantify the sophisticated structure of heterogeneous materials without losing its original characteristics of generality and universality. In other words, P_n functions can be widely performed and adopted in assorted fields (e.g. medical experiment to distinguish if the sample cell is Malignant tumor or not, biological tissue comparison to determine if the samples are related or not, Material design optimization to predict the future created material will be the required material or not. and etc.) to quantify and compare the immethodical structure of various materials.

The key component of our procedure to use P_n functions is the computation of a "probability map", which is a digital data set can be obtain by transforming from the topology projections (e.g. X-ray tomography) and shown as Figure 1. 2. In this dissertation, I set the interested phase as value of 1 and the other phase is set as value of 0. By selecting the interested phase, probability map which only contains value of 1 and 0 can be utilized to calculate the probability of an arbitrary point in the material system for the interested phase.

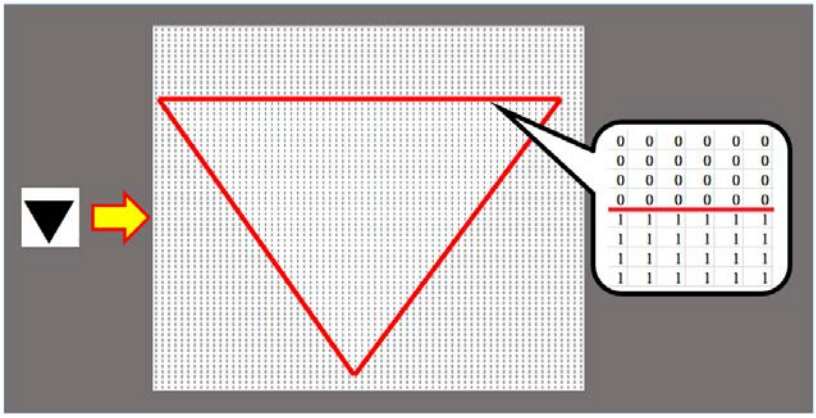

Figure 1. 2 Probability Map of Imaging. (The Black Pixels Are Interested Phase and They Are Set As the Value of 1. The Descriptors Within The Triangle Are Assigned the Valued of 1.)

Therefore, the correlation functions of interest are then readily computed from the transformed probability map, based on their probability interpretations. The utility of our procedure illustrated by P_n functions (e.g. P_2, P_3, P_4, P_6, and P_8) to analyze heterogeneous materials from simple morphologies such as the congruent spheres which are randomly overlapped or orderly latticed to complicate structures such as concrete microstructure, metal-ceramic composite, and lead-tin alloy in chapter 2. Besides, in chapter 2, I will also introduce the basis and algorisms of P_n functions.

1.4.2 Explaining the Utility and Verifying the Reliability of the P_n Functions.

Why P_n functions is so useful and powerful? Actually, when gathering all the results of P_n functions from programming, I notice that a lot of hidden information (e.g. symmetric arrangement, periodicity pattern, average size of morphologic grain/ligament, etc.) can be categorized through results of related curves.

Taking Figure 2. 4 for example, One can easily distinguish the each curve's feature of curvature, oscillation, decreasing/increasing tendency, peak value, convergent altitude, etc. to realize further uncovered structure of the target. What factors effect and cause the tendency

of curve? In fact, these obvious and explicit tendencies are developed by the various features of microstructure which are not easy to be observed by our naked eyes. By using probability-based P_n functions, I can easily sift these hidden and arranged information. In the chapter 3, I will discuss all the physical meaning for every curve's tendency for simplified and its real application the thin film.

1.4.3 How to Use the P_n Functions to Execute the Reconstruction of the Complex Heterogeneous Materials.

In this dissertation, I will use the calculated data sets of P_n functions of real objects' imaging and Yeong-Torquato (YT) procedure to render material realizations via stochastic optimization [61][62]. Actually, reconstruction from real object's P_n functions is relatively complicated processes because it has innumerable permutation to reconstruct its original microstructure. By using YT procedure, this energy-optimization algorism can try to find macrostructure's lowest energy point by let the lowest energy point escape from the local minimal energy point which usually trap the reconstruction procedure and lead to an unfavorable reconstruction result.

Generally speaking, an acceptable and reasonable result can be derived from YT procedure. This achieve has magnificent contribution in assorted field to research or design better materials without prodigal time and expense. The whole reconstruction procedure, algorism and basis are related in chapter 3.1.

1.4.4 Verifying the Reliability and Precision Result of Reconstruction.

After the reconstruction procedure is completed, an appraisal will be executed to examine the accuracy and validity of reconstruction results. Sometimes, I can directly tell some morphological feature such as interested particle's shape, the dispersion of particle, and the connectivity of particle/ligament by our naked eye for simple case. However, disordered

systems are ubiquitous in physical, biological and material sciences. Examples include liquid and glassy states of condensed matter, colloids, granular materials, porous media, composites, alloys, packings of cells in avian retina and tumor spheroids, to name but a few. Under this complicated circumstance, our naked eyes may be useless. That is why I try to find a statistical morphological descriptors (i.e. the lineal-path function) to examine the accuracy and validity of reconstruction structure by a more scientific way.

The lineal-path function $L(r)$ [39][73], which provides the probability that a randomly placed line segment of length r entirely lying in the phase of interest. The difference between $L(r)$ and P_2 function shown as Figure 1. 3 is that a line segment which is continuously connected is thrown into probability map for $L(r)$ rather than 2 arbitrarily non-connected points for P_2 function. That is why the lineal-path function is sensitive to cluster particle because of its property of connectivity.

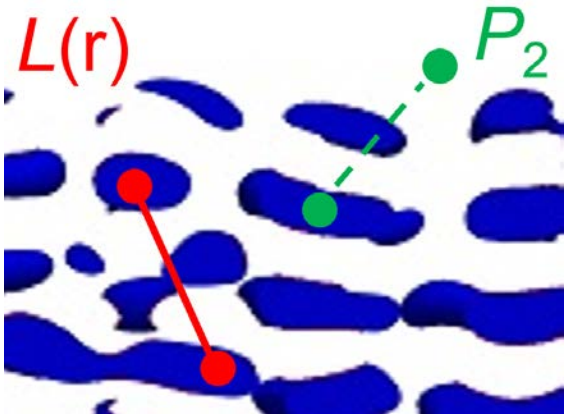

Figure 1. 3 Schematic Illustration of the Difference Between $L(r)$ and P_2 Function.

In particular, the lineal-path function $L(r)$ will be computed from both the original system and the reconstructed realization to study the connectivity of interested phase. In this dissertation, I will use $L(r)$ function as my criteria to assess the reliability and accuracy of reconstructed model in chapter 4.

1.4.5 P_n Functions' Application for Coupling Simulations and Experiments

Not only P_n functions can provide an efficiently way to quantify and reconstruct the microstructure of objects but it also can be used for distinguishing or coupling the difference or relationship between simulations and experiment results. Maybe someone doubts that why the ability to compare or couple the simulations and experiment is so important? Because the precise and verified simulations can shorten the design phases and cost down the budget of investment for products' design and related manufacture, that is why we need a more convincing method to compare simulations and experiments.

Actually, P_n functions can quantify the dissimilarity between simulations and experiments for some metaphysic cases which cannot easily be expressed or compressed thoroughly. Take the following cases for example, if someone asks you that how beautiful is that girl or if these 2 twins look alike? Maybe your answer is "She is pretty" or "They look alike". However, since all the people have their aesthetic standard and their point of view, your answer shouldn't be very objective and understood completely for other people. Actually, the main purpose of P_n functions is aimed to provide a scientific way to quantify the results from abstract phenomenon to countable outcomes by a series of numbers or several curves which can be assessed for the coupling circumstance between simulations and experiment such as complex structure simulation. When a person can validate his simulation's results are reliable and verified, the created programming are pretty useful for further and future use. In my dissertation, I will use vapor-deposition of phase-separation alloy films as example to elaborate P_n functions' ability to quantify 4D structure of films. Of course, P_n functions can be applied and suitable for other fields.

CHAPTER 2

STRUCTURAL QUANTIFICATION FOR HETEROGENEOUS MATERIAL AND ITS MICROSTRUCTURE EVOLUTION

2.1 Introduction of Correlation Functions

In this chapter, I will introduce what is correlation function and some lower-order functions which are non-standard correlation functions but useful for quantification of microstructure. Finally, I will introduce the n-Point Polytope Functions (i.e. P_n functions) which is a subset of standard correction functions can offer more detailed and reliable quantification result.

2.1.1 Conventional Statistical Microstructural Descriptors-Definition of the Correlation Functions

The most prevailed class and widely used descriptor-based representations is the standard n-point correlation (or probability) function Sn, which provides the probability of occurrence of specifically arbitrary n-point configurations in the material imaging [1][24]-[26]. The set of Sn with n from 1 to ∞ provides a complete and thoroughly quantitative microstructure representation, physical properties and performance of the material system under quantitative consideration.

Consider a heterogeneous material occupying two disjointedly random phases (i.e. phase 1, a regions V_1 of volume fraction Φ_1 , and phase 2, regions V_2 of volume fraction Φ_2 shown in Figure 1. 1). The state of each phase in the material is constant and independent of time, that is, $V_1 \cup V_2 = V$ and $V_1 \cap V_2 = 0$. As we denote that phase 1 is our phase of interest, the indicator function $I^{(1)}(x)$ (i.e. the probability of indicator of interested point) of phase 1 is then given by

$$I^{(1)}(x) = \begin{cases} 1, x \in V_1 \\ 0, x \in V_2 \end{cases} \tag{2.1}$$

This formula means that when one throw an arbitrary point into probability map for interested phase 1, the value of indicator function is 1 if the thrown point is located at phase 1, but otherwise the value of indicator function is 0.

We can follow the same procedure to get $I^{(2)}(x)$ and it is clearly to see that

$$I^{(2)}(x) = \begin{cases} 0, x \in V_1 \\ 1, x \in V_2 \end{cases} \tag{2.2}$$

Since phase 1 and phase 2 are independent, continuous and complementary, we can derive that the sum of both indicator function is 1.

$$I^{(1)}(x) + I^{(2)}(x) = 1 \tag{2.3}$$

The n-point correlation function (or n-point probability function) $S_n^{(1)}$ for phase 1 is then defined as follows:

$$S_n^{(1)}(\boldsymbol{x_1}, \boldsymbol{x_2}, \dots, \boldsymbol{x_n}) = \left\langle I^{(1)}(\boldsymbol{x_1}) I^{(1)}(\boldsymbol{x_2}) \dots I^{(1)}(\boldsymbol{x_n}) \right\rangle \tag{2.4}$$

Where the angular brackets "$\langle \dots \rangle$" denote ensemble averaging over independent realizations of the medium. The formula 2.4 is the basic expression for n-point correlation function.

It has been shown that the effective properties of a heterogeneous material can be explicitly expressed as series expansions involving certain integrals of S_n. Interested readers are referred to [2] for detailed discussions of S_n and their properties.

However, using the S_n functions has some drawbacks Taking convex polygon for example, the n point polygon has n sides when n≥3 and each length of side doesn't need to be the same. One needs to permute and enumerate all the difference distance between every n-point configuration to get a thoroughly consideration. In other words, it will be expensive

for computer to compute and store their probability of occurrence even when n=3 shown as Figure 2. 1. The resulting statistical data sets of S_n are typically too tedious and unrealistic to be executed and performed.

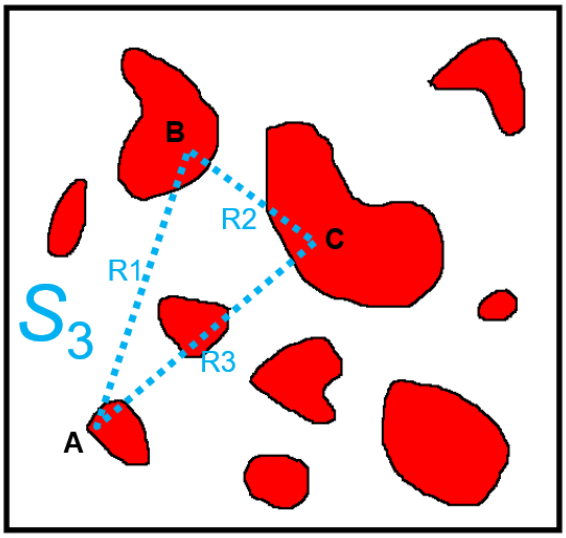

Figure 2. 1 Schematic Illustration of the S_3 (R1, R2 and R3 Are Distance From A to B, B to C and C to A Point Respectively. They Don't Need to Be Given the Same Value.)

For the simplification purpose, more and more researchers adopt the lower order function to quantify the sophisticated structure and the quantification results have been shown that even the lower order function , i.e. S_2 ,can be utilized to model a wide spectrum of different heterogeneous material systems to acquire the data of QMR [27]-[34].

However, some researchers also believe that two-point statistics alone might not be sufficient to represent certain complex microstructures because two-point statistics sometime is too weak to describe all the morphologic features [35]-[38]. Therefore, an alternative approach is to employ the non-standard lower-order correlation functions such as the cluster functions [1][40], which is very effective in capturing specific morphological features (e.g., clustering) [39] or surface functions [41][42], which is encoded with partial higher-order n-point statistics. These methods are powerful but cannot be allowed to systematically

incorporate with hierarchical higher order structural information for microstructure quantification. I will introduce S_2 (two-point correlation functions), Lineal-path function L, Two-point cluster function C_2 and P_n function respectively in the following paragraphs.

2.1.2 Two-Point Correlation Function

Before discussing the two-point correlation function, actually I want to introduce one point probability function first. The one point probability function $S_1^{(1)}$, which is the probability of finding one point to be in the phase 1, is equal to the volume fraction of the phase 1(Φ_1), i.e.,

$$S_1^{(1)}(\boldsymbol{x_1}) = \langle I^{(1)}(\boldsymbol{x_1})\rangle = \Phi_1 \tag{2.5}$$

The value of Φ_1 is also pretty significant for quantification analysis of S_2 function which will be introduce in the next paragraph because it always is the initial outset of the curve of the S_2-r diagram (i.e. the value of S_n functions V.S. the length of the assigned two-point). All the onset of the S_n-r diagram with different value of n should be start at the same initial point when all the distance between every vertex is zero because when the length of every side is zero at the beginning, all the vertices of S_n function are converged and gathered in to one point. In fact, one point probability function is the cornerstone of the S_n function. Besides, P_n functions also have this similar character. I will introduce it more detailed later when we debate about the P_n functions.

The two-point probability function $S_2^{(1)}$ for phase 1 can then be derived from Eq. (2.4) as

$$S_2^{(1)}(\boldsymbol{x_1}, \boldsymbol{x_2}) = \left\langle I^{(1)}(\boldsymbol{x_1}) I^{(1)}(\boldsymbol{x_2})\right\rangle \tag{2.6}$$

S_2 function gives the probability that two randomly selected points x_1 and x_2 fall into phase i and j respectively when the number of phase is 3(see Figure 2. 2(A)). For a material

with q distinct phases, there are totally q*q different S_2. However, it has been shown that only q of them are independent[1][40]-[42] and the remaining q*(q-1) functions can be explicitly expressed in terms of the q independent ones. In our case, q = 2 (i.e., inclusions and matrix) and thus, we only need to consider the two-point correlation functions associated with one of the phases (i.e., either for the inclusion or matrix).

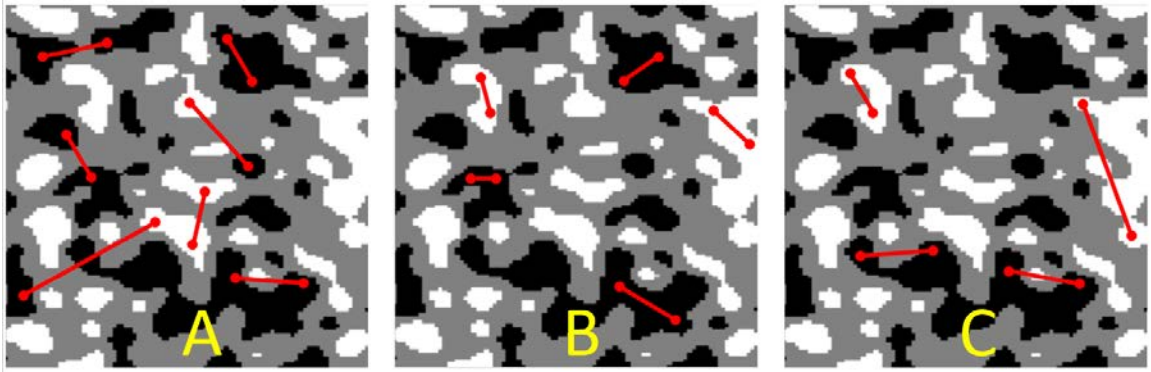

Figure 2. 2 Schematic Illustration of the Events That Contribute to Various Correlation Functions. The Two-Point Correlation Function S_2 Gives the Probably of Finding Two Points in the Phases of Interest. In (A), We Show Events That Contribute to S_2 (ij), Where i, j Can be Either Red Phase or Blue Phase. The Lineal-Path Function L(r) Gives the Probability That a Randomly Chosen Line Segment of Length r Entirely Falls into The Phase of Interest. In (B), We Show Events That Contribute to L(i). The Two-Point Cluster Function C_2 (r) Gives the Probably of Finding Two Points Separated by r In The Same Cluster of The Phase of Interest. In (C), We Show Events That Contribute to C_2 (i).

The system is statistically homogeneous if the joint probability distributions describing the stochastic process are translationally invariant, i.e., invariant under a translation (shift) of the space origin. For a statistically homogeneous medium, $S_2^{(1)}$ is a function of the relative displacements of the point pairs.

$$S_2^{(1)}(\boldsymbol{x_1}, \boldsymbol{x_2}) = S_2^{(1)}(\boldsymbol{x_1} - \boldsymbol{x_2}) = S_2^{(1)}(\boldsymbol{r}) \tag{2.7}$$

Where $\boldsymbol{r} = \boldsymbol{x_2} - \boldsymbol{x_1}$. At r = 0, the auto-correlation function gives the probability that a randomly selected point falls into the phase of interest, i.e., the volume fraction of the associated phase.

The material system is statistically isotropic if the joint probability distributions describing the stochastic process are rotationally invariant, i.e., invariant over rigid-body rotation of the spatial coordinates. If the medium is statistically isotropic, then $S_2^{(1)}$ is only a radial function, depending on the separation distances of point pairs [39].

$$S_2^{(1)}(\boldsymbol{x_1}, \boldsymbol{x_2}) = S_2^{(1)}(|\boldsymbol{r}|) = S_2^{(1)}(r) \tag{2.8}$$

Henceforth, we will drop the superscript in $S_2^{(1)}$ for simplicity. Without further elaboration, S_2 is always the two-point correlation function of the phase of the interest (i.e. phase 1 is interested phase here). With the understanding of the nature of two-point probability functions, one can easily obtain the limit of the value of S_2,

$$\lim_{r\to 0} S_2(r) = \varphi_1 \text{ and } \lim_{r\to \infty} S_2(r) = \varphi_1^2 \tag{2.9}$$

We note that the subset of S_n functions, i.e. S_2, do can give the probability of finding a particular two-points configuration in specific phases to quantify the morphological features..

2.1.3 Lineal-Path Function

The lineal-path function $L^{(i)}(r)$ gives probability that a randomly selected line segment of length r = | r | along the direction of vector r entirely falls into phase i (see Figure 2. 2(B)) [1][44]. When r = 0(i.e. the distance between 2 ends of line segment), $L^{(i)}(0)$ reduces to the probability of finding a point in phase i and thus, $L^{(i)}(0) = \Phi i$. The materials that do not contain obvious cluster features, the probability of finding a line segment with very large length solely falling into any phases is small. Accordingly, for large r values $L^{(i)}$ decays to zero rapidly in such materials. The lineal-path function contains partial topological connectedness

information of the material's phases, i.e., that along a lineal-path. Generally, the lineal-path function underestimates the degree of clustering in the system (e.g., two points belonging to the same cluster but not along a specific lineal path will not contribute to $L^{(i)}$ or the dispersedly irregular shape of cluster will also influence the calculation result.). Although lineal-path function sometime underestimates the clustering features in the system, it still can offer a set of reliable data.

Not only the lineal-path function can be executed in 2D but also performed for distribution of D-dimensional spheres with arbitrary degree of penetrability using statistical-mechanical concepts. The quantification result is very good agreement between theory and the real model [1].

The lineal-path function do can efficiently quantify the connectivity features for common cases. That is why I consider take this non-standard n point correlation function as a criteria to assess the correction and accuracy of reconstruction structure.

2.1.4 Two-Point Cluster Function

The two-point cluster correlation function $C_2{}^{(i)}(X_1, X_2)$ which is slightly different from the two-point correlation function gives the probability that two randomly selected points $\boldsymbol{x}_1$ and $\boldsymbol{x}_2$ fall into the same cluster of phase i (see Figure 2. 2 (C)) [1][45]. The two-point cluster correlation function take consideration about if its end points are located in the same interested phase only rather than if all elements of line segment are located in the same phase or not.

Here, the definition of cluster is that a compact region where any point in this domain is connected to any other point belonged to the same phase by a continuous path completely.

For statistically homogeneous materials, C_2 depends only on the relative vector displacement(r) between the two points, i.e. $C_2(X_1, X_2) = C_2(r)$.

In contrast to the lineal-path function, C_2 contains complete clustering information of the phases, which has been shown to have dramatic effects on the material's physical properties [1]. Moreover, unlike S_2 and L, the cluster functions generally cannot be obtained from lower-dimensional cuts (e.g., 2D slices) of a 3D microstructure, which may not contain correct connectedness information of the actual 3D system because it only takes every calculation within the same cluster in account and neglects calculation of related connectivity.

It has been shown that C_2 is related to S_2 via the following equation [45]

$$S_2{}^{(ii)}(r) = C_2{}^{(i)}(r) + D_2{}^{(i)}(r) \tag{2.10}$$

Where $D_2{}^{(i)}(r)$ measures the probability that two points separated by r fall into different clusters of the phase of interest. In other words, C_2 is the cluster's connectedness contribution to the standard two-point correlation function S_2. For microstructures with well-defined inclusion, C_2 (r) of the inclusions which is a short-ranged function will rapidly decays to zero as r approaches the largest linear size of the inclusions. We note that although C_2 is a "two-point" quantity, it has been shown to embody higher-order structural information which makes it a highly sensitive statistical descriptor over and above S_2 [39][46[47].

2.2 The Introduction of N-Point Polytope Functions (P_n Functions)

In this section, I will introduce the n-point polytope functions. The main reason I want to use P_n functions to quantify my targeted microstructure is that although the lower-order functions such as S_2 and L can efficiently quantify the microstructure, sometimes the complicated microstructure will be underestimated by these lower-order function especially

when the geometric shape of the inclusion or interested phase is pretty variable. It will be difficult for tow-points basis function to thoroughly segment the whole geometric relationship of the structure. However, adopting standard correlation functions to quantify the microstructure is too expensive to obtain the final result. Without loss of generality, I use the n –point polytope functions which only take account of regular polygon with different length of side (i.e. r) as templates to analyze the microstructure.

The whole quantification process is that I acquire a heterogeneous microstructure (either in 3D or a 2D slice. In this dissertation, I adopt 2D analysis) in which the different structural features are segmented and grouped into different "phases". A simple example is a composite microstructure contains a "matrix phase" and a "particle phase", see Figure 2. 3 (a). Note this microstructure can be a snapshot from an evolution process which belongs to 4 D case. The definition of P_n is then given as follows:

P_n (r) $\equiv$ Probability that all of the n vertices of a randomly selected regular n-point polytope with edge length r fall into the phase of interest.

Base on this definition, one can derive two sets of the P_n functions for 2D and 3D. The first set involves n-point regular polygons, for which the vertex (edge) number n can take any positive integer values; and in the limit $n\rightarrow\infty$, the shape becomes a circle (in this limiting case, the quantity r is the radius of the circle, instead of the edge length to prevent P_n functions cannot be converged because of the length of side.). We note that the n-point polygon functions can be computed from both 2D slices and full 3D microstructure. The other set involves 3D polyhedra whose edges are of the same length. Since we merely consider the regular template for P_n functions, only a small number of 3D polyhedra satisfy this condition, including the five Platonic solids (i.e., the regular polyhedra: tetrahedron, octahedron,

dodecahedron, icosahedron, and cube) and the thirteen Archimedean solids (i.e., the semi-regular polyhedra) (see Figure 2. 3 (b)) [48]. In the case of n = 2, the 2-point polytope function P_2 is identical to the standard 2-point correlation function S_2 when number of phase of imaging is 2 in 2D.

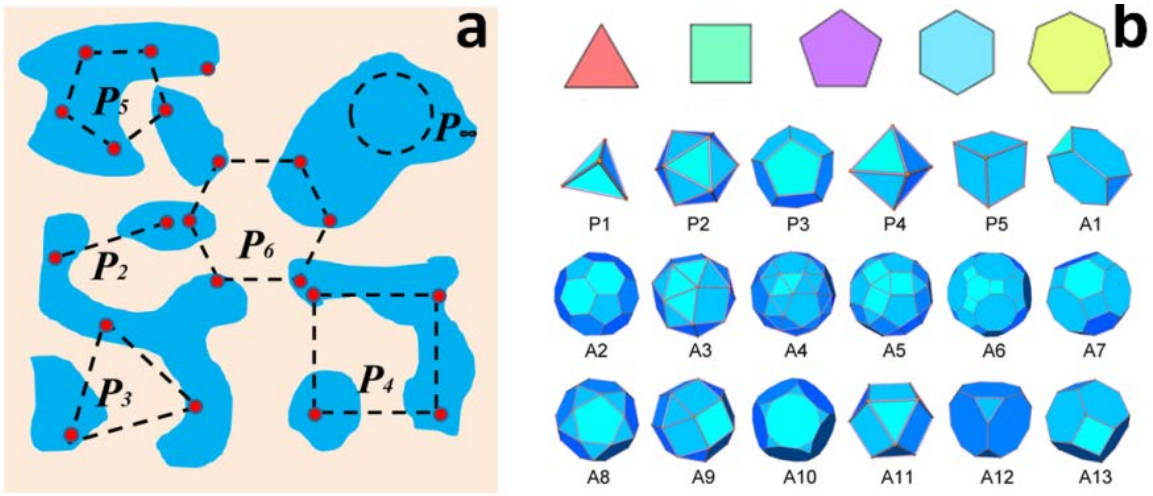

Figure 2. 3 (a) Schematic Illustration of Stochastic Events Contributing to the P_n Functions in the Case of Regular Polygons. (b) Examples of Regular Polygons (Triangle, Square, Pentagon, Hexagon, and Decagon) and Polyhedra (Including the Platonic Solids P1-P5, and Archimedean Solids A1-A13) For Computing the P_n Functions.

Figure 2. 3 (a) schematically illustrates the stochastic events that contribute to the P_n functions in the case of regular polygons. For r = 0, the polygon reduces to a single point, and P_n (r=0) gives the volume fraction Φ of the phase of interest (i.e., the probability a randomly selected point falling into the phase of interest). For finite r values, P_n (r) provides n-point spatial correlations in the phase (feature) of interest. For very large r values (e.g., $r\rightarrow\infty$), the probabilities of finding the vertices in the phase of interest are almost independent of one another, thus, we have P_n ($r\rightarrow\infty$) $\approx \Phi^n$, where Φ is the volume fraction of the phase of interest in the system. These asymptotic behaviors allow us to introduce a convenient re-scaled form of the P_n functions, i.e.,

$$f_n(r) = [P_n(r) - \Phi^n]/[\Phi - \Phi^n] \quad (2.11)$$

With $f_n(r = 0)$=1 and$f_n(r \to \infty)$=1. Finally, we note that one can define "cross-correlation" polytope functions by requiring a subset of the vertices falling into different phases (features) in the microstructure. In this dissertation, we will mainly focus on the "auto" polytope functions defined with 2D polygons, in which all of the vertices of the polygons fall into the same phase of interest.

Moreover, the value of volume fraction (Φ) is also pretty significant for quantification analysis of P_n function because it always is the initial outset of the curve of the P_n -r diagram (i.e. the value of P_n functions V.S. the length of side of assigned template shown as Figure 2. 4). All the onset of the P_n -r diagram with different value of n should be start at the same initial point because when the length of side of all assigned templates are zero at the beginning, all the vertices of all regular templates of P_n function are converged and gathered in to one point. By knowing the initial point and tendency of curve, we can easily predict and determine the calculation results are correct/correct or not.

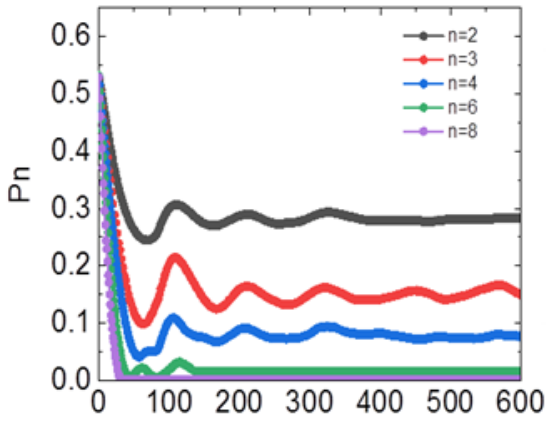

Figure 2. 4 The Tendency of the P_n Functions.

CHAPTER 3

P_n FUNCTIONS' PROCEDURE AND ITS APPLICATION

In this chapter, I will introduce how to compute the P_n function from the imaging data. First, we use X-ray tomography to obtain the 2D interested cross section from the 3D microstructure [55]. The reason we choose X-ray tomography is that it is an extremely efficient, low-cost, and non-destructive technique for characterizing microstructure in 3D and 4D [49][50][51]. One can obtain imaging of multi-component materials from the sub-micrometer to nanometer range by using high brilliance and partially coherent synchrotron light. X-ray tomography can be conducted in imaging modes based on absorption or phase contrast. The technique can also be used using lab-scale systems (See Figure 3. 1). In x-ray tomography, 2D projections usually obtained at small angular increments can be employed to generate grayscale images of the microstructure. For simplifying purpose, square imagine of which length is denoted as Maxx will be used for its transformed probability map within my whole dissertation. When I acquire the 2D imaging, my first step is to transfer the imagines into grayscale and control their threshold value (from 0-255) or images' contrast value to segment/distinguish details of individual material phases of interest and produce probability maps which are accurately 2D digitalized representations of the 3D microstructure. In my programing part, I set black pixel as my interested phase (i.e. inclusion of interest.) and white one as matrix. Such data sets of probability map can be used to quantify the microstructure. After I extract the P_n functions hundred times from the probability map, I really feel that x-ray tomography is an excellent technique/method that eliminates destructive cross-sectioning, and allows for superior resolution and image quality with minimal sample preparation[4]-[8][56][57].

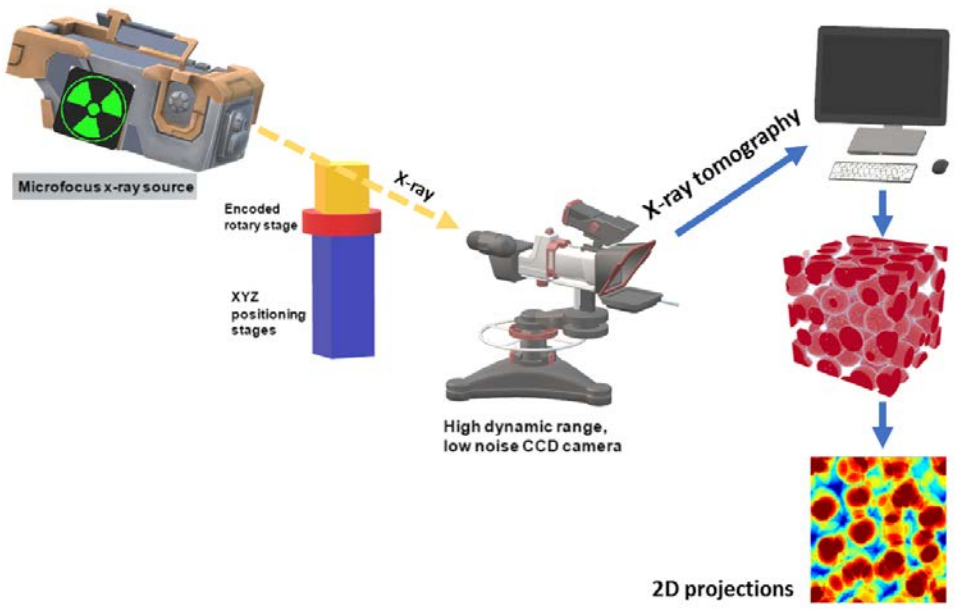

Figure 3. 1 Schematic Illustration of the Key Components of X-Ray Tomography and an Illustration of a 2D Projection of a 3D Hard Sphere Packing Structure. Different Colors in the 2D Projection Represent Different Attenuated Intensities.

3.1 Computing P_n Functions from Imaging Data

Once we obtain the imaging data of probability map including both 2D images or 3D digital representations of the material microstructure, the probability-based descriptor of the P_n functions allow us to easily compute and extract the features from microstructural data. For example, in order to compute the value of $P_n(r)$ with r=r*, the following procedure is used [55]:

(i) We first decide that how many type of the regular n-polytopes, i.e. the value of n, are needed to be generated with the edge/side length r. Since I merely analyze 2D probability map in this dissertation, only the regular polygon templates are used. For example, if n=4, it means that we will create one-point, 2-point, triangle, and square templates to calculate the P_n functions. The value of r is the integer less equal than the half value of the pixel number/length of probability map because

of the setting of continuous boundary condition which will be detailed described in the following section.

(ii) In order to obtain a rigorous and real probability map, I adopt the periodic boundary conditions, i.e. PBC, for every imaging to execute the P_n functions. Actually, PBC is wildly used in computer simulation and mathematical models to let a limit unit model to be calculated as an infinite model. For 2D, the minimum PBC is combined with additional 8 congruent imaging, shown as

(iii) Figure 3. 2, to construct a macroscopic imaging rather than a microscopic one. When a particle passes one side of a unit, this particle will proceed to enter the according side of its ambient unit with the same direction and speed. This characteristics can ensure the conservation of moment/energy of the whole system to get more accurate and reasonable results. Besides, when we calculate the distance between point A and point B without the PBC setting, the distance should be r_2 with microscopic point of view. However, when we add the PBC setting, the shortest distance between becomes r_1 because both B point are same entity under PBC setting. Besides, when using P_n functions, we focus on the nearest distance as the side of polygon to avoid overestimation. So the value of r, the distance between 2 points, is always $\leq L/2$. Here, L stands for the length/pixel of the square image. For this reason, I set n_t, the length of side of any template, is $\leq L/2$ in the programing and add the PBS setting to my probability map to obtain more reasonable and precise results.

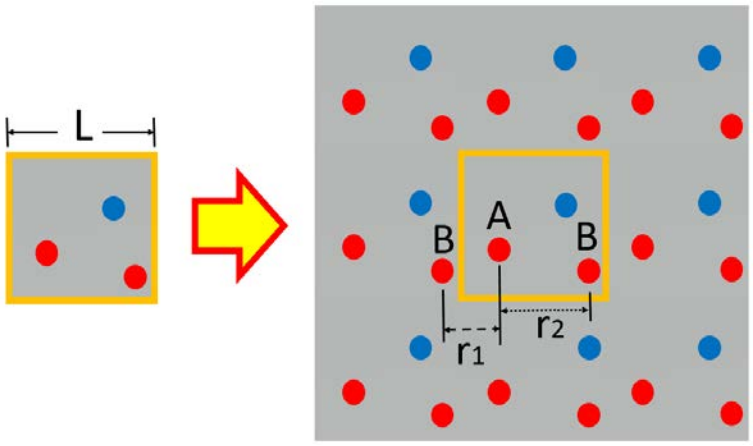

Figure 3. 2 Schematic Illustration of Periodic Boundary Condition.

(iv) When step i and ii are ready, then the selected polygon are randomly allocated and constantly oriented with periodic boundary condition for M times in the probability map which is transform from material microstructure (see Figure 3. 3(a)).

(v) Every time when the selected polygon is placed in the probability map, we check whether all of its vertices fall into the phase of interest (i.e., a "success" event), and we count the total number of success event Ms out of a total of M trials. Because the thrown templates are assigned into an infinite probability map which is set with the PBC, the distance between templates' 2 adjacent vertices located in the interested pixel (or voxel in 3D) denoted as r in dissertation is driven as the nearest one. Therefore, the edge length of the pixel/voxel defines the smallest distance in the system and provides a natural unit for measuring the distance.

(vi) We compute P_n (r*) = Ms/M. The P_n (r*) is the probability that a randomly selected n-polygon with the length of side, i.e. r*, having all its vertices fall into the phase of interest

(vii) Repeat step v for different r* values(r* is an integer and $1 \leq r^* \leq r$) to compute the full $P_n(r)$ function.

(viii) Finally, the $P_n(r)$ vs r diagram is drawn for further analysis purpose. Actually, many potential and hidden features/characters of imaging can be driven from this result diagram. How to uncover the relatedly concealed information will be discussed in the next section. .

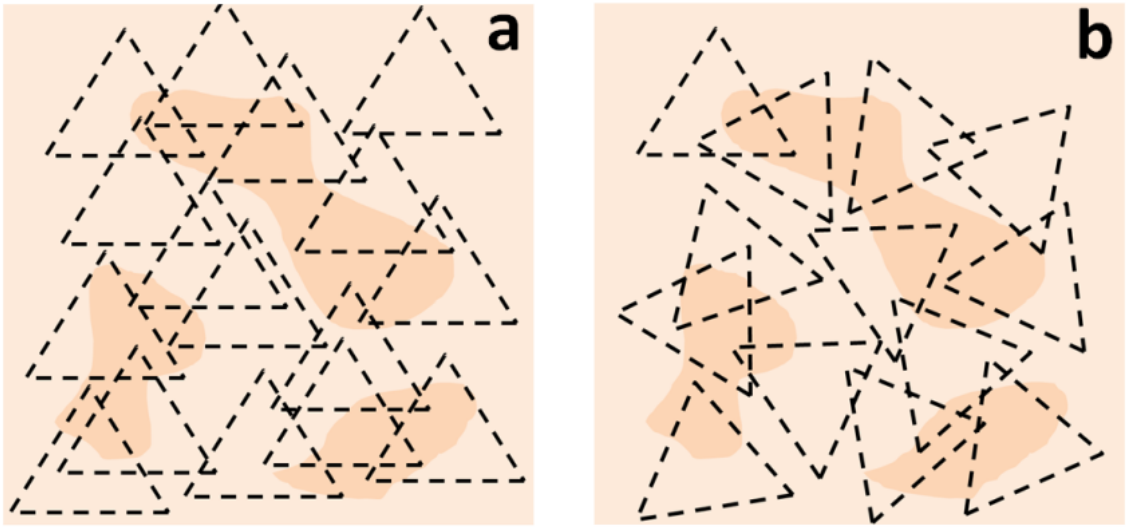

Figure 3. 3 Schematic Illustration of Different Sampling Templates for Computing P_n Functions (in the Case of n=3) From Images: (a) Directional Sampling, in Which Only the Location of the Template Is Randomly Selected. (b) Isotropic Sampling, in Which Both the Location and Orientation of the Polygon Template Are Randomly Selected.

For sure, one can place n-polygon templates orientations (i.e., isotropic sampling shown as Figure 3. 3(b)) rather than constant orientation, directional sampling, to gather more information for more intricate cases. However, it means that you need to spend more time and computer resource to obtain more detailed result.

3.2 Information Content of P_n Functions Based on Model Microstructures

3.2.1 P_n Functions for Separated Sphere Model

In this section, I will continuously introduce the information content of P_n Functions. For simplifying purpose, I will take Figure 3. 4 for example to thoroughly demonstrate the implication and meaning of curve of P_n vs r diagram. The upper panels of Figure 3. 4 shows diverse morphologies of congruent spheres and lower panels are their related P_n –r diagram (i.e. P_2 –r curve for this example)[55]. Here, r which is less and equal the half value of the imaging length stands for the nearest distance between 2 arbitrarily thrown points. Different morphology has different curve tendency which can potentially offer additional information to us. By observing the left 2 imaging of Figure 3. 4, it goes without saying that the value of r occurred with the zero slope at the first decay meant the size of interested phase (i.e. red phase) because when r increases its length over the diameter of the sphere, there is no any possibility for 2 arbitrary points to be located in the interested phase. Moreover, the value of r happened with the zero slope at the second decay means the distance from its neighbor. Besides, the converged value of the elevation of the P_n –r curve is also an important index for imaging. The converged value of the elevation indicates the dispersion and distribution of the same polytope templates. We can obviously acknowledge that the value of converge elevation shown as Ea at lower right panel is higher than lower middle and lower left one because the P_2 polytope templates which are fallen in the interested phase are closer than r averagely. It means the allocation and arrangement of every polytope template has a high connectivity.

Since not only P_2–r curve can show these properties but also other P_n–r curve can sift their related information, I will introduce one more complex case and real case to illustrate the significance and explicitness of the P_n function in the following sections.

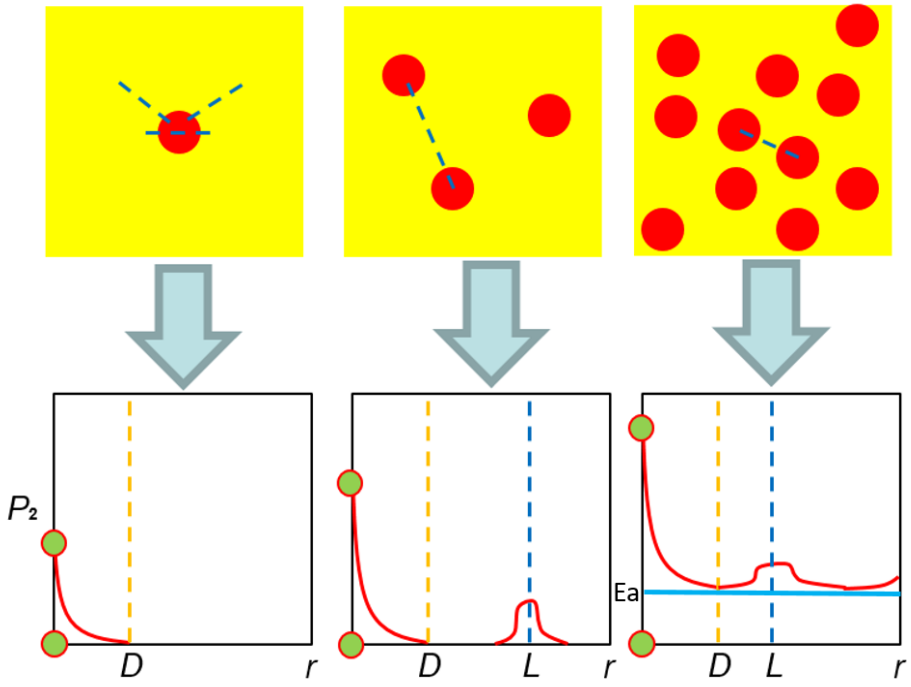

Figure 3. 4 Schematic Illustration of P_2-r Curves.

3.2.2 P_n Functions for Triangle Particles with Different Orientation and Arrangement.

In this section, I will illustrate the result of 2 models composed of congruent equilateral triangle particles arranged on a square lattice and triangular lattice with different orientations in Figure 3. 5(a) and Figure 3. 6(a) to more comprehensively specify the information contained in the P_n vs r diagram. The orientations of all triangle particles in each model are the same but the orientation in each model are different.

First, let's embark on the introduction of the P_n functions of Figure 3. 5(a). In order to demonstrate and consider more factors to get more detailed result, I create 2 directional sampling templates along with x and y axis direction for P_3 (i.e. 3-point polytope functions). In other worlds, the directional P_3 functions are computed by fixing the orientation of the equilateral triangular sampling templates vertically and horizontally respectively. From Figure

3. 5 (b) and Figure 3. 5 (c), the results can be seen that the P_3 functions for all four microstructures start with the same value at r = 0, which is the volume fraction of the particles; and monotonically decrease as one moves away from r = 0. This monotonically decaying behavior is introduced in 2.2 and happened for all P_n functions. The reason of it is that when r is small from zero, the majority of contributions to the correlation functions are from the events in which the sampling templates entirely fall into the interested phase. That is why the success of such events dramatically decreases as the size of the template increases. When the value of r is bigger than the average length of diameter of the interested particle, the value of P_n function will converge to a constant value. If the average space between the adjacent interested particles are large than the average diameter/length of interested phase, the value of P_n function will approach to zero. Otherwise, the value of P_n function will converge to certain value according to the configuration of the microstructure.

We note that when the orientation of the triangular particles is consistent with the orientation of the sampling triangular template, the resulting P_3 function exhibits a slower decay for small r. This is because in such cases, the sampling templates with larger sizes (i.e., associated with larger r values) can still entirely fall into a single particle. So slower decreasing tendency of curve means that the shape of sampling template and interested particle/phase have more geometry relationship between each other. Under this observed circumstance, for sure, when one adopt various orientation of sampling template to perform P_n functions, one can easily observe and predict which shape with certain directional orientation is more proper to compute but it will cost lots of time and computer resource.

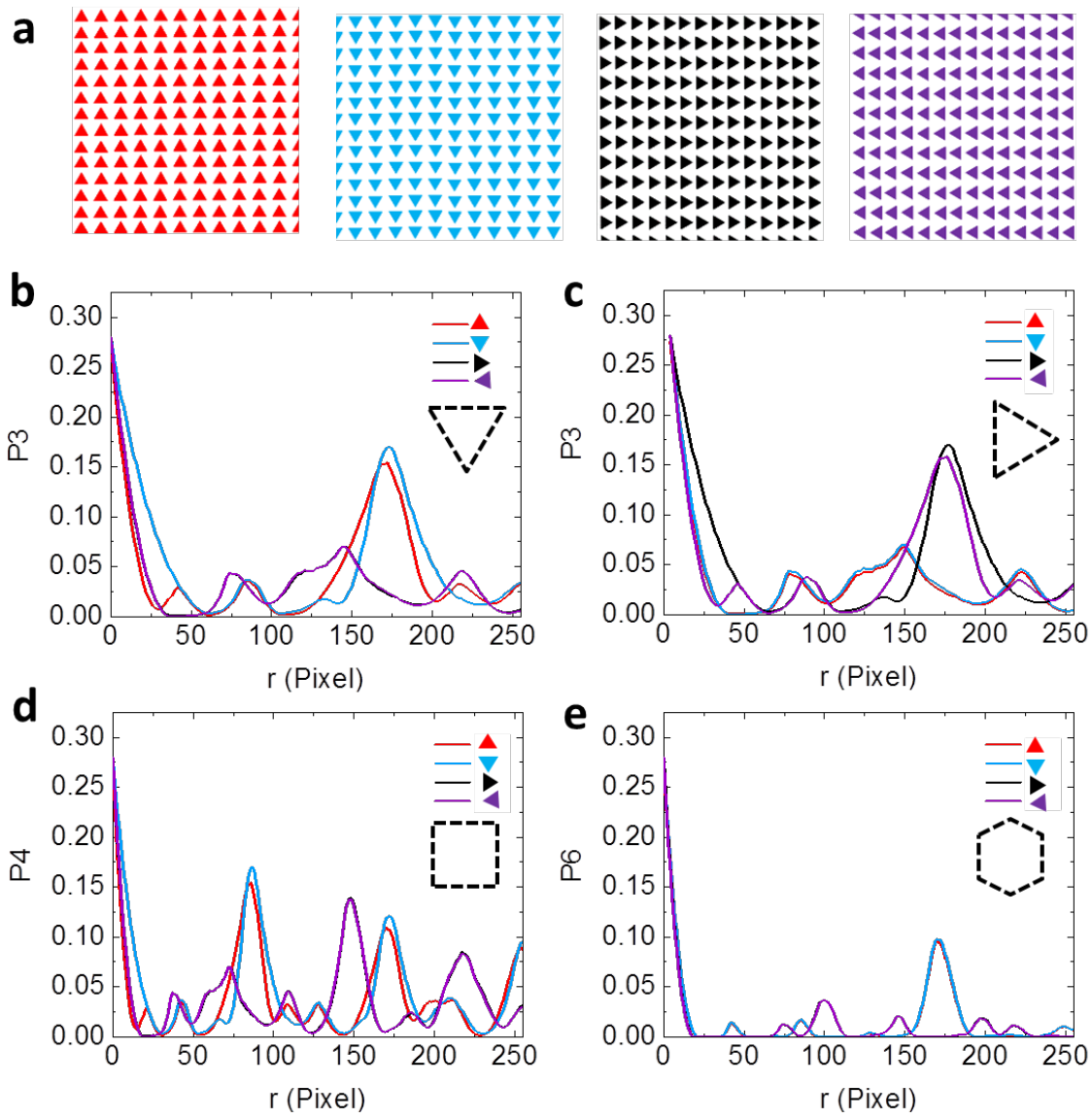

Figure 3. 5 (a) Model Microstructures Composed of Congruent Equilateral Triangle Particles With Different Orientations Arranged on a Square Lattice. The Resolution of the Images Is 1048 by 1048 Pixels. (b) Directional 3-Point Polytope Functions P_3 for the Model Microstructures Associated With Vertically Oriented Triangular Sampling Templates. (c) Directional 3-Point Polytope Functions P_3 for the Model Microstructures Associated With Horizontally Oriented Triangular Sampling Templates. (d) 4-Point Polytope Functions P_4 for the Model Microstructures. (e) 6-Point Polytope Functions P_6 for the Model Microstructures. The Unit of Distance Is One Pixel Length.

Interestingly, Figure 3. 5 (b) and Figure 3. 5 (c) can be seen that beyond the initial decay, the P_3 functions exhibit significant peaks at certain intermediate and event large r values

(e.g., $r \approx 180$, 290, 340, 430 pixels). These peaks indicate the existence strong triangular correlations (i.e., hidden triangular patterns/symmetry) on the length scales as defined by the associated r values. We note it is very surprising to detect the emergence of large-scale triangular correlation (symmetry) in packing arrangements based on square lattice. This example also indicates that the novel statistical descriptors we developed are very efficient in capturing hidden order and spatial correlations in the microstructure [55].

Figure 3. 5(d) shows the 4-point polytope functions P_4 for the model microstructures. A series of peaks (i.e., oscillations) beyond the initial decay can be clearly observed. These peaks correspond to the square correlation/symmetry on different length scales in the packings, which are resulted from the square symmetry of the underlying packing lattice. The P_4 functions are almost identical for all four microstructures (see Figure 3. 5(a)), indicating that for this function the packing arrangements of the particles is more sensitive to the local particle shape [55].

Figure 3. 5 (e) shows the 6-point polytope functions P_6 for the model microstructures. It can be seen that the initial decay of P_6 is much faster than that in P_3 and P_4. This is because it is more difficult to entirely fit a hexagon in the particle compared to a triangle or a square with the same edge length. The P_6 functions also exhibit significant peaks on certain intermediate and large length scales (e.g., $r \approx 180$, 290, 340, 430 pixels), indicating hidden hexagonal symmetry/correlations on that length scale. These length scales are completely consistent with the length scales associated with the triangular peaks in P_3 because the geometry of hexagon actually can be combined with these 2 oriented sampling templates [55].

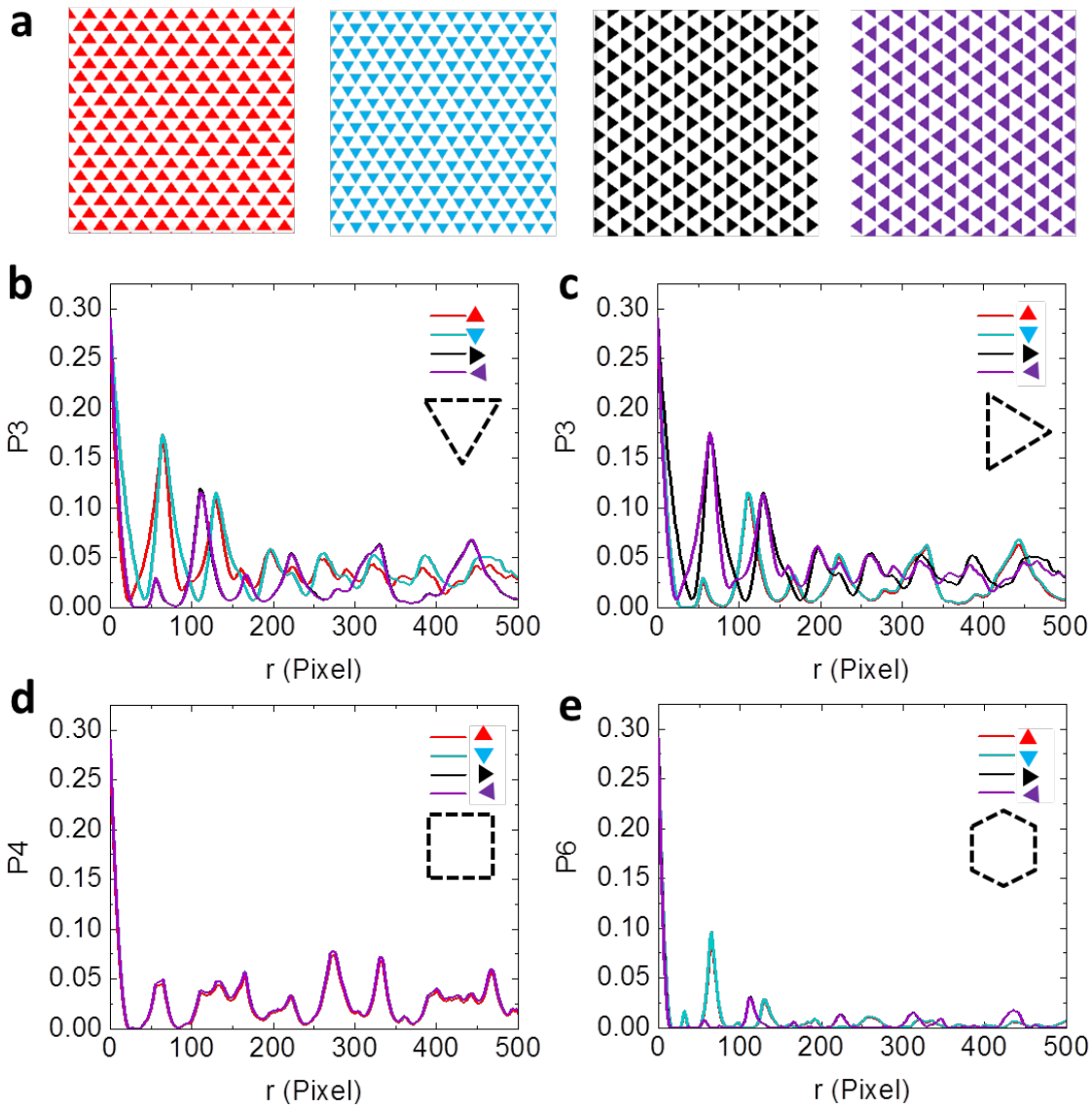

Figure 3. 6 (a) Model Microstructures Composed of Congruent Equilateral Triangle Particles With Different Orientations Arranged on A Triangular Lattice. The Resolution of the Images Is 1048 by 1048 Pixels. (b) Directional 3-Point Polytope Functions P_3 for the Model Microstructures Associated With Vertically Oriented Triangular Sampling Templates. (c) Directional 3-Point Polytope Functions P_3 for the Model Microstructures Associated With Horizontally Oriented Triangular Sampling Templates. (d) 4-Point Polytope Functions P_4 for the Model Microstructures. (e) 6-Point Polytope Functions P_6 for the Model Microstructures. The Unit of Distance Is One Pixel Length.

Now, let's discuss the P_n functions of triangle particles which contain triangular packing lattice with different orientation in Figure 3. 6(a). Figure 3. 6 (b) and Figure 3. 6 (c) show the directional 3-point polytope functions P_3 respectively associated with vertically and

horizontally oriented triangular sampling template for the model microstructures shown in Figure 3. 6 (a). The P_3 functions initially decay and exhibits a series of significant peaks (oscillations) with decaying magnitude as r increases. These peaks are associated with triangular correlations on different length scales, resulted from the underlying triangular packing lattice [55].

Figure 3. 6 (d) shows the 4-point polytope functions P_4 for the model microstructures. The hidden square correlations on large length scales (e.g., $r \approx 275$, 340 pixels) are again picked up and manifested as the associated peaks. Figure 3. 6 (e) shows the 6-point polytope functions P_6 for the model microstructures. Similar to the P_3 functions, the P_6 functions exhibit significant peaks and strong oscillations, indicating the hidden hexagonal correlations resulted from the triangular packing arrangements [55].

We can see from these examples that the P_n functions can provide a systematic "decomposition" of the features of interest in the microstructure in terms of a series of polytope basis and very effective in capturing hidden symmetry/spatial orders in the system. Therefore, the set of P_n functions offers a systematic way to devise more accurate microstructure representations by successively incorporating higher order morphological information [55].

3.3 Quantifying Microstructure of Heterogeneous Materials via P_n Functions

In this section, we employ the P_n functions to quantify and model a variety of heterogeneous materials with distinct microstructures, including particle reinforced composites, bi-phase interpenetrating composites and porous materials. In addition, we also apply the P_n functions to quantify and model the microstructural evolution (e.g., coarsening development) in a lead-tin alloy aged at 175°C up to 120 hours.

In next section, I will illustrate more complicate microstructures to explore P_n functions' outstanding performance and ability to quantify microstructures.

3.3.1 Quantification of Complex Microstructures

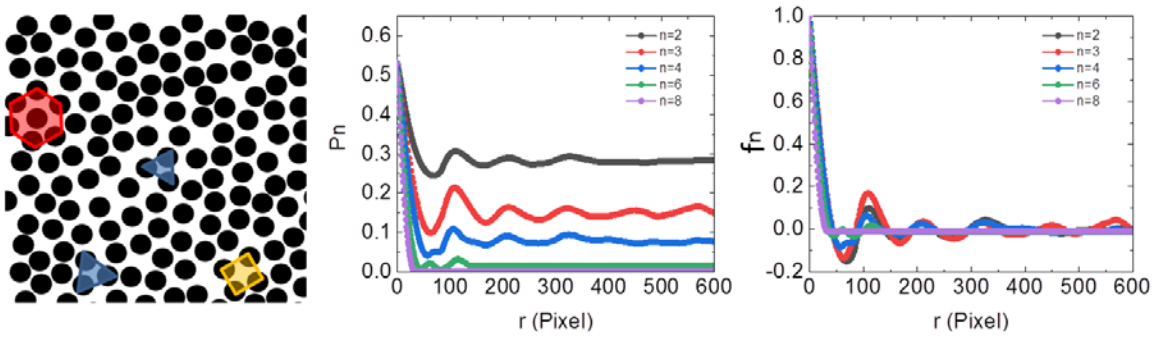

Figure 3. 7 (a) 2D Microstructure Composed of Equal-Sized Hard Spheres in a Matrix. (b) The P_n Functions for the Particle Phase with n =2, 3, 4, 6 and 8. (c) The Corresponding Rescaled f_n Functions Highlighting the Spatial Correlations (c.f. Eq. (2.11)).

Figure 3. 7 shows the quantification of a 2D microstructure composed of equal-sized hard spheres in a matrix [28], i.e., a packing (see Figure 3. 7 (a)). The sphere packing is generated using Monte Carlo simulations [29]. The size of the image is 1024 by 1024 pixels and the diameter of the particle is D = 65 pixels. Figure 3. 7 (b) shows the P_n functions for the particle phase with n =2, 3, 4, 6 and 8. Similar to the cases of the model microstructures discussed in previous section, all P_n functions initially decay from the volume fraction Φ=0.545 as r increases from 0. The positions of the first minimum in the P_n functions for small n values

roughly correspond to the linear size of the particle (~ 65 pixels). After the initial decay, all P_n functions studied here except for n = 8 exhibit strong oscillations and the first peaks in different P_n functions occur at approximately the same r values. These oscillations respectively indicates strong pair, triangle, square and hexagonal correlations on different length scales in the system. Figure 3. 7 (b) illustrates examples of such correlations, which are all associated with the mean nearest neighbor separate distance, i.e., the distance associated with the first peak in P_2. These correlations result from the tendency for the particles to self-organize on a triangular lattice at high densities. The P_8 is almost flat after the initial decay, indicating the system does not possess any octagonal correlations on intermediate and large length scales. Figure 3. 7 (c) shows the corresponding rescaled f_n functions highlighting the spatial correlations (c.f. Eq. (2.11)) [55].

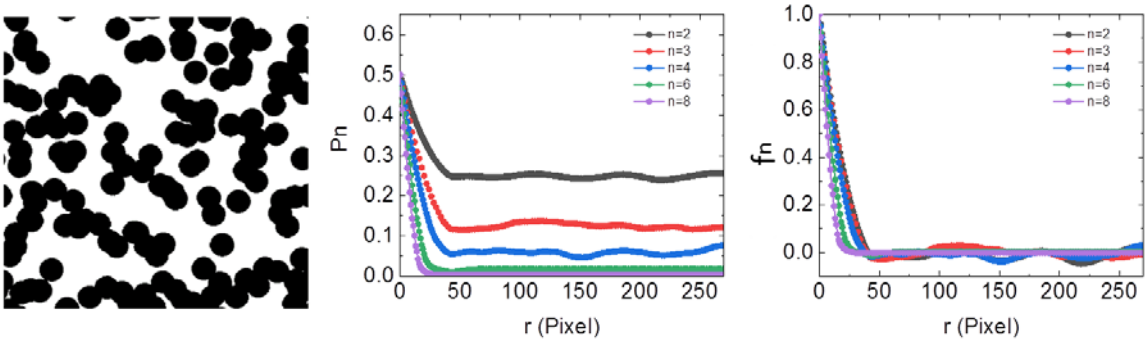

Figure 3. 8 (a) 2D Microstructure Composed of Equal-Sized Overlapping Spheres in a Matrix. (b) The P_n Functions for the Particle Phase With n =2, 3, 4, 6 and 8. (c) The Corresponding Rescaled f_n Functions Highlighting the Spatial Correlations (c.f. Eq. (2.11)).

Figure 3. 8 shows the quantification of a 2D microstructure composed of equal-sized overlapping spheres in a matrix [28] (see Figure 3. 8 (a)). The spheres are randomly placed in the matrix without any built-in spatial correlations. The size of the image is 512 by 512 pixels and the diameter of the particle is D = 45 pixels. Figure 3. 8 (b) shows the P_n functions for the particle phase with n =2, 3, 4, 6 and 8. Similar to the previous systems, all P_n functions initially

decay from the volume fraction Φ=0.50 as r increases from 0. After the initial decay, all P_n functions are virtually flat, indicating that the particles possess no spatial correlations of any symmetry on any length scales beyond the diameter of the particles. We note that for the totally random overlapping sphere system, the P_n functions possess the analytical expression P_n I = exp[-$\varrho v_n(r; R)$], where ϱ is the number density of the spheres in the system (i.e., number of spheres per unit volume) and $v_n(r; R)$ is the volume of the union of n spheres with radius R with centers placed at the vertices of a n-polytope with edge length r. Figure 3. 8 (c) shows the corresponding rescaled f_n functions highlighting the spatial correlations (c.f. Eq. (2.11)) [55].

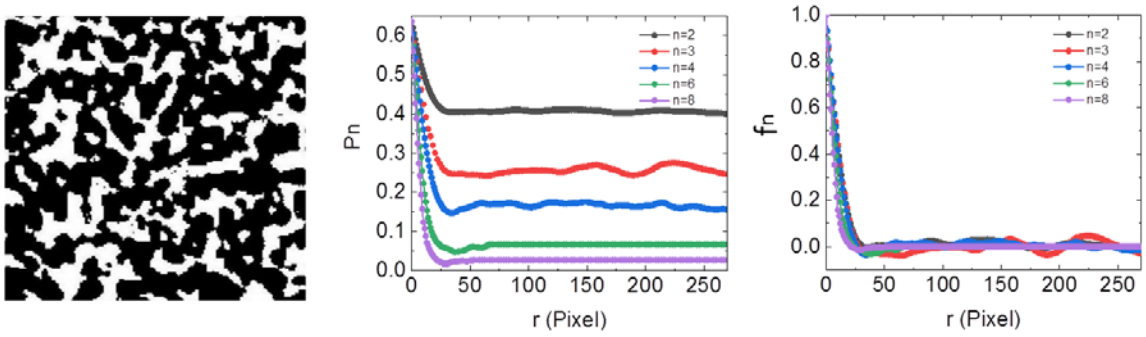

Figure 3. 9 (a) 2D Image of a Concrete Microstructure Composed of Reinforcement Rocks (Shown in Black) and the Cement Paste (Shown in White). (b) The P_n Functions for the Rock (Black) Phase with n =2, 3, 4, 6 and 8. (c) The Corresponding Rescaled f_n Functions Highlighting the Spatial Correlations (c.f. Eq. (2.11)).

Figure 3. 9 shows the quantification of a 2D concrete microstructure composed of reinforcement rocks (shown in black) and the cement paste (shown in white) [74](see Figure 3. 9 (a)). The rock particles possess complex polygonal morphologies and a wide size distribution. The size of the image is 400 by 400 pixels. Figure 3. 9 (b) shows the P_n functions for the rock phase with n =2, 3, 4, 6 and 8. Similar to the previous systems, all P_n functions initially decay from the volume fraction Φ=0.48 as r increases from 0. The r value associated with the first minimum in the functions provides the average particle size in the system, i.e., ~ 40 pixels. After the initial decay, the lower-order P_n functions (e.g., n≤4) exhibit weak

oscillations, reflecting the spatial correlations resulted from the mutual exclusion effects of the rock particles. The correlations are much weaker compared those in hard-sphere systems, mainly due to the anisotropy and size polydispersity of the rock particles. Figure 3. 9 (c) shows the corresponding rescaled f_n functions highlighting the spatial correlations (c.f. Eq. (2.11)) [55].

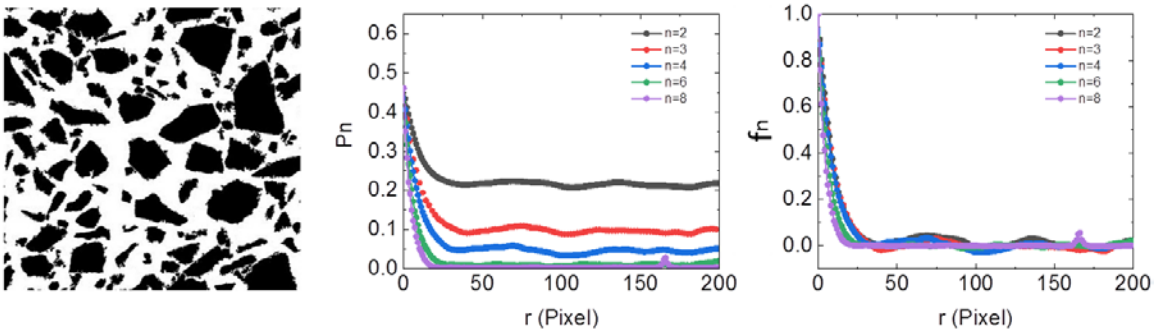

Figure 3. 10 (a) 2D Image of A Fontainebleau Sandstone Microstructure Composed of the Rock Phase (Shown in Black) and the Pore Phase (Shown in White). (b) The P_n Functions for the Rock (Black) Phase with n =2, 3, 4, 6 and 8. (c) The Corresponding Rescaled f_n Functions Highlighting the Spatial Correlations (c.f. Eq. (2.11)).

Figure 3. 10 shows the quantification of a 2D microstructure of a Fontainebleau sandstone composed of the rock phase (shown in black) and the pore phase (shown in white)[30] (see Figure 3. 10 (a)). Similar to the concrete microstructure, the rock particles possess complex shapes and a wide size distribution. In addition, the particles are densely packed and compressed such that their boundaries are fused and cannot be clearly distinguished. The size of the image is 512 by 512 pixels. Figure 3. 10 (b) shows the P_n functions for the rock phase with n =2, 3, 4, 6 and 8. Similar to the previous systems, all P_n functions initially decay from the volume fraction Φ=0.82 as r increases from 0. The r value associated with the first minimum in the functions provides the average particle size in the system, i.e., ~ 32 pixels. After the initial decay, the P_n functions exhibit very weak oscillations for small and intermediate r values. This behavior is similar to that observed for the

overlapping sphere system, as the rocks are compressed and fused which can be effectively considered as "overlapped" in the boundary regions. Figure 3. 10 (c) shows the corresponding rescaled f_n functions highlighting the spatial correlations (c.f. Eq. (2.11)) [55].

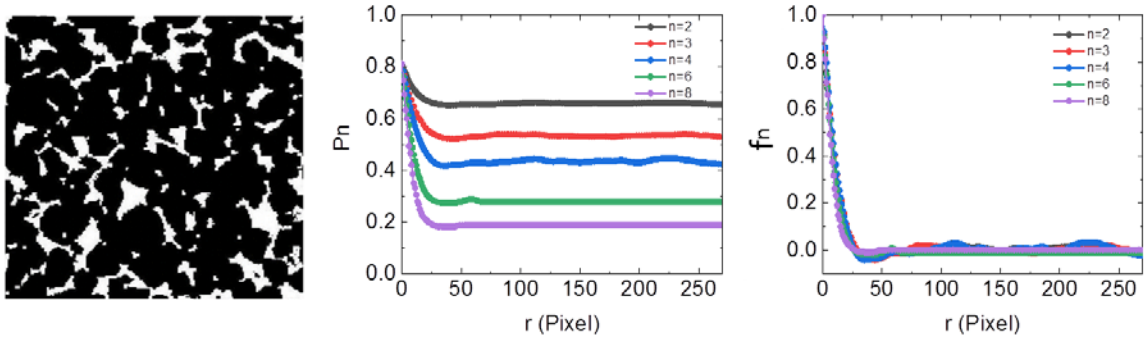

Figure 3. 11 (a) 2D Image of an Interpenetrating Metal-Ceramic Composite Microstructure Composed of the Boron-Carbide Phase (Shown in Black) and the Aluminum Phase (Shown in White). (b) The P_n Functions for the Boron-Carbide (Black) Phase with n =2, 3, 4, 6 and 8. (c) The Corresponding Rescaled f_n Functions Highlighting the Spatial Correlations (c.f. Eq. (2.11)).

Figure 3. 11 shows the quantification of a 2D an interpenetrating metal-ceramic composite composed of the boron-carbide phase (shown in black) and the aluminum phase (shown in white) [30] (see Figure 3. 11 (a)). This microstructure contains "ligaments" of similar width instead of "particles". The size of the image is 512 by 512 pixels. Figure 3. 11 (b) shows the P_n functions for the rock phase with n =2, 3, 4, 6 and 8. Similar to the previous systems, all P_n functions initially decay from the volume fraction Φ=0.65 as r increases from 0. The r value associated with the first minimum in the functions provides the average ligament width in the system, i.e., ~ 27 pixels. After the initial decay, the P_n functions exhibit weak oscillations for small and intermediate r values, characterizing the exclusion effects between the ligaments. Figure 3. 11 (c) shows the corresponding rescaled f_n functions highlighting the spatial correlations (c.f. Eq. (2.11)) [55].

3.3.2 Quantification of Microstructure Evolution

P_n functions not only can comprehensively describe the features of microstructure but also can efficiently quantify the evolution of it. We now employ the P_n functions to quantify microstructure evolution (e.g., coarsening development) in a lead-tin alloy aged at 175°C up to 120 hours, see Figure 3. 12. [75], we model the evolution process using time-dependent 2-point correlation function S_2, which is equivalent to P_2. We showed that when properly scaling with the time-dependent increasing length scale (e.g., the average width of the ligaments), the S_2 functions correspond to different aging time all collapse approximately onto a universal curve, capturing the intrinsic density fluctuations in the system. Here, we investigate the higher order functions.

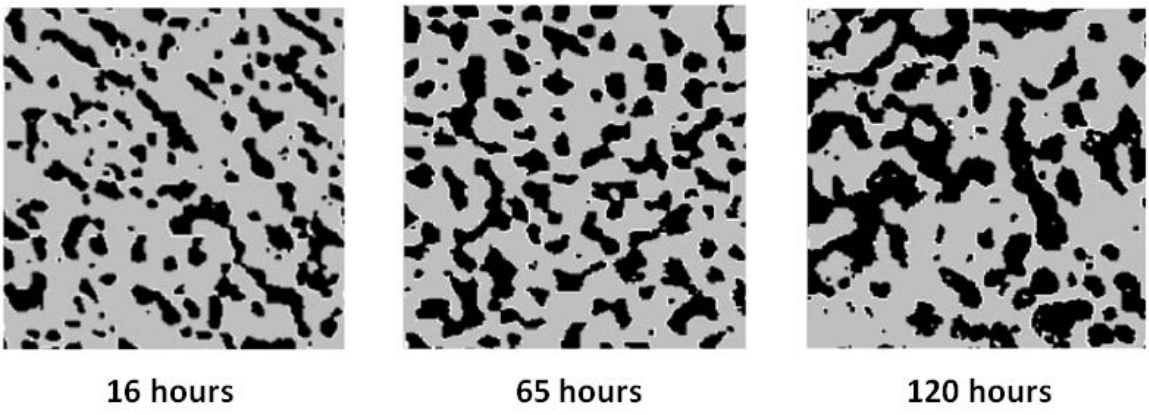

Figure 3. 12 Representative Microstructures of the Lead-Tin Alloy (Pb37Sn63) at 175 °C for Different Times. The Dark Region Represents Lead-Rich Phase and White Region Represents Tin-Rich Phase. The Linear Size of the Microstructure Is 100 μm. The Resolution of the Image Is 600 by 600 Pixels.

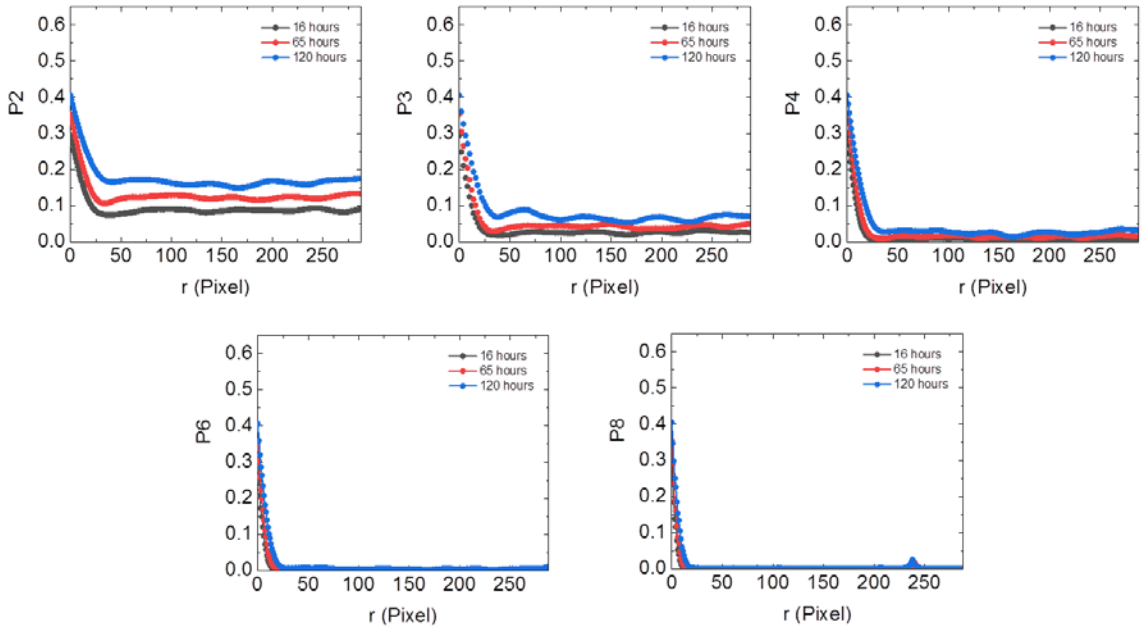

Figure 3. 13 The P_n Functions Associated With the Pb-Sn Alloy Microstructures at Different Aging Times.

Figure 3. 13 shows the P_n functions (with n = 2, 3, 4, 6 and 8) associated with the Pb-Sn alloy microstructures at different aging times as shown in Figure 3. 12. It can be seen that for P_n functions, the initial decay as r increases from 0 becomes slower as aging time increases. In other words, the r value associated with the first minimum in the functions increases as aging time increases (i.e. $r_{16\text{-hr}}$ value> $r_{25\text{-hr}}$ value > $r_{160\text{-hr}}$ value). As discussed above, this r value characterizes the average width of the "ligaments" in the microstructure, which coarsens as aging time increases. By the way, since the particles coarsen during the annealing process, the connectivity between each particle increases. By watching P_2 vs r diagram in Figure 3. 13, we can notice that the converged height increases as aging time increases (i.e. $Ea_{160\text{-hr}}$ value> $Ea_{25\text{-hr}}$ value > $Ea_{16\text{-hr}}$ value). However, this phenomena correspond our previous conclusion which is denoted in 3.2.1 can explain its real physical situation [55].

Moreover, at large aging time (e.g., t = 120 hours), we can see that significant triangle and square correlations emerge in the microstructure, which are manifested as the relatively

strong oscillations in the corresponding P_3 and P_4 functions. Such higher order correlations are not observed for small aging time and might be resulted from the additional correlation induced due to coarsening development. We note that the P_2 functions also exhibit stronger oscillations as coarsening proceeds. It is now clear that the observed pair correlations are associated with the emergence of higher order correlations due to coarsening. This example illustrates the importance of incorporating higher-order statistics for accurate quantification and representation of complex microstructural evolution [55].

In this chapter, we have introduced a set of hierarchical statistical descriptors, i.e., the n-point polytope functions P_n for quantitative representation of complex heterogeneous materials and microstructure evolution. The P_n functions provide the probability of finding regular n-polytopes in 2D with vary sizes in the material phase of interest, which are a subset of the full n-point correlation function S_n. We have shown that the P_n functions allow one to systematically incorporate higher order spatial correlations for microstructure quantification in a concise, expressive, and interpretable fashion, and provide an effective decomposition of the features of interest into polytope correlations.

Besides, according to our computational result, we can conclude that if the a particular correlation function P_n does not possess significant oscillations beyond the initial decay as the distance increases, the system typically does not possess strong n-polytope correlations. Therefore, that particular P_n function might not be necessary for quantifying the system. For most of material systems studied in the paper (such as the metal-ceramic composite, concrete, sandstone and PbeSn alloy), we can see that the octagonal function P_8 does not possess significant oscillations, which indicates that for these systems, it might not be necessary to go up to n=8. However, for the model composite microstructure (i.e., a packing of equal-sized spheres in a matrix), P_8 clearly shows oscillations for small and intermediate distances,

indicating P_8 is required in order to accurately capture octagonal correlations on these length scales. It manifests that if we can further consider higher order P_n functions into account to quantify the microstructure, we can get more overall results of quantification.

The utility of the P_n functions has been demonstrated by applying them to quantify and model a variety of complex heterogeneous material systems as well as microstructural evolution. Our results suggest that the n-point polytope functions can offer a practical set of basis for quantitative microstructure representation (QMR), for both static 3D complex microstructure and 4D microstructural evolution of a wide spectrum of heterogeneous material systems.

3.4 Conclusions and Discussion of P_n Functions

In our opinion, an ideal set of material representations and quantification shall acquire the following crucial properties: (1) conciseness to facilitate tractable sampling and inverse design within the low-dimensional representation space; (2) expressiveness to enable high-fidelity reconstruction of complex microstructures with heterogeneous morphologies, and accurate predictions of material properties of interest; (3) universality to allow efficient computation from distinct multi-modal imaging data and to enable data fusion for microstructure modeling; (4) interpretability to allow easy and intuitive understanding of the key morphological features in the material systems and their evolution from the representations.

Actually, according to the computational results and our observation in chapter 3, P_n functions which is the subset of the S_n functions do can equip these four significant factors to efficiently describe the feature of microstructure and its evolution to provide a valid, and reliable algorism of quantification.

Additional, In order to let P_n functions can be more efficiently to be utilized, we still need to find an easier method to analyze the results of material's evolution. I believe that some people will ask me what do you mean? Actually, from the curves of Figure 3. 13, we can know that 3 sample imaging will cause 3 curves for every P_n functions. For the same reason, if we extract more imaging, e.g. 1500 imaging, from an evolution processing to analyze, the high-dimensioned results of total 7500 curves of P_n functions (n=2, 3, 4, 6 and 8) will cause dazzling chaos contrarily even P_n functions do can provide the reliable quantification of configuration for each evolving imaging. For this circumstance, I will discuss 2 methods named Omega Metric and Differential Omega Metric in Chapter 5 to overcome this shortage.

CHAPTER 4

MICROSTRUCTURE RECONSTRUCTION PROCEDURE AND ITS APPLICATION BASED-ON GIVEN P_n FUNCTION

P_n functions are a set of hierarchical statistical descriptors known as the "n-point polytope functions" P_n which are subset from the standard n-point correlation functions S_n. That is why P_n functions can efficiently include higher-order n-point statistics of the morphological and topological features of interested phase in a concise, explainable, and expressive manner. In view of above mentioned reasons, I will try to use the given data sets of P_n functions to reconstruct its original microstructure in this chapter [59]. Actually this is really a challenge to be achieved and realized because reconstructing a complex structure has infinite combination and permutation. Although the confirmed information of P_n functions are known to realize the reconstruction, the probability of diverse microstructures having same P_n functions still exists because their some specific geographic shape of inclusion and the related connectivity between every inclusion. To overcome this hindrance, I use the algorism of Yeong-Torquato (YT) reconstruction procedure [61][62] to find the optimal results of reconstruction which are really converging to the real model. The reliable and valid results of reconstruction can be useful for material engineers who analyze, invent and design new materials.

In this chapter, I will introduce the basic algorism of reconstruction and the reconstructed results of model with simplified particles, the comparison of schematic with arranged spheres and the difference of imaging with real material particle to obtain more information content about reconstruction via P_n functions.

4.1 Realization Rendering via Stochastic Optimization

In order to obtain more accurate result of reconstruction. I use the algorism of Yeong-Torquato (YT) reconstruction procedure to generate virtual 2D microstructures from a specific set of P_n functions with n value equals to 2, 3, 4, 6 and 8 in this chapter. Actually, one can use YT procedure to generate virtual 3D microstructures as well when one use 3D template of P_n functions. For sure, you can collect all the virtual 2D probability map to produce virtual 3D reconstruction but it's result may not so reliable when it compare the result which is created by the 3D template of P_n functions [59].

When I embark on the research about reconstruction, actually there are a great deal of other different microstructure reconstruction procedures, such as the Gaussian random field method [63], phase recovery method [64], and the recently developed raster path method [65]. These algorisms are reliable but they have some limitation when we want to use these methods to reconstruct the virtual model. In order to reconstruct more and more general cases, I adopt the YT procedure which enables anyone to incorporate an arbitrary number of correlations of any type, while the others require specific structural information as input. Because the YT procedure is equipped with such unique, flexible and generalized feature of algorism, it can help one to get the more optimal reconstruction results by choosing effective P_n functions. In other words, one can sift out some nonobvious P_n functions and consider contributed P_n functions to reconstruct the virtual model. I will describe my result of trials about how to find the most effective P_n functions to concise all the reconstruction procedure in the later paragraphs.

In the YT procedure, the way to reconstruct the model is formulated as an "energy" minimization problem, with the energy functional E defined as follows

$$E = \sum_n \sum_\beta \sum_r \left[P_n^\beta(r) - \bar{P}_n^\beta(r) \right]^2 \quad (4.1)$$

Where $\bar{P}_n^\beta(r)$is a target polytope function of order n along direction β and $P_n^\beta(r)$ is the corresponding function associated with a trial realization. In fact, he energy functional E is also known as least-square error. In this chapter, I incorporated P_2, P_3, P_4, P_6, and P_8 into energy functional E of YT procedure. In order to get the optimum reconstruction results, the simulated annealing method [76][77] is usually employed to solve the aforementioned minimization problem by switching the pixels to the most ideal reconstruction. Specifically, starting from an initial trial microstructure (i.e., old microstructure/randomly arranged microstructure) which contains the same number of voxels (3D)/pixels (2D) of target model for each phase. Then two randomly chosen voxels/pixels belonged to different phases are exchanged to generate a new trial microstructure (Figure 4. 1). This new trial microstructure's relevant correlation functions are computed and its associated energy is evaluated, which determines whether the new trial microstructure should be accepted or not via the probability:

$$p_{acc}(old \to new) = \min\left\{1, \quad \exp\left(\frac{E_{old}}{T}\right) \Big/ \exp\left(\frac{E_{new}}{T}\right)\right\} \quad (4.2)$$

Where T is a virtual temperature that is chosen to be high initially and slowly decreases with the rate of change of T according to a cooling schedule [58][60]. When $E_{new} < E_{old}$, the new trial microstructure is accepted because its value is bigger than 1 when index of exponential function is positive. However, when $E_{new} > E_{old}$, one can determine the new trial microstructure will not be accepted but if we use this algorism, its energy may be confines in the local energy minima because its energy does have any chance jump to the lower energy position. In order to compute more optima reconstruction, I adopt Monte Carlo steps (P_M) to ensure that the trial microstructure will not be trapped in the local energy minima to obtain more accurate results (Figure 4. 2). When $P_M < \exp[(E_{old} - E_{new})/T]$, I also accept the new trial

microstructure to ensure that the trial microstructure will not be trapped in the local energy minimum to obtain more accurate results (Figure 4. 2). The aforementioned process is repeated until E is smaller than a prescribed tolerance, which we choose to be 10^{-6} here. Generally speaking, several hundred thousand trials need to be made to achieve such a small tolerance for a valid case [59].

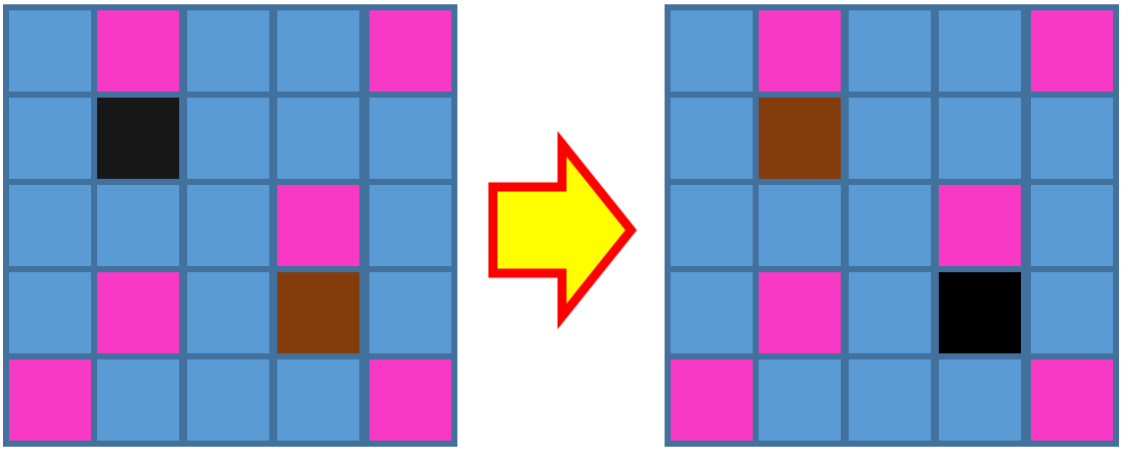

Figure 4. 1 Schematic Illustration of the Pixel Exchange Procedure for Generating A New Microstructure Based on An Old Microstructure.

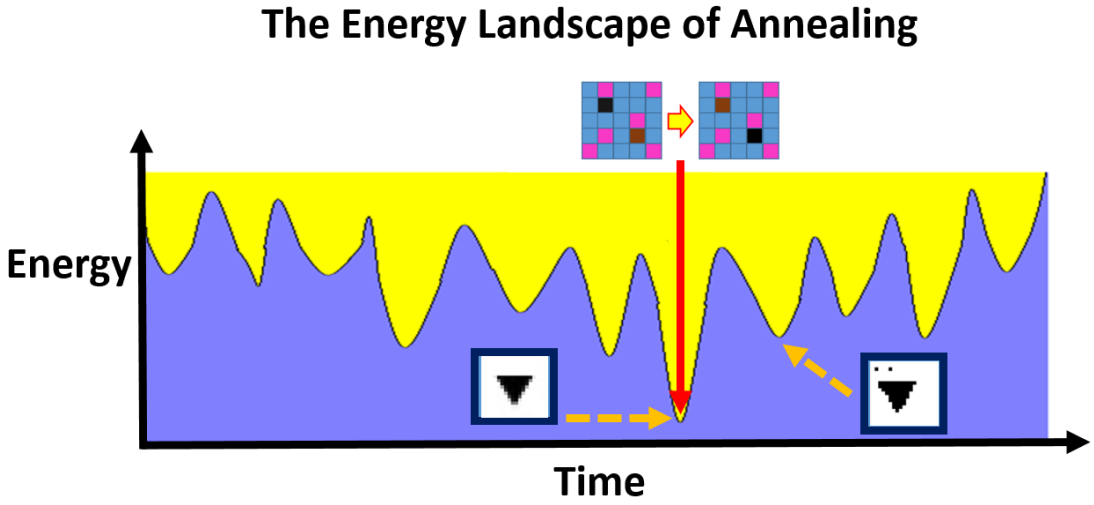

Figure 4. 2 Schematic Illustration of the Simulated Annealing Optimization Procedure for Reconstruction. The Initial Uphill Moves Allow the System to Escape from Local Energy Minimum.

According to the reconstruction procedure, it can be clearly seen that the key step in the reconstruction process is to efficiently compute the correlation functions and energy E from the trial microstructure to decide if the trial microstructure will be accepted or not.

That is why how to efficiently compute the correlation functions from the trial microstructure which is especially crucial for the reconstruction of large-scale 3D/2D realizations. The key idea is to only compute the related P_n functions of randomly selected pixel pair due to the switch, instead of re-compute the functions from scratch. We can implement this ideal by deducting the success number of the black pixels and adding the success number of white pixels before pixel pair switch because I only exchange 2 pixels which belong different phase. After collecting the all affected numerators of the P_n functions and re-computing the contributions from these templates after the pixel exchange, we can acquire the P_n functions of the randomly selected pixel pair and no one need to recalculate the switched structure. It will save tremendous time and computer resource to efficiently compute the trial realizations.

However, we note that when n gets larger, the number of affected n-polygonal templates also increases rapidly. Sometimes, how to find the affected pixels due to exchanging two pixels belonged to different phase will becomes more difficult and intricate. Since our focus in this chapter is to probe the information content of the hierarchical set of P_n functions for relatively small 2D systems (e.g., 100 by 100 pixels), we can just re-compute the P_n functions from new trial realizations without extremely increasing the computational cost. Under this basis, I re-compute all the P_n functions for old trial realizations to decide if it's acceptable to be placed as the new trial or not to proceed the reconstruction procedure.

4.2 Realization of Reconstruction of Simplified Model

In order to verify the reliability of algorism of reconstruction, I first choose directional sampling template of n=3, 4, 6 and 8 (shown as Figure 4. 3) to compute relative P_n functions (P_3, P_4, P_6 and P_8) for simple images which contain single equilateral tringle, square, regular hexogen and regular octagon particles separately (shown as Figure 4. 4) and then use the computed P_n functions to reconstruct their original structure to compare if the reconstructed results are reasonable or not.

Besides, I also adopt the periodic boundary condition to let the reconstruction simulation simplified. Moreover, I utilize the image which only contain "matrix phase" (while pixels) and "particle phase" (black pixels) to predigest the whole procedure of getting P_n functions and reconstruction, and the size of all imaging is 20 by20 pixels.

When I compute the P_n function and execute the reconstruction procedure, the whole procedure, setting and parameters are the same to ensure the results of reconstruction are comparable and interpretable.

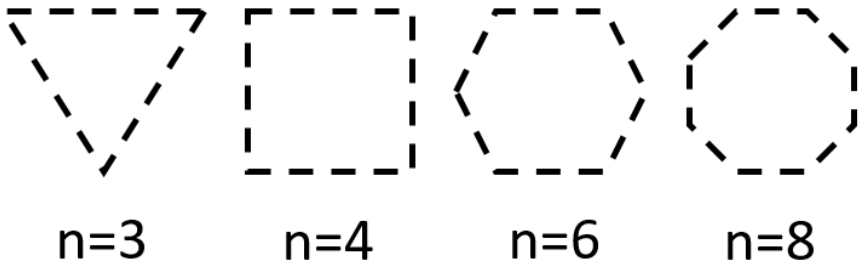

Figure 4. 3 Illustration of the Different Shapes of the Sampling Templates for the P_n Functions With Various Value n.

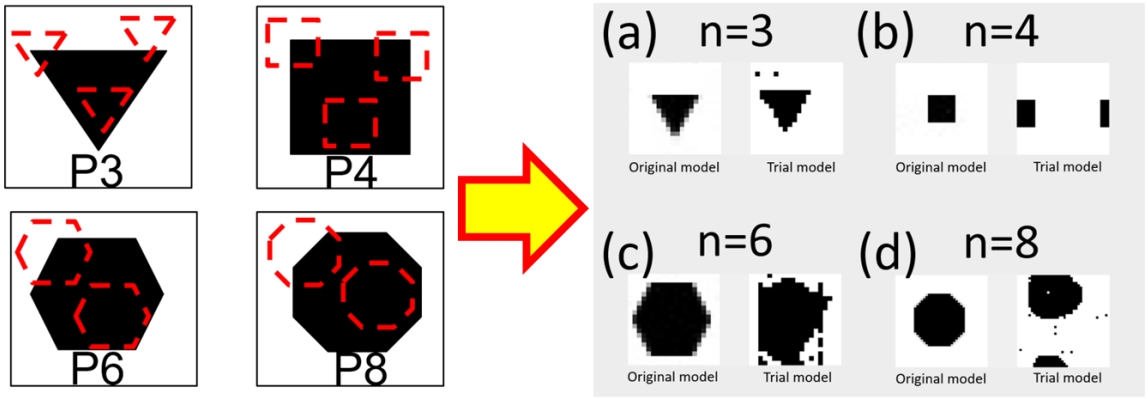

Figure 4. 4 Reconstruction Results of Imaging Which Contain Single (a) Equilateral Tringle, (b) Square, (c) Regular Hexogen and (d)Regular Octagon Particles by Using Their Related P_3, P_4, P_6, and P_8 Separately.

Because P_n functions can provide a systematic "decomposition" of the features of interest in the microstructure in terms of a series of polytope basis and effectiveness about capturing hidden symmetry/spatial orders in the system, we finally acquire a very solid and valid results from reconstruction procedure.

For single equilateral tringle particle imaging shown as Figure 4. 4 (a), we can easily tell that the trial/reconstructed model is pretty similar to its original model because sampling template (n=3) can efficiently provide its geometry fitting to the whole reconstruction procedure. Besides, the trial model is shifted its location to the upper place a little bit, for I use the periodic boundary conditions which are often chosen for approximating a large (infinite) system to avoid getting a simulation results affected by boundary interference. Averaging speaking, the trial microstructure is valid and reasonable compared to the real model.

For single square particle imaging shown as Figure 4. 4 (b), we can observer that the trial microstructure is also shifted but its overall result is under our expectation. If we imagine the trial microstructure is a unit cell and we can use it to make up an infinity plane then we can obtain a whole square shown as Figure 4. 5. The most significant character of

reconstruction of equilateral triangle and square is that all the pixels can automatically converge into connected particles.

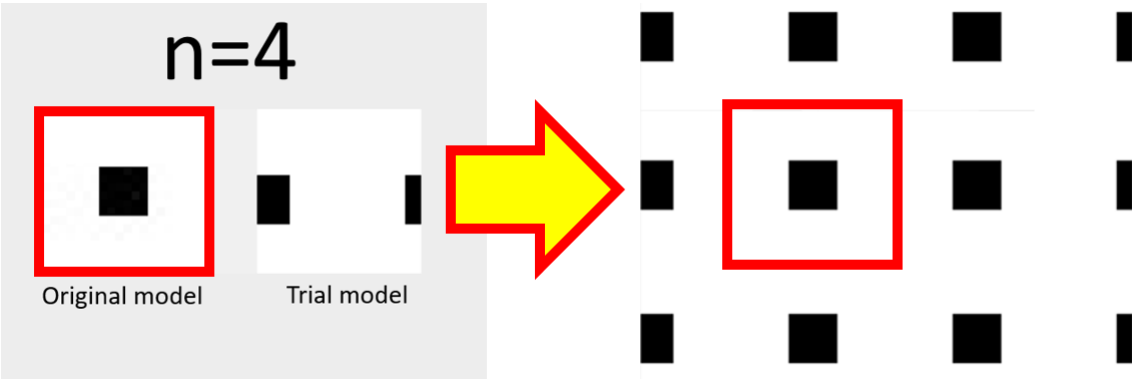

Figure 4. 5 Reconstruction Results of Figure 4. 4 (b) Under Periodic Boundary Conditions.

For single regular hexagon and octagon particle imaging shown as Figure 4. 4 (c) and Figure 4. 4 (d), we can easily distinguish that the geography results of these two reconstruction are not really similar to the original model but the convergent character of their result shows that P_n functions which still can be usefully used to sift and restore the critical geometric information even the target image has more complex shape of the interested phase. How to improve our reconstruction results? Actually, when I choose regular hexagon template (i.e. n=6) and I use this template to compute the P_n functions of image which is constructed with single hexagon particle, we easily underestimate and neglect some important factors. Form the point view of geometry, hexagon can be combined and created with equilateral triangles which is the subset unit can more thoroughly describe the connected, dispersed and geometric relationship of the ambient interested pixels. The similar result will be obtained when I use regular octagon template (i.e. n=8) to compute the P_n functions of image which is constructed with single octagon particle The reconstruction result of image which is constructed with single octagon particle, i.e. Figure 4. 4(d), under PBC setting is shown as Figure 4. 6.

That is why only using the higher rank of P_n functions to compute the image which has complex particles sometimes cause distorted reconstruction. One can add lower rank of P_n functions to attain more accurate results. In other words, one can cooperate with different results of calculated P_n functions to reconstruct the microstructure. That is why I select YT reconstruction procedure as my algorism to reconstruct the model because its formula can combine the required P_n functions as many as I want. Moreover, when interested particles have more complex geometry, one need to consider to add lower P_n functions to compute and describe its relationship of configuration according to the different cases..

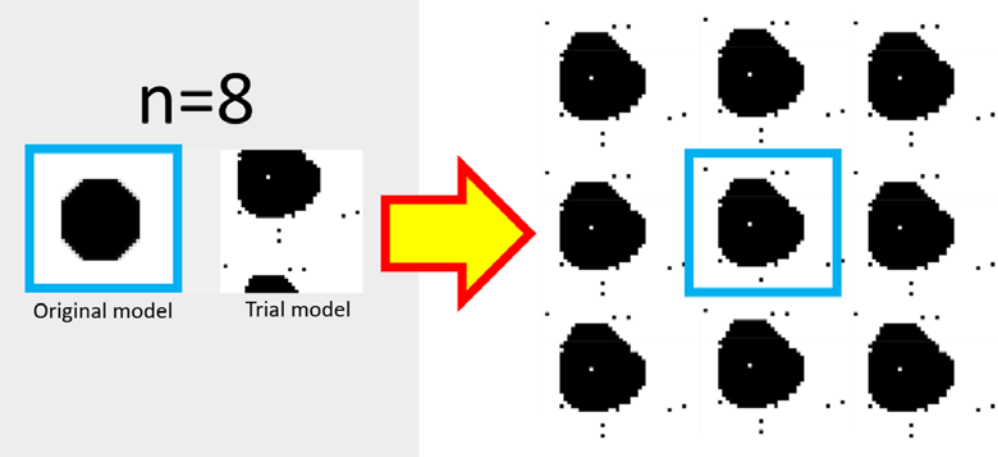

Figure 4. 6 Reconstruction Results of Figure 4. 4(d) Under Periodic Boundary Conditions.

4.3 Information Content of P_n Functions via Realization Rendering

In the last section, I already introduce simplified imaging which only contain single particle with different geometric shape and their reconstruction results. In this section, I will investigate the information content of the P_n functions using a serious of heterogeneous systems, including ordered and disordered particle packings respectively representing crystalline and liquid state of matters, overlapping particles with a Poisson distribution of particle centers, interpreting microstructure of metal-ceramic composite, and concrete

microstructure. This is achieved by incorporating additional P_n functions of successively higher orders into the realization reconstructions, starting with the fundamental two-point function P_2 (or equivalently S_2). But the challenging comes, how to decide our reconstruction results are valid? The accuracy of the reconstructed realizations are subsequently accessed using statistical descriptors that are not used in the reconstruction, such as the lineal-path function $L(r)$ [39] [73], which provides the probability that a randomly placed line segment of length r entirely lying in the phase of interest. In particular, the lineal-path function $L(r)$ will be computed from both the original system and the reconstructed realization. The accuracy metric ψ, defined as the sum of the absolute differences of these two functions over all r values, will also be computed, i.e.,

$$\psi = \sum_r [L(r) - L^*(r)] \tag{4.3}$$

Where $L(r)$ and $L^*(r)$ are respectively computed from the reconstructed realization and the original system. The level of accuracy of the realizations, quantified via ψ, reflects the statistical information encoded in the P_n functions. The lesser value ψ is, the higher accuracy it has. For example, higher accuracy indicates essential additional structural information is encoded in the newly added functions. In the following realization rendering cases, the size of the reconstructed system is 80 by 80 pixels without further elaboration, and periodic boundary conditions are employed.

4.3.1 Ordered Packing of Congruent Spheres

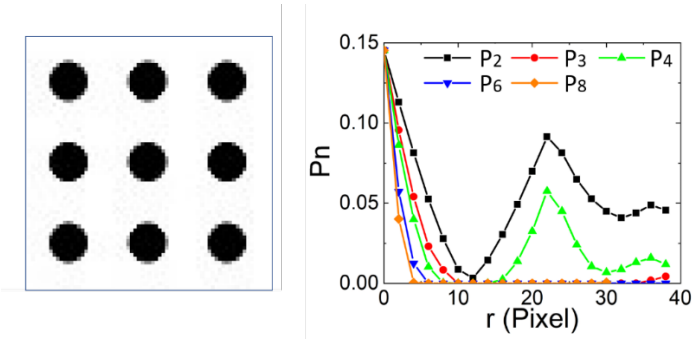

Figure 4. 7 A simple 2D Crystalline Packing of Congruent Spheres on A Square Lattice (Left) and the Associated P_n Function for the Particle Phase (Right).

We begin with a simple 2D crystalline packing of congruent spheres on a square lattice (see Figure 4. 7(left)) [59]. The volume fraction of the particle phase is phi = 0.14. It can be clearly seen from Figure 4. 7(right) that both the P_2 (i.e., S_2) and P_4 functions exhibit strong oscillations, which is the manifestation of the underlying 4-fold symmetry of the structure. The other P_n functions (i.e., n=3, 6, 8) do not exhibit significant oscillation beyond an initial decay, reflecting the fact that the system is composed of compact particles as building blocks, but does not possess strong n-point correlations on large length scales.

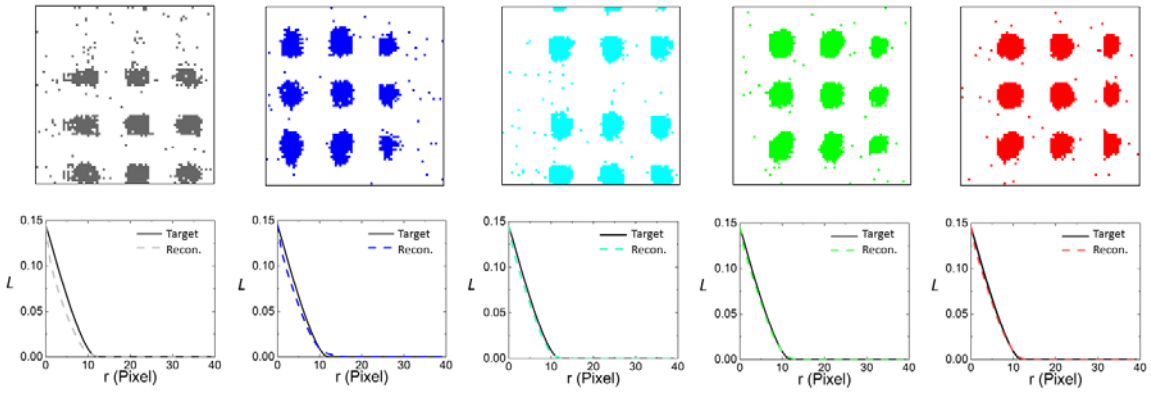

Figure 4. 8 Realizations of 2D Crystalline Packing of Congruent Spheres on A Square Lattice (Upper Panels) and the Associated Lineal-Path Functions (Lower Panels) Obtained via Stochastic Reconstruction by Successively Incorporating Higher-Order P_n Functions. The Functions Incorporated from Left to Right Are Respectively: P_2, $\{P_2, P_3\}$, $\{P_2, P_3, P_4\}$, $\{P_2, P_3, P_4, P_6\}$, and $\{P_2, P_3, P_4, P_6, P_8\}$.

Figure 4. 8 shows the realizations (upper panels) obtained via stochastic reconstruction by successively incorporating higher-order P_n functions [59]. The functions incorporated from left to right are respectively: P_2, $\{P_2, P_3\}$, $\{P_2, P_3, P_4\}$, $\{P_2, P_3, P_4, P_6\}$, and $\{P_2, P_3, P_4, P_6, P_8\}$. It can be seen that the spatial arrangement of the particles on the square lattice is reproduced in all cases. This is because the structural information for the highly ordered 4-fold symmetric arrangement is already captured by the lowest order function P_2, which is further reinforced by incorporating P_4. Interestingly, the shape of the particle is improved due to incorporation of additional functions, i.e., P_3, P_6, and P_8. This is consistent with information content of these functions, i.e., P_3, P_6, and P_8 functions do not possess long-range oscillations and thus, only encode information on the morphology of the particles. The lineal-path functions $\boldsymbol{L}$ are computed from the reconstructed realizations and compared to that of the original system (see Figure 4. 8, lower panels). It can be seen as higher order P_n functions are successively incorporated, the $\boldsymbol{L}$ function of the reconstructed realizations matches the original system better. This is consistent with the quantification using accuracy metric shown in Figure 4. 9 [59].

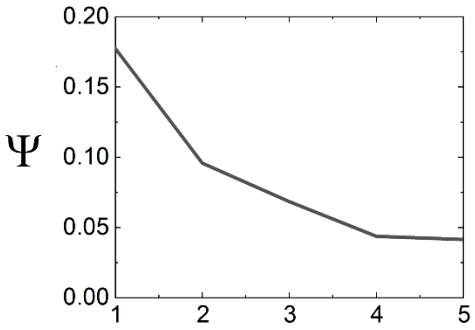

Figure 4. 9 Accuracy Metric ψ Defined in Eq. (4) Associated with Reconstructions Incorporating Different Sets of P_n Functions. The Horizontal Axis Indicates the Number of Functions Incorporated in the Reconstruction.

4.3.2 Disordered Packing of Congruent Spheres

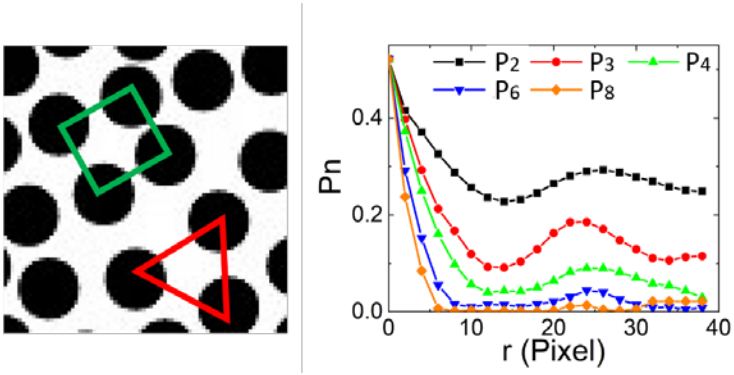

Figure 4. 10 A 2D Disordered Packing of Congruent Hard Spheres Generated via Monte Carlo Simulations (left) and the Associated P_n Function for the Particle Phase (Right).

Figure 4. 10 shows the quantification of a 2D microstructure composed of equal-sized hard spheres in a matrix [58], i.e., a packing (see Figure 4. 10, left panel) [59]. The sphere packing is generated using Monte Carlo simulations [48]. The P_n functions for the particle phase with n =2, 3, 4, 6 and 8 are shown in Figure 4. 10 right panel. Similar to the crystalline packing case discussed in Sec. 4.3.1, all P_n functions initially decay from the volume fraction Φ=0.48 as r increases from 0. The positions of the first minimum in the P_n functions for small n values roughly correspond to the linear size of the particle (~ 12 pixels). After the initial decay, all P_n functions studied here except for n = 8 exhibit relatively significant oscillations and the first peaks in different P_n functions occur at approximately the same r values. These oscillations respectively indicate strong pair, triangle, square and hexagonal correlations on different length scales in the system. In Figure 4. 10, we illustrate examples of such correlations, which are all associated with the mean nearest neighbor separate distance, i.e., the distance associated with the first peak in P_2. These correlations result from the tendency for the particles to self-organize at high densities [59].

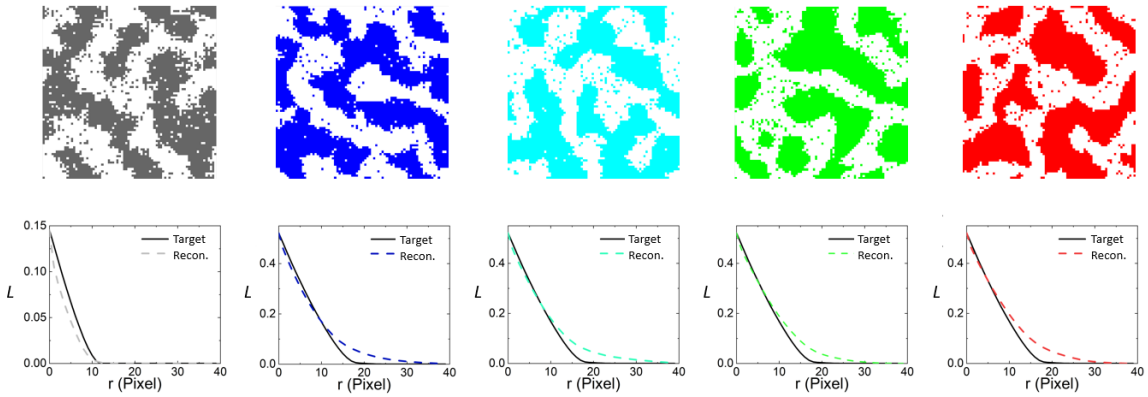

Figure 4. 11 Realizations of Disordered Packing of Congruent Hard Spheres (Upper Panels) and the Associated Lineal-Path Functions (Lower Panels) Obtained via Stochastic Reconstruction by Successively Incorporating Higher-Order P_n Functions. The Functions Incorporated from Left to Right Are Respectively: P_2, $\{P_2, P_3\}$, $\{P_2, P_3, P_4\}$, $\{P_2, P_3, P_4, P_6\}$, and $\{P_2, P_3, P_4, P_6, P_8\}$.

Figure 4. 11 shows the realizations (upper panels) obtained via stochastic reconstruction by successively incorporating higher-order P_n functions [59]. The functions incorporated from left to right are respectively: P_2, $\{P_2, P_3\}$, $\{P_2, P_3, P_4\}$, $\{P_2, P_3, P_4, P_6\}$, and $\{P_2, P_3, P_4, P_6, P_8\}$. It can be seen that in all reconstructions, the connectivity of the particle phase has been significantly overestimated. In particular, instead of reproducing individual compact particles, a single connected phase with a characteristic ligament size comparable to the sphere diameter is produced. The strong oscillation in the correlation functions is realized by the inter-ligament spacing and correlations. This is because the particle volume fraction Φ=0.48 is close to percolation [78] [79]. These results also indicate that the P_n functions (up to n = 8) do not encode topological connectedness information. On the other hand, it has been shown that incorporating cluster functions [39][45] can lead to significantly improved reconstructions capturing the connectivity information. The lineal-path functions L also are computed from the reconstructed realizations and compared to that of the original system (see Figure 4. 11 lower panels). Since L is sensitive to clustering, which is overestimated in all

realizations, successively incorporating higher-order P_n functions does not lead successively more accurate reconstruction. Instead, the more complex energy landscape associated with higher-order P_n functions might lead to slower convergence of the reconstruction, and higher probability that the system gets stuck in a shallow local minimum [59]. This is consistent with the quantification using accuracy metric shown in Figure 4. 12 [59].

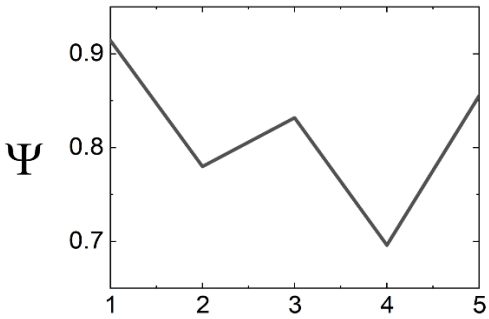

Figure 4. 12 Accuracy Metric ψ Defined in Eq. (4) Associated with Reconstructions Incorporating Different Sets of P_n Functions. The Horizontal Axis Indicates the Number of Functions Incorporated in the Reconstruction.

4.3.3 Overlapping Congruent Spheres

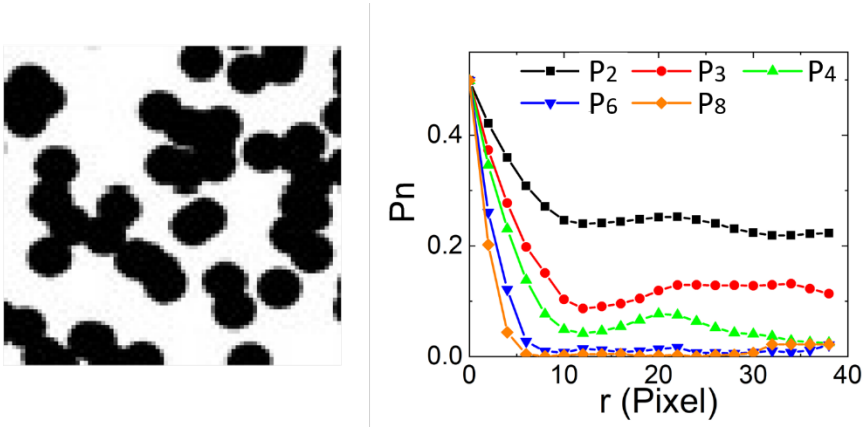

Figure 4. 13 A 2D Disordered Packing of Congruent Overlapping Spheres With a Poisson Distribution of the Particle Centers (Left) and the Associated P_n Function for the Particle Phase (Right).

Figure 4. 13, shows the quantification of a 2D microstructure composed of equal-sized overlapping spheres in a matrix [48][59] (see Figure 4. 13, left panel). The spheres are randomly placed in the matrix without any built-in spatial correlations. Figure 4. 13, right panel shows the P_n functions for the particle phase with n =2, 3, 4, 6 and 8. Similar to the previous systems, all P_n functions initially decay from the volume fraction Φ=0.47 as r increases from 0. After the initial decay, the P_n functions are virtually flat, indicating that the particles possess no spatial correlations of any symmetry on any length scales beyond the diameter of the particles. We note that for the totally random overlapping sphere system, the P_n functions possess the analytical expression $P_n(r) = \exp[-\varrho v_n(r; R)]$, where ϱ is the number density of the spheres in the system (i.e., number of spheres per unit volume) and $v_n(r; R)$ is the volume of the union of n spheres with radius R with centers placed at the vertices of a n-polytope with edge length r.

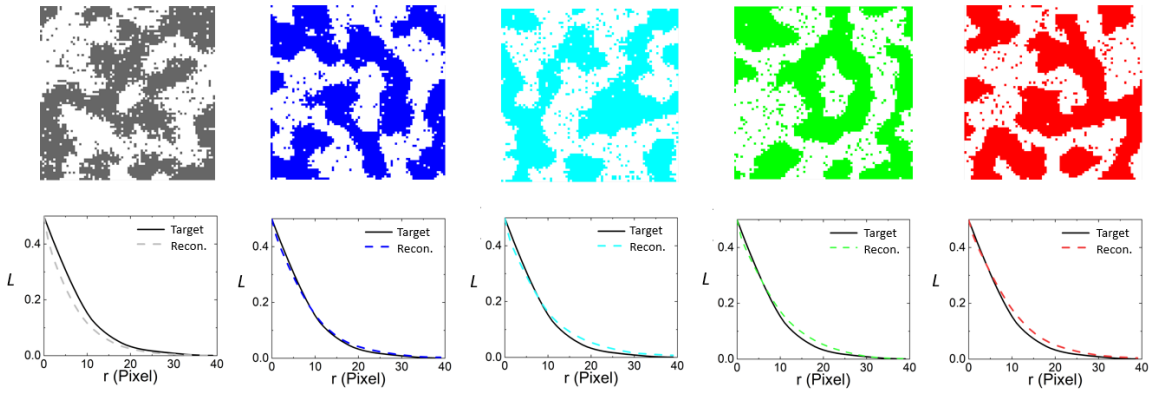

Figure 4. 14 Realizations of Overlapping Sphere Packing (Upper Panels) and the Associated Lineal-Path Functions (Lower Panels) Obtained via Stochastic Reconstruction by Successively Incorporating Higher-Order P_n Functions. The Functions Incorporated from Left to right Are Respectively: P_2, $\{P_2, P_3\}$, $\{P_2, P_3, P_4\}$, $\{P_2, P_3, P_4, P_6\}$, and $\{P_2, P_3, P_4, P_6, P_8\}$.

Figure 4. 14 shows the realizations (upper panels) obtained via stochastic reconstruction by successively incorporating higher-order P_n functions [59]. The functions incorporated from left to right are respectively: P_2, $\{P_2, P_3\}$, $\{P_2, P_3, P_4\}$, $\{P_2, P_3, P_4, P_6\}$, and $\{P_2, P_3, P_4, P_6, P_8\}$. In all the reconstructions, the connectivity of the particle phase has been correctly reproduced, as the overlapping particles in the original system form a single connected phase, in contrast to the hard sphere packing case. Since all the P_n functions contains no essential information beyond the particle diameter (~ 12 pixels), incorporating these functions does not lead to improvement of the reconstruction accuracy for the overlapping sphere system. This is consistent with the quantification using accuracy metric shown in Figure 4. 15 [59].

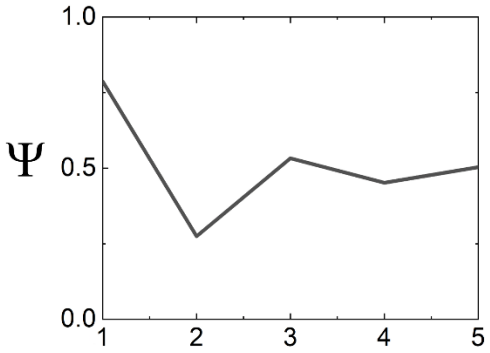

Figure 4. 15 Accuracy Metric ψ Defined in Eq. (4) Associated with Reconstructions Incorporating Different Sets of P_n Functions. The Horizontal Axis Indicates the Number of Functions Incorporated in the Reconstruction.

4.3.4 Concrete Microstructure

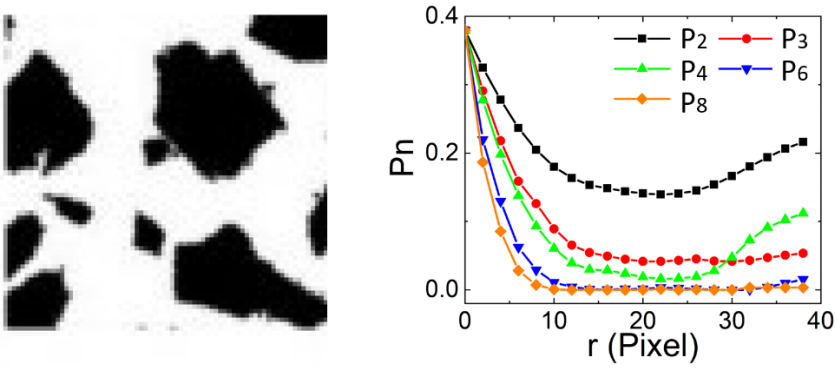

Figure 4. 16 A 2D Slice of a Concrete Microstructure in Which the Cement Paste Is Shown in White and the Rocks Are Shown in Black (Left) and the Associated P_n Function for the Rock Phase (Right).

Figure 4. 16 shows the quantification of a 2D concrete microstructure composed of reinforcement rocks (shown in black) and the cement paste (shown in white) [52] [59] (see Figure 4. 16, left panel). The rock particles possess complex polygonal morphologies and a wide size distribution. Figure 4. 16 right panel shows the P_n functions for the rock phase with n =2, 3, 4, 6 and 8. All P_n functions initially decay from the volume fraction Φ=0.38 as r increases from 0. The r value associated with the first minimum in the functions provides the average particle size in the system, i.e., ~ 20 pixels. After the initial decay, the lower-order P_n

functions (e.g., n≤4) increase, reflecting the spatial correlations resulted from the mutual exclusion effects of the rock particles. The correlations are much weaker compared those in hard-sphere systems, mainly due to the anisotropy and size polydispersity of the rock particles.

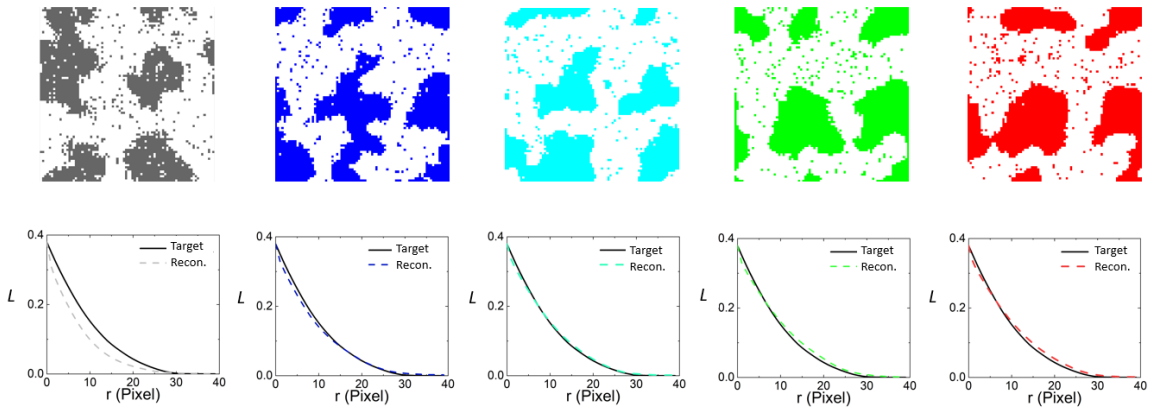

Figure 4. 17 Realizations of Concrete Microstructures (Upper Panels) and the Associated Lineal-Path Functions (Lower Panels) Obtained via Stochastic Reconstruction by Successively Incorporating Higher-Order P_n Functions. The Functions Incorporated from Left to Right Are respectively: P_2, $\{P_2, P_3\}$, $\{P_2, P_3, P_4\}$, $\{P_2, P_3, P_4, P_6\}$, and $\{P_2, P_3, P_4, P_6, P_8\}$.

Figure 4. 17 shows the realizations (upper panels) obtained via stochastic reconstruction by successively incorporating higher-order P_n functions [59]. The functions incorporated from left to right are respectively: P_2, $\{P_2, P_3\}$, $\{P_2, P_3, P_4\}$, $\{P_2, P_3, P_4, P_6\}$, and $\{P_2, P_3, P_4, P_6, P_8\}$. In the reconstructions, individual rock particles can be clearly distinguished. As higher-order P_n functions are successively incorporated, the shape and morphology of the rock particles are improved. This can be seen both from visual inspection of the reconstructed realizations and the quantitative comparison of the lineal-path functions (Figure 4. 17, right lower panels). In the case that a larger number of P_n functions are incorporated, the complexity of energy landscape increases dramatically, leading to very slow convergence of the reconstruction. This also leads to the slight increase of ψ shown in Figure 4. 18 [59].

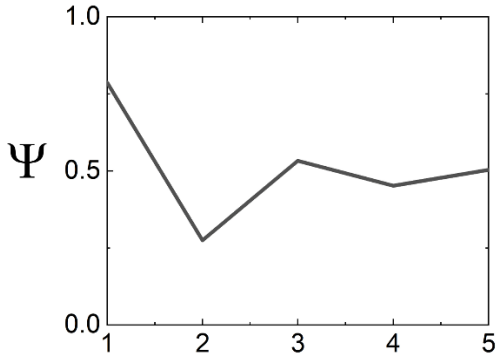

Figure 4. 18 Accuracy Metric ψ Defined in Eq. (4) Associated with Reconstructions Incorporating Different Sets of P_n Functions. The Horizontal Axis Indicates the Number of Functions Incorporated in the Reconstruction.

4.3.5 Interpenetrating Metal-Ceramic Composite

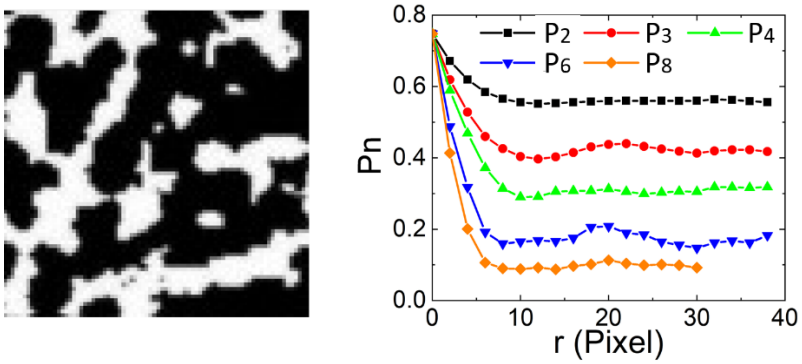

Figure 4. 19 A 2D Slice of A Interpenetrating Microstructure of a Metal-Ceramic Composite Composed of the Boron-Carbide Phase (Black) and the Auminum Paste (White) (Left) and the Asociated P_n Function for the Boron-Carbide (Ceramic) Paste (Right).

Figure 4. 19 shows the quantification of a 2D an interpenetrating metal-ceramic composite composed of the boron-carbide phase (shown in black) and the aluminum phase (shown in white) [51][59] (see Figure 4. 13(a)). This system contains "ligaments" of similar width instead of "particles", and possesses connected material phase, in contrast to the hard particle packings. Figure 4. 19 right panel shows the P_n functions for the ceramic phase with n =2, 3, 4, 6 and 8. Similar to the previous systems, all P_n functions initially decay from the volume fraction Φ=0.76 as r increases from 0. The r value associated with the first minimum

in the functions provides the average ligament width in the system, i.e., ~ 10 pixels. After the initial decay, the P_n functions exhibit weak oscillations for small and intermediate r values, characterizing the exclusion effects between the ligaments.

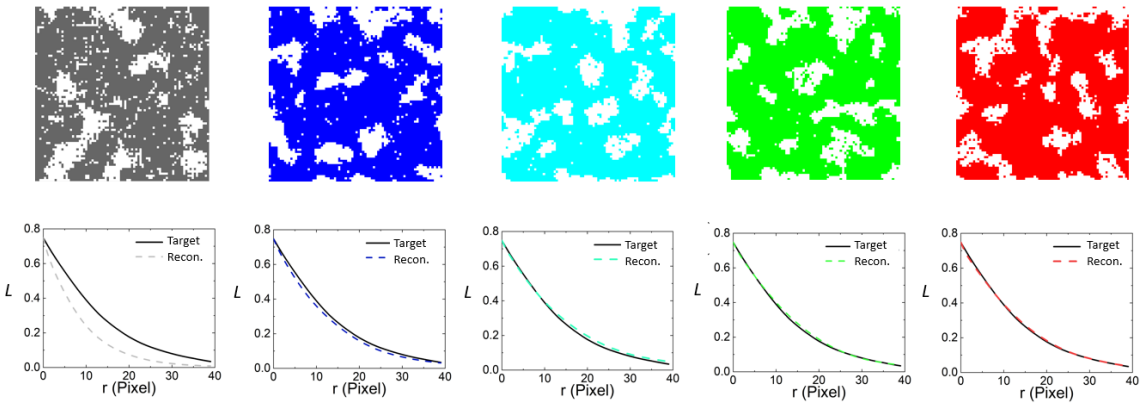

Figure 4. 20 Realizations of the Interpenetrating Microstructure (Upper Panels) and the Associated Lineal-Path Functions (Lower Panels) Obtained via Stochastic Reconstruction by Successively Incorporating Higher-Order P_n Functions. The Functions Incorporated from Left to Right Are Respectively: P_2, $\{P_2, P_3\}$, $\{P_2, P_3, P_4\}$, $\{P_2, P_3, P_4, P_6\}$, and $\{P_2, P_3, P_4, P_6, P_8\}$.

Figure 4. 20 shows the realizations (upper panels) obtained via stochastic reconstruction by successively incorporating higher-order P_n functions [59]. The functions incorporated from left to right are respectively: P_2, $\{P_2, P_3\}$, $\{P_2, P_3, P_4\}$, $\{P_2, P_3, P_4, P_6\}$, and $\{P_2, P_3, P_4, P_6, P_8\}$. In all the reconstructions, the morphology and connectivity of both the ceramic and metallic phases have been very well reproduced. As can be seen from the comparison of the lineal-path functions (Figure 4. 20, lower panels) and the accuracy metric ψ (see Figure 4. 21), including higher-order P_n functions leads to successively improved reconstructions. This indicates that the additional morphological information encoded in higher-order P_n functions has been efficiently utilized in the reconstructions. We note that it is relatively easier for the reconstruction algorithm to converge to a realization with connected phase at high volume fractions, as such realizations are more degenerate [37][38]. Therefore,

it is common that better reconstruction accuracy can be achieved for systems where the phase of interest (i.e., the ceramic phase) is connected [59].

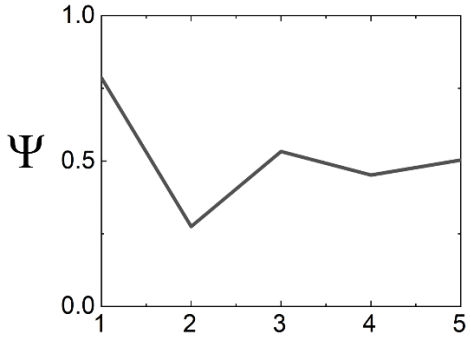

Figure 4. 21 Accuracy Metric ψ Defined in Eq. (4) Associated With Reconstructions Incorporating Different Sets of P_n Functions. The Horizontal Axis Indicates the Number of Functions Incorporated in the Reconstruction.

4.4 Conclusions and Discussion of Reconstruction

In this chapter, we employ stochastic realization reconstruction to probe the level of statistical morphological information contained in a recently introduced set of hierarchical statistical microstructural descriptors, i.e., the "*n*-point polytope functions" P_n. The P_n (r) function provides the probability of finding a set of n points sitting at the vertices a regular n-polytope of edge length r in the phase of interest, and thus, is a subset of the corresponding standard n-point correlation function S_n. In particular, P_n functions up to n = 8 were successively incorporated into the Yeong-Torquato reconstruction procedure and the accuracy of the reconstructed systems was quantitatively assessing via the lineal-path function, which provides "linear clustering" information. We examined a wide spectrum of representative random systems with distinct geometrical and topological features, including representative crystalline and disordered particle particles, Poisson distribution of particles, microstructures of concrete and interpenetrating metal-ceramic composites.

We found that generally, successively incorporating higher order P_n functions which encodes essential higher-order morphological information leads to superior accuracy of the reconstructions. However, incorporating more P_n functions into the reconstruction also significantly increases the complexity and roughness of the associated energy landscape for the underlying stochastic optimization, making it difficult to convergence numerically. Another observation is that the P_n functions (up to n = 8 studied here) appear to be not sensitive to topological connectedness information. This was evidenced by the significant overestimation of the clustering in the reconstruction of disordered packings of hard spheres near percolation point. These examples indicate that for certain complex systems, successively incorporating higher order correlation functions in a linear fashion might not be the best practice, as one can significantly increase the computational cost without incorporating too much useful additional morphological information. An alternative approach in such cases is to utilize non-conventional functions (e.g., those encoding clustering information) or to employ machine learning techniques to identify and extract crucial higher order correlations that leapfrog unnecessary computation of all the P_n functions[80][81][82].

CHAPTER 5

APPLICATO OF P_n FUNCTIONS FOR VAPOR-DEPOSITION ALLOY FILMS

With the advent of technology, our life have changed dramatically. The invented equipment are manufactured smaller and smaller in size but they contain more and more functions. Take the smart phone for example, it can totally substitutes camera, recorder, scientific calculator, MP3 player, photo editor, GPS navigation, etc.

These days, the most popular topics people or TV always discuss are development of AI (artificial intelligence), 5G equipment, Autonomous vehicle and HPC (high performance computing) which are thoroughly evolving our life. The key factor can let all the virtual concepts and ideas to be realized is that the semiconductor has been created and substituted for traditional circuit board. That is why more and more people currently focus on the manufacture ability of semiconductor in civilian and military industry.

Can you imagine the first super computer is as big as half football court before semiconductor is produced? Why such big equipment can be compacted into nowadays chip which has smaller size than your finger nail and more efficient over thousand-times than outmoded circuit board? Because semiconductor can be created in nanometer size and constructed to form the 3D layered structure to accommodate uncountable circuits. That is why multi-functions can easily be equipped to the designed product.

Under the competitive business environment, how to raise the quality of semiconductor becomes more and more significant target for semiconductor engineers and manufacturers because it indirectly affects the reliability of the designed product and the product's market share. In fact, the process of vapor deposition of semiconductor manufacture plays a decisive role because vapor deposition process usually cause irregular and discontinuous film surface such as pothole or hillock which always lower the conductivity,

smoothness and light transmittance of films. These surface perturbations are hindrances for semiconductor and solar interconnectors. During my search period, I am honor to have opportunity to cooperate with professor Ankit and his team to analysis vapor-deposition of phase-separating alloy by using P_n functions, Omega Metric and Differential Omega Metric. Before I start to calculate and analyze their simulation results, I will brief introduce the main process of making the semiconductor in the next paragraph. In such situation, you can understand why hillocks growth needs to be eliminated, predicted and studied.

5.1 The Procedures to Create Semiconductor

In this paragraph, I will introduce the outline about how to create a semiconductor and describe the importance of vapor deposition process. The flow chart of manufacture is shown as Figure 5. 1.

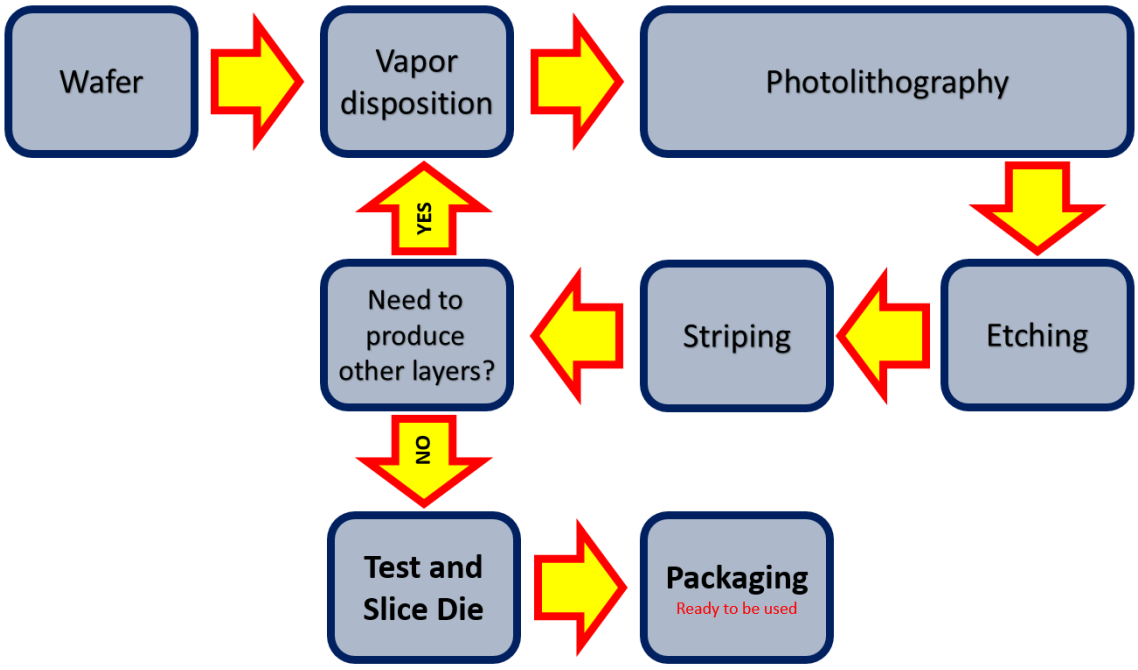

Figure 5. 1 The Flow Chart of Fabrication of Semiconductor.

The first step for creating a semiconductor is that we need a high quality circular silicon wafer which is sliced from silicon ingot and then refined/polished in order to provide the best possible surface, i.e. substrate, for the following fabrication steps.

The second step is the vapor deposition. The implementation of vapor deposition is characterized by a process in which the material much as Cu, Ta, Mo and Ag goes from a condensed/solid phase to a vapor phase and then condenses on the thin film(Figure 5. 2 and Figure 5. 3).

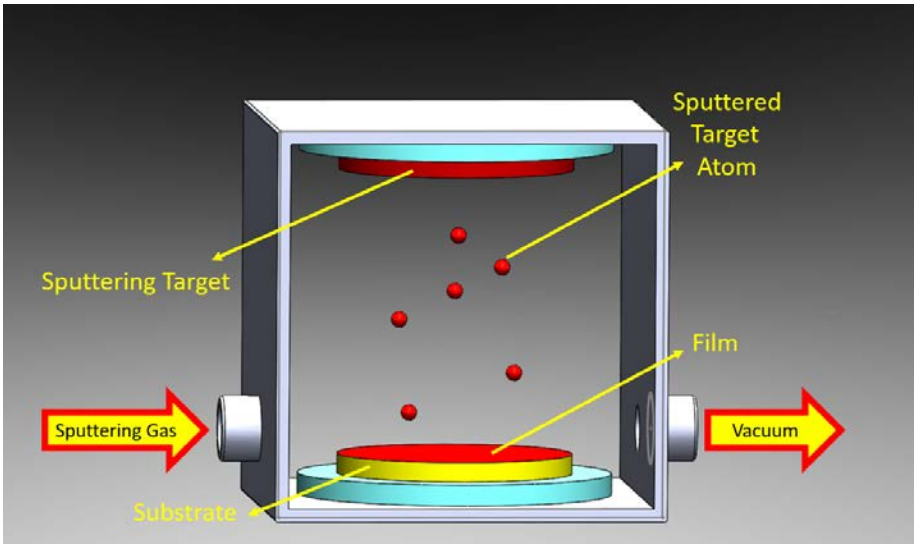

Figure 5. 2 Schematic Illustration of Vapor Disposition' Equipment.

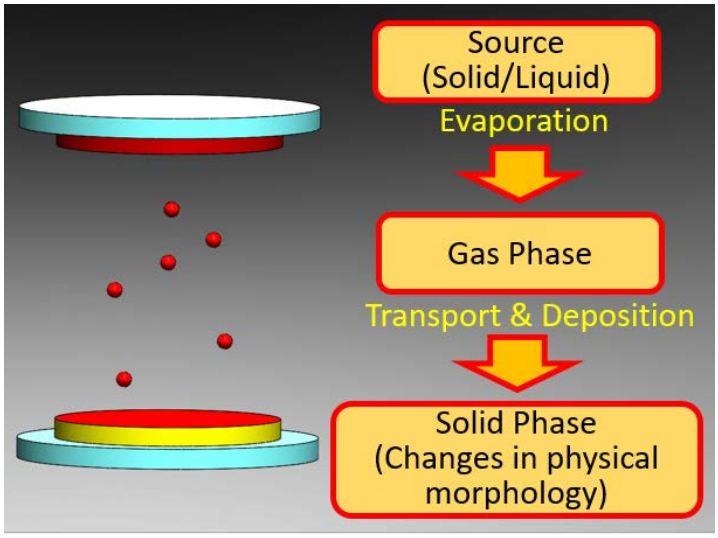

Figure 5. 3 Schematic Illustration of the State Cycle of the Vapor-Decomposition Material.

Vapor deposition is a widespread commercial applications and extensively used in the semiconductor industry to deposit thin films of various materials in integrated circuit processing. For optical application, the thin antireflection coatings on glass are also deposited by vapor deposition to protect the coated glass. Besides, all the items which require thin films for mechanical, chemical or electronic functions can use vapor deposition process to achieve their expectation effect. Examples include thin film solar panels, aluminized PET film, food packaging bag, coated cutting tool, etc. However, since semiconductor and some optical coating are used for precision instrument, the quality of vapor deposition will affect products' life cycle. Take semiconductor for example, the irregular surface will cause potholes and hillocks which will cause open circuit because the microstructure of alloys in the film cannot continuously connected. Under the situation of Nanometer scales, even a dust will cause semiconductor to be broken, not to mention hillock will cause a devastating damage. That is why professor Ankit's work is so important. Besides, if the film's surface is discontinuous, the more error opportunity will be occurred for the next step "the photolithography" because the non-smooth surface will randomly reflect and refract. In such situation, the required removed or kept part of film may not be eliminated or maintained from the film accurately.

The third step is photolithography. The main procedure of photolithography is that a layer of photoresist is spread thinly across the films and wafer. Then let the wafer expose to a UV light mask, which is shaped in the pattern of the designed circuits. Exposed photoresist becomes soluble and is washed off by a solvent. Under this step, the chemical protector can easily applied on the wafer.

The forth step is etching. In this step, eroding chemicals are used to remove unwanted silicon and vapor-deposition material, leaving the wanted material which is protected by the photoresist.

The fifth step is Stripping. In this step, we remove the photoresist by using related solvent. When this step is finished, the designed circuits are produced.

The sixth step is to decide if other layers also are needed to be produced. If the answer is yes, just repeat the procedures from step 2 to step 5. Otherwise, just enter the next step.

The seventh step is test and slice die. When all the designed circuits are built, the wafer is sliced into dies, and functional dies are now ready to be tested on the test machine to make sure all the circuits are well built and functioned.

The final step is packing. When chips pass all the required tests. The chips will be integrated with other chips or parts or circuit board as another assembly. When all the integration is finished, the final assembly will be numbered and packaged.

5.2 The Studies and Important Factors for Phase-Separating Films Making.

From the last paragraph, we can understand that the hillock growth and microstructure of films can directly affect the yield rate of semiconductor's products.

There were lots of researches have studied what mechanisms governing formation of hillocks in monolithic films. Especially, some researches have shown how to control and prevent the growth of hillock [83]-[86]. Besides, more and more prior works also present that thermal stress gradient, temperature, deposition rate, coefficient of thermal expansion and dissimilar mobility [83][87]-[89] are all the main factors should be taken into consideration to generate film made from different metal ingredients.

A recent paper [90] theorized that the morphological transitions were a serious evolution of system's need to lower its internal energy as the deposition rate increased under the energy equilibrium environment. In fact, the structure of immiscible separating-phase has large interface energies compared to the surface energies of alloy components themselves

because of the incoherent of nature of interphase boundaries such as Cu-Ta and Ag-W film [91]-[93]. To let the simulation result of hillock growth of film more accurate, the interphase and phase energy of each phase are all driven into simulation functions of contact angle $\theta_{f,v}$ in order to obtain more precise outcomes. My cooperating team use 3D phase filed approach to numerically simulate the formation of vapor deposition of phase-separating alloy films. The related basis of its simulation will be introduced in the next paragraph.

5.2 The Basis of Simulation of Phase-Separating Alloy Films.

As mentioned before, my cooperating team adopt multi-pronged numerical assesses the role of surface and interfacial energies in the formation of hillocks on the film surface. They supplement the energetics with adatom kinetics to see hillock growth (shown as Figure 5. 5) by assigning an initial condition constituting of spherical perturbations to induce hillock formation from an early stages of vapor deposition. They assign thermodynamic gradient and interaction parameters so as to induce low angles of contact at the film/vapor interface, in order to evaluate the physical morphology of the evolving hillocks as a function of the contact angles. Moreover, to let the simulation can be more real, they also add random noise to simulate the real world vapor-deposition under practically vacuum state.

After a succession of complex and intricate formula derivation, the formula of contact angle, i.e. $\theta_{f,v}$, is obtained.

$$\theta_{f,v} = 2\cos^{-1}\left(\frac{\sigma^{A,B}}{2\sigma^{f,v}}\right) \tag{5.1}$$

Where $\sigma^{A,B}$ is the interfacial energy between the phase separating components A and B, while $\sigma^{f,v}$ is the surface energy of the film surface with respect to the vapor phase.

$$\sigma^{A,B} = 2N_v\lambda[K_BT]^{1/2}\int_{\emptyset_A}^{\emptyset_B}\left(f(\emptyset)\right)^{1/2}\mathrm{d}\emptyset \tag{5.2}$$

Where N_v denotes the number of molecules per unit volume, and λ is the interaction distance, which is related to the intermolecular distance and is assumed to be a constant for the alloy. K_B is the Boltzmann constant and T is the absolute temperature. $\emptyset$ is the composition field which varies in value from $\emptyset_A$ within the A-rich phase to $\emptyset_B$ within the B-rich phase.

A model using a three-dimensional domain with a maximum of 150x150x150 grid points is constructed. We assign a characteristic length-scale, L* equal to 1:1 nm, which is calculated based on observed interface widths and morphological phase-separated domains in vapor deposited Cu based immiscible alloys with Ta and Mo [94][95].

An initial condition reflecting either a characteristic perturbed seed or of Langevin noise is given to the system. The top half of the simulation space is assigned as the vapor phase, thereby allowing for a 50/50 split in the space by volume. To simulate deposition, a layer of Langevin noise is added every few time steps, n$\triangle$t which leads to a temporal increase in the film's thickness. The noisy layer is added at the juncture of the interface between the vapor and the film, at $\emptyset_v = 0.5$. To compensate for loss in relative volume of the vapor phase, a layer of thickness $\triangle$x of vapor phase is also added to the top of the simulation space. A schematic of the deposition process is shown in Figure 5. 4 and the simulated structure of hillocks under different contact angle and designated location of seeds are shown as from Figure 5. 6 to Figure 5. 9.

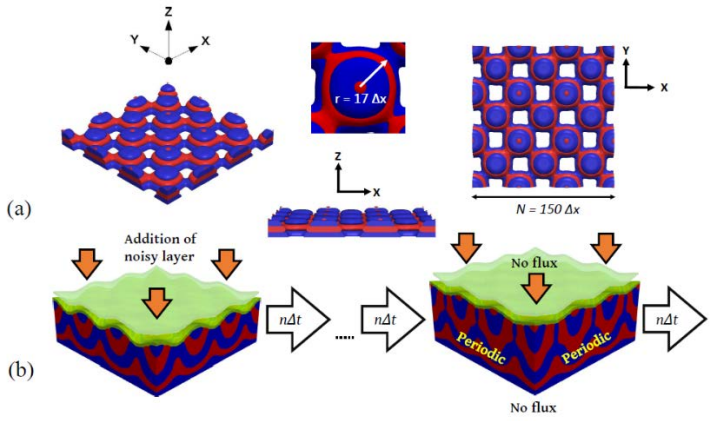

Figure 5. 4 Schematic of Simulated Vapor Deposition of Phase-Separating Alloy Film With Steep Protuberances. (a) Protuberances Are Spherical With r = 17Δx. (b) Boundary Conditions Assumed Are Periodic Along x and y Axes, and No-Flux Along the Deposition Axis.

5.3 The Results and Conclusions of Simulation and Experiment.

The simulations are execute by 2 parts which are organized arranged seeks and random seed with different contact angle at 0°, 47° and 63°. The simulation results of organized arranged seed are present from Figure 5. 6 to Figure 5. 8 and the simulation outcomes of random seed is illustrated as Figure 5. 9. The simulation results show that when the contact angle between 2 phases is large, the shorter hillocks will be generated because the stronger interfacial energy exists. From the simulated images, we also found that the repeated patterns are occurred. To extract this hidden information, P_n functions can be utilized to show this phenomenon for organized arranged seed simulation.

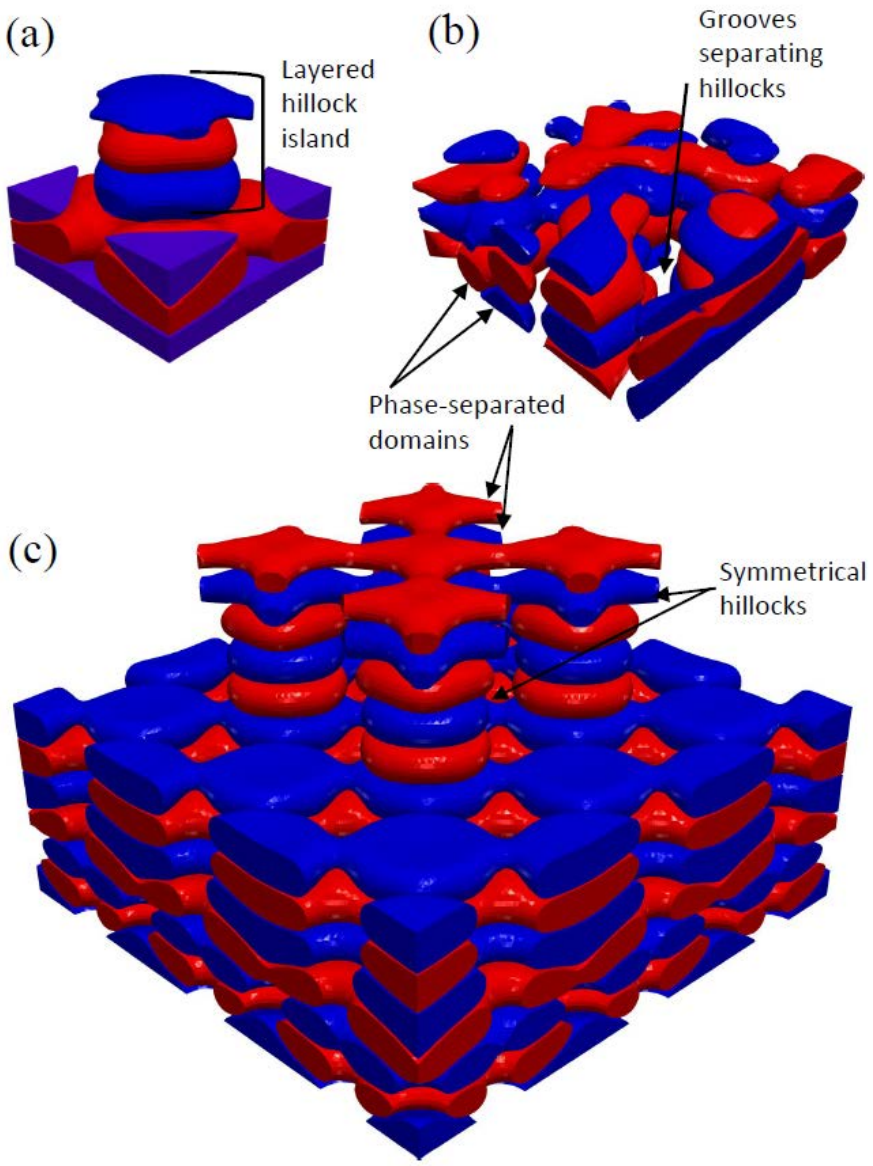

Figure 5. 5 Distinct Hillock Nanostructures that Evolve During Vapor Deposition of Phase Separating Alloy Film Depending on the Seed Morphology. (a) A Representative Volume of the Film Showing A Disconnected Hillock When Deposition Simulations Are Initialized from a Perturbed Seed That Comprises of Vertical Concentration Modulations. (b) Connected Hillocks That form When Deposition Simulations Are Initialized from a Random Seed, and (c) Segmented Film with Symmetrical Hillocks That form at Narrow Contact Angles When the Seed morphology is same as (a).

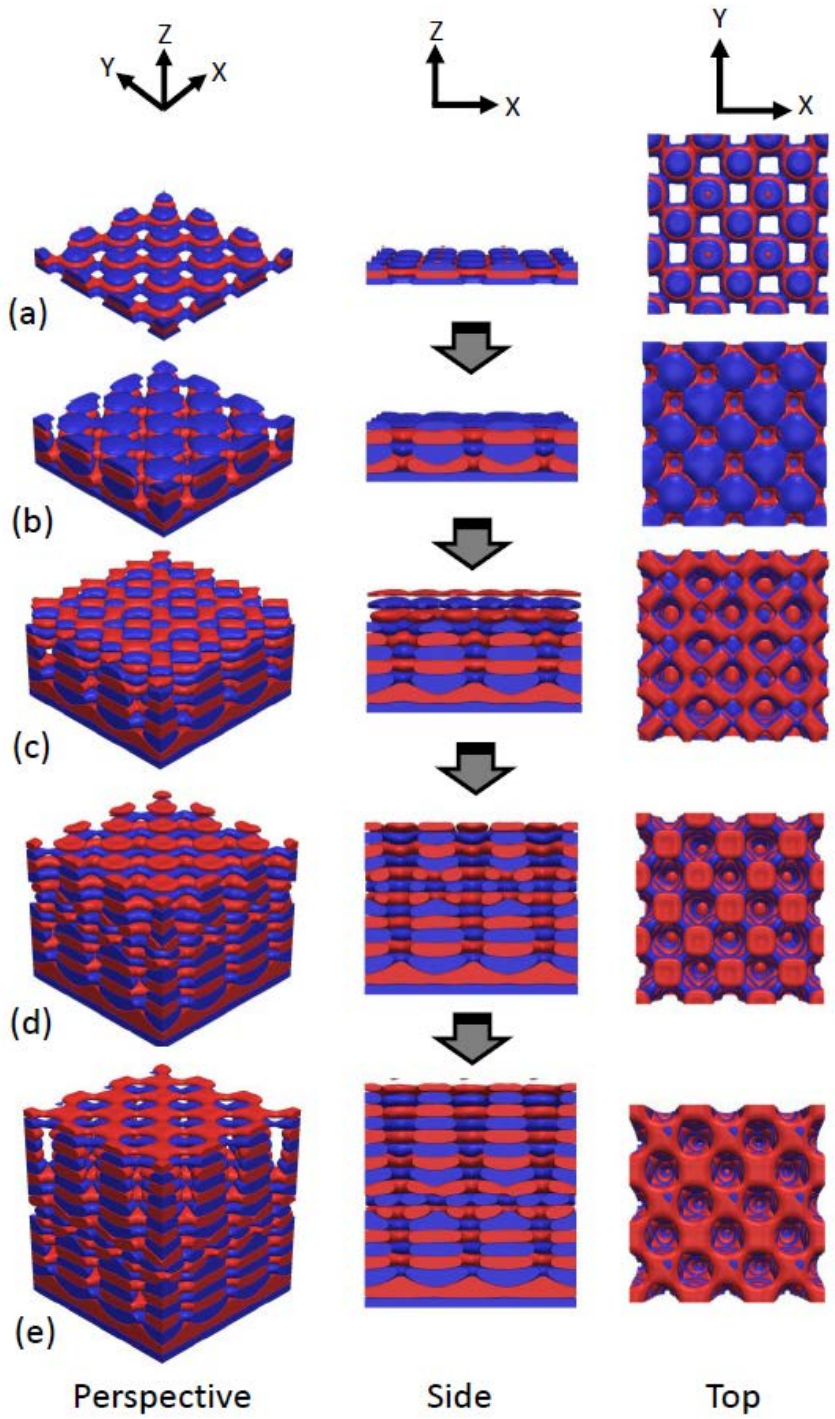

Figure 5. 6 Simulated Vapor Deposition from An Initial Hillock Seed Condition for Protuberation Radius of 17 Δx and a Preset Contact-Angle ≈ 0◦ at Different Time-Steps (a) t=12, (b) t=612, (c) t=1212, (d) t=1812, and (e) t=2412.

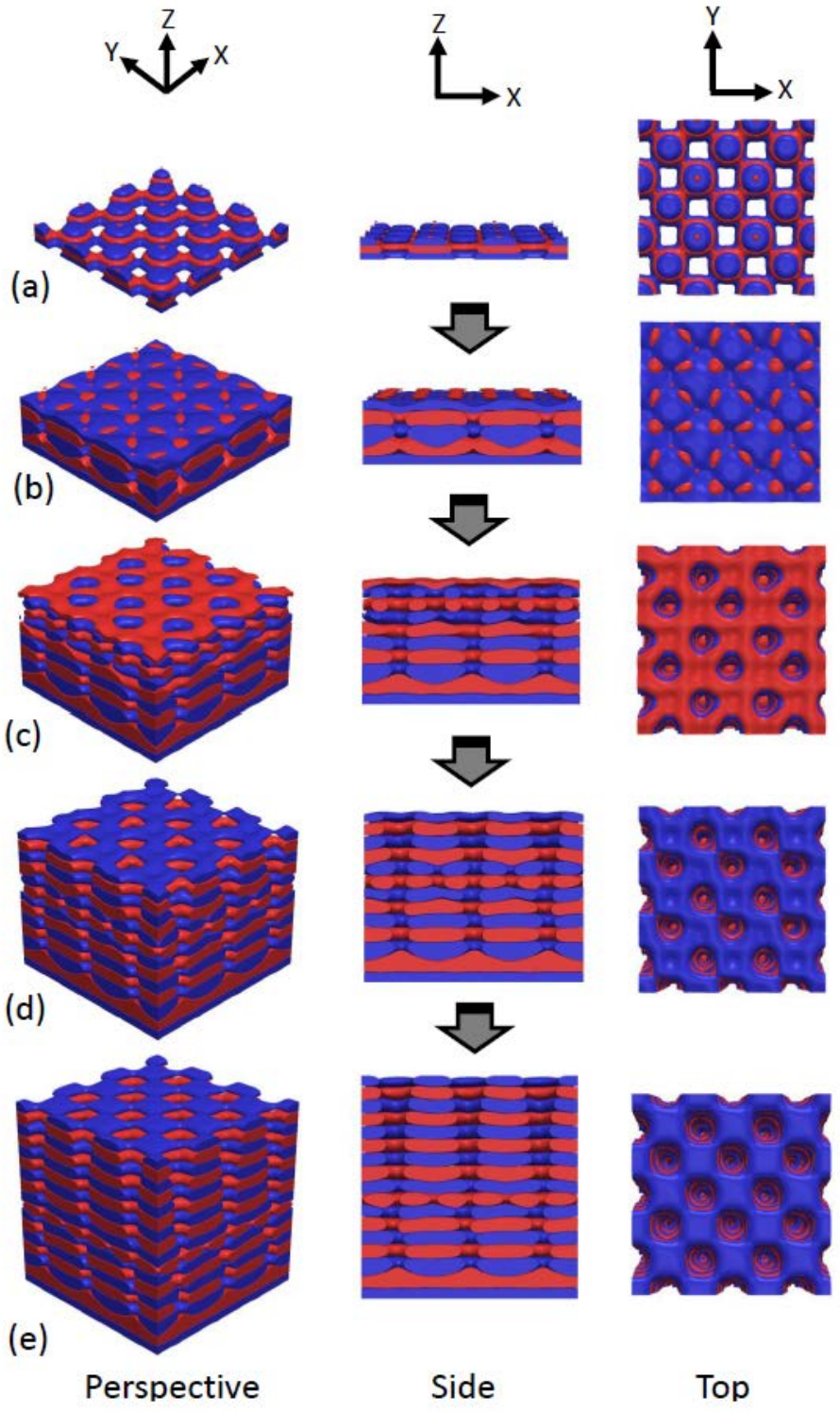

Figure 5. 7 Simulated Vapor Deposition from an Initial Hillock Seed Condition for Protuberation Radius of 17 Δx and a Preset Contact Angle ≈ 47◦ at Different Time-Steps (a) t=12, (b) t=612, (c) t=1212, (d) t=1812, and (e) t=2412.

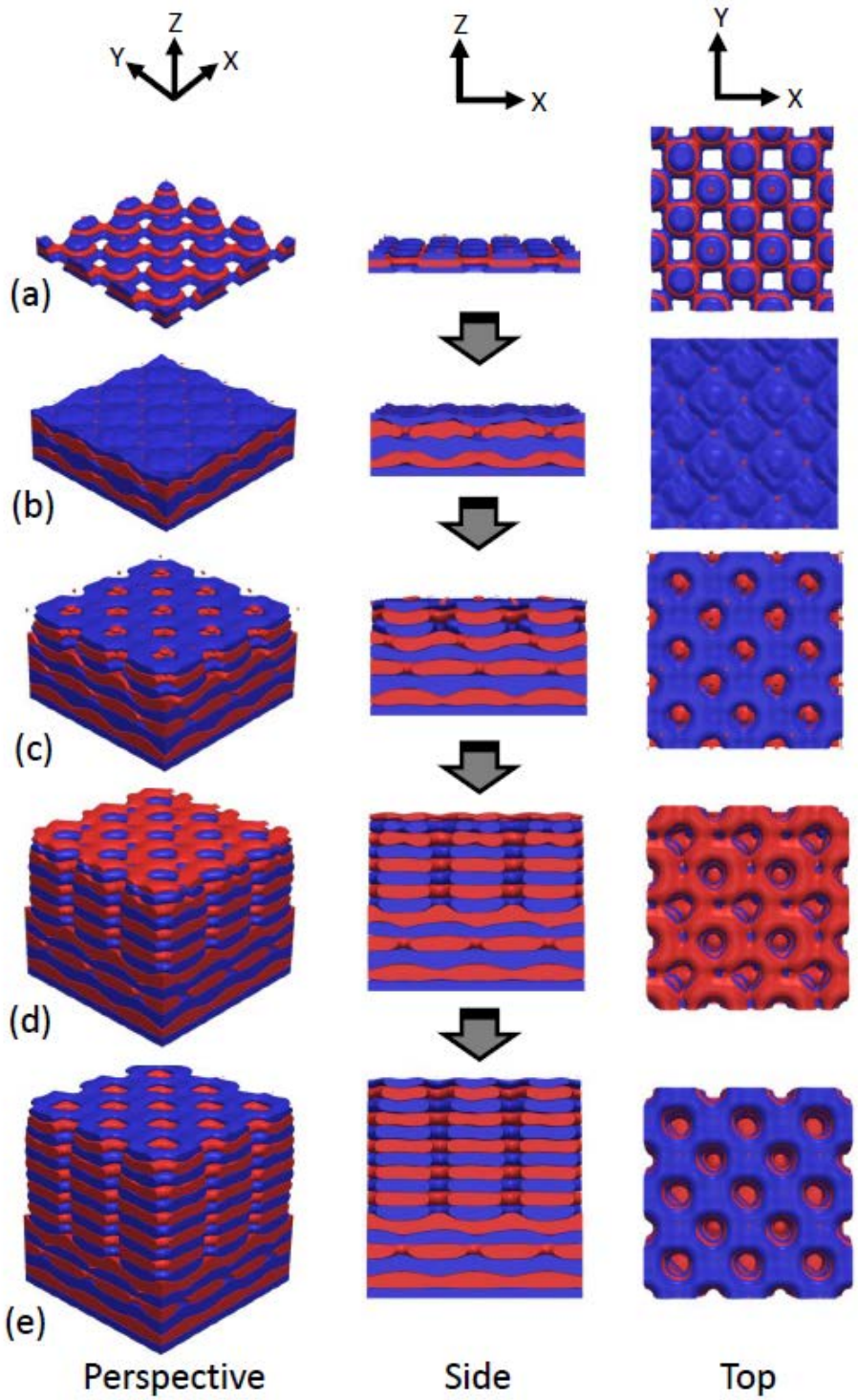

Figure 5. 8 Simulated Vapor Deposition from An Initial Hillock Seed Condition for Protuberating Radius of 17 Δx and a Preset Contact Aangle ≈ 63◦ at Different Time-Steps (a) t=12, (b) t=612, (c) t=1212, (d) t=1812, and (e) t=2412.

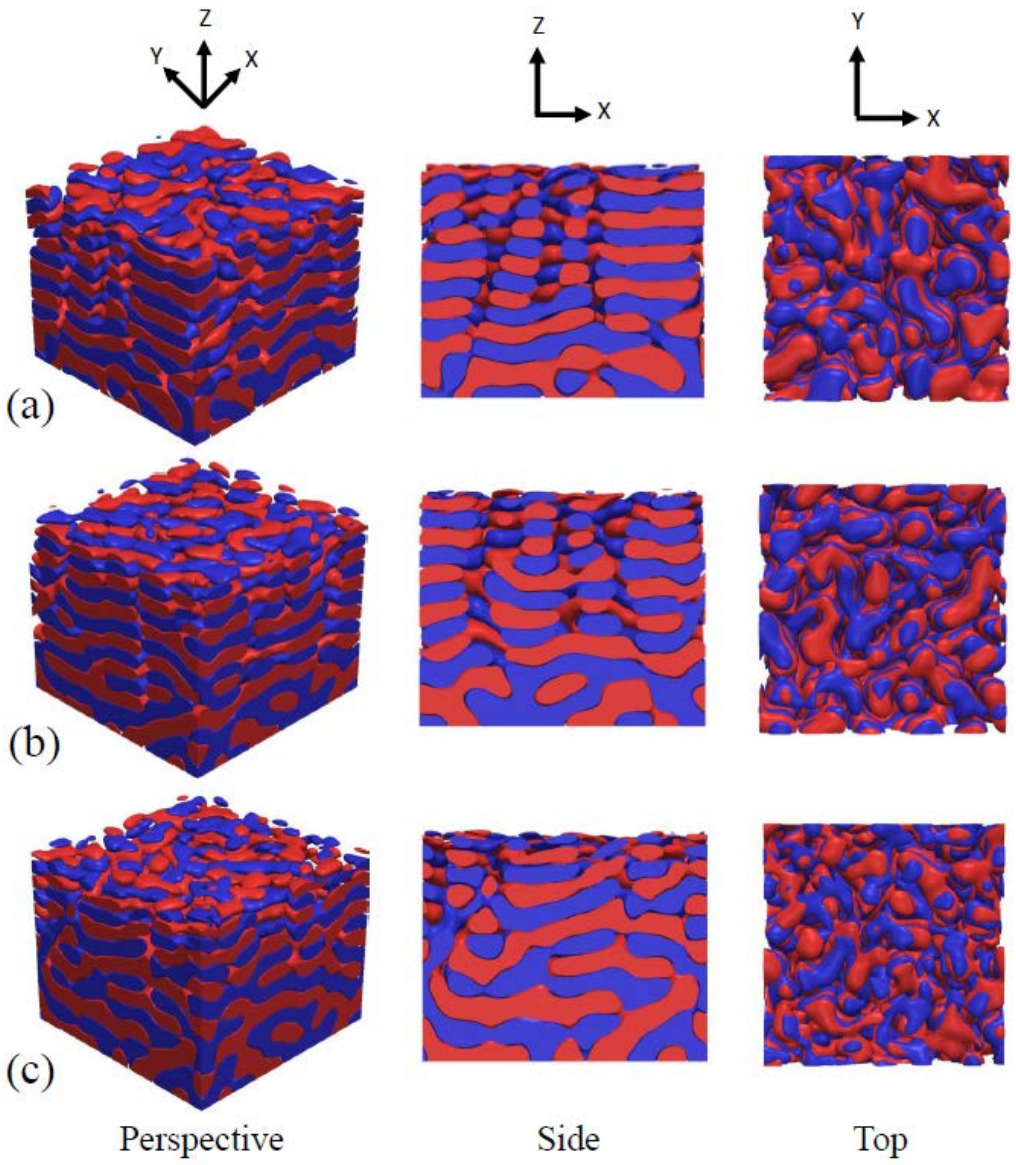

Figure 5. 9 Simulated Vapor Deposition from a Random Seed Condition at Contact Angles (a)≈0◦, (b)θ≈47◦, and (c) θ≈63◦

5.4 Using P_n Functions to Couple Related Simulations and Experiments.

In this section, I will directly use P_n functions to analyze the evolving images of professor Ankit's simulation.

Initially, I employ the polytope functions P_2 and P_4 to quantify microstructural evolution of the deposited thin films. In particular, for a fixed contact angle θ, I first select three representative snapshots of the top surface of the deposited film during its growth and segment the phase of interest. Without loss of generality, we focus on the blue phase in our analysis. Since the blue and red phases are complementary to each other, analyzing one of the phases is sufficient to provide statistical quantification of the pattern.

Figure 5. 10 (a), (b) and (c) shows the computed functions from the simulated thin film samples of organized arranged seeds for three contact angles $\theta \approx 0^\circ$, $\theta \approx 47^\circ$ and $\theta \approx 63^\circ$, respectively. For different contact angles, the phase morphology exhibits distinct evolution pathways. Specifically, for $\theta \approx 0^\circ$ where the morphology of blue phase varies from an interconnected network to compact clusters to connected complex topology. For the other two angles, regular patterns of holes develops as the deposition proceeds, which correspond to the hillocks.

Nonetheless, the P_n functions reveal universal hidden correlations across all angles and all times. In particular, the peaks in P_2 and P_4 respectively indicate characteristic length-scales associated with strong two-point correlations and 4-point correlations. It can be clearly seen that these length scales all coincide with one another, regardless of the underlying geometry and topology of the phase microstructure. In addition, the strong peaks in P_4 at $r \approx 30$ nm and 60 nm indicates strong 4-fold symmetry, which is inherited from the initial seeds and preserved during the film growth process.

For the random seeds part, the morphology of the deposited film is also quantified by using the 2-point function P_2 (see Figure 5. 11). Since the patterns resulted from the random seeds do not possess long-range correlations, the associated P_2 functions possess the well-known damped oscillation form [58][60], with the length scale associated with the first local minimum and maximum corresponding to the average width of the ligaments and the inter-ligament spacing. It can be seen that increasing the contact angle leads to decrease of both ligament width and spacing at specific time, as manifested as the shifting of the first local minimum and maximum to larger distances.

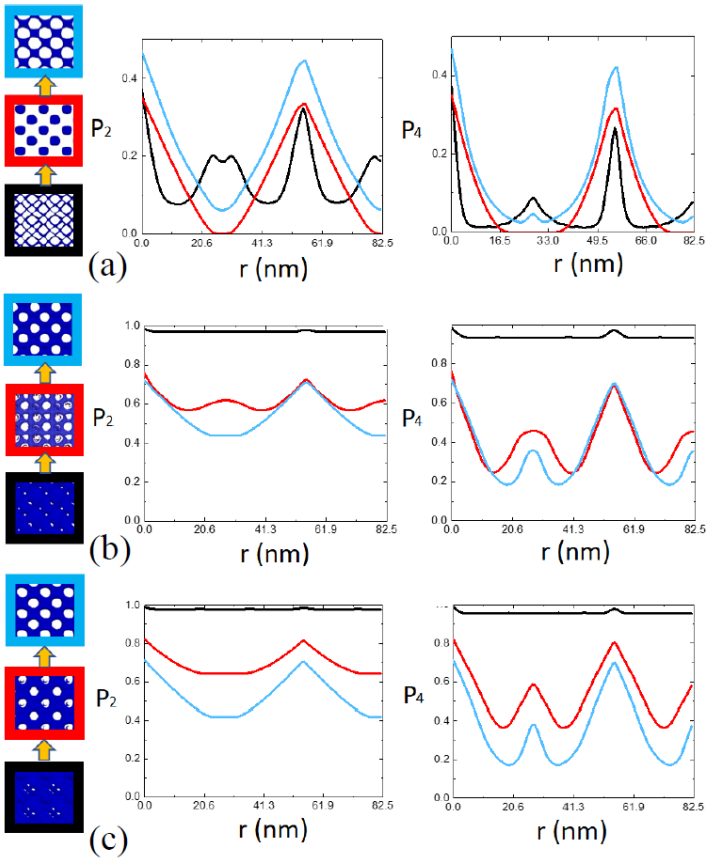

Figure 5. 10 Quantification of Evolving Patterns of the Deposited Thin Film via Polytope Functions. The Functions Associated With Segmented Blue Phase Morphologies Are Computed from the Simulated Thin Film Samples for Three Contact Angles, (a) θ=0◦, (b) θ=47◦ and (c) θ=63◦. The Analyses Reveal Universal Hidden Correlations Across All Angles and All Times, Manifested as the Coinciding Length-Scales Associated with Peaks in the Functions.

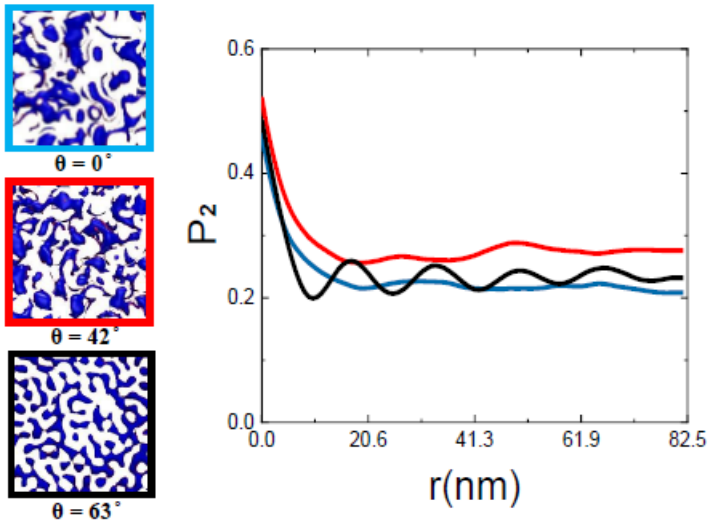

Figure 5. 11 Quantification of the Morphology of the Deposited Films Resulted from Random Seeds Using the 2-Point Function P_2.

5.5 Using Reduced-Dimension Methods to Efficiently Quantify 4D Evolution.

Form the previous paragraph, we can certainly detect that the P_n functions of evolving images of each time internal can be calculated independently under external stimuli. In the Figure 5. 10, nine evolving images for P_2 and P_4 analysis can cause 18 independently curves for different contact angle. The quantification ability of P_n function is undeniable. However, if the evolution duration is prolonged or the interval between 2 images is shorten, the numerous increased images will cause numerous numbers of P_n functions' curves which will be so chaotic and complex to be observed for the selected P_n functions. Or to put it another way, if one want to analyze P_2, P_3, P_4, P_6, and P_8 for 150 evolving images, the final result which contains 750 curves will concurrently be revealed in the same coordinate. Not to mention if someone want to investigate the huger model.

Moreover, all the independent P_n functions curves can only present temporal microstructure quantification at certain time. By observing the whole P_n functions result, we

only can understand the tendency of evolving microstructure for each interval. If we only use P_n functions to analyze hillocks of films, we can only obtain the discontinuous results and these results can only provide limit insight of the film. That is why from Figure 5. 10(a), we only can detect that the morphology is transferred from an interconnected network to compact clusters to connected complex topology according the width of peak and the oscillation tendency of relating P_n functions curves. In other words, the results of P_n functions curve are non-generic and non-feature dependent.

Obviously, I don't only need enough database but also a systemic and organized method to compare and contrast the consecutive processes of 4D evolution of our target object without losing its original microstructure generality.

5.5.1 The Concept of Omega Metrix

Under the circumstance we have discussed before, in order to continuously extract the characteristic physics and mechanisms from 4D evolution, a more simplified and smart method is needed to be utilized for processing-structure-property mapping with a basis of reduced-dimension microstructure representation. For 4D evolution analysis, I will use Omega Metrix which is a purely concise, concurrently visualized, physically interpretable reduced-dimension representation for microstructure evolution to overcome all the hindrances of 4D analysis.

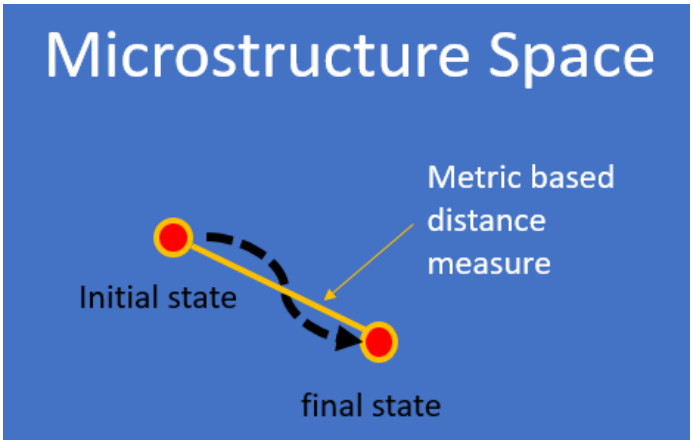

Figure 5. 12 The Concept of Omega Metric

But, what on earth is Omega Metric? The basis of Omega Metric is an effective distance from different microstructures compared to the referenced image by using the results of P_n functions, and thus, provide a measure for the entire structure of the high-dimensional microstructure space (shown as Figure 5. 12). From the value of Omega Metric, we can totally differentiate the difference between images captured from different time and if these analyzed images are matched or not to the referenced one. Besides, Omega Metric can decompose different symmetry features into canonical polytope symmetry groups, allowing one to detect potentially distinct convergence and dynamics of evolution of different symmetry groups underlying the microstructure. Since Omega Metric is inherited from the P_n functions which are continuous and differentiable w.r.t. microstructures, that is why I believe that Omega Metric can offer virtual microstructures for microstructural evolution to allow AI-based (gradient-based) evolution prediction, 4D material microstructure design and optimization.

5.5.2 The Formula of Omega Metrix

The formula of Omega Metric can be written as

$$\Omega n(t) = \Sigma r \left| P_n (r; t) - P_n (r; t=0) \right| \quad (5.3)$$

Where the t is represent arbitrary time relative to the reference image, r is the distance between vertices of each 2D regular polytope, t=0 is the initial time for the referenced image. So, the Omega Metric Ωn(t) is the summation of the absolute value of the distance/difference of P_n Functions between analyzed and referenced image under different length scale for different time. Developed Omega Metrix can integrate and immerge the same value n of P_n functions into a continuous curves. In such situation, if one want to analyze P_2, P_3, P_4, P_6, and P_8 for 150 evolving images, the final result of Omega Metric with 5 curves will concurrently be revealed in the same coordinate. Furthermore, since every Omega Metric contains continuous status of each evolving image, the curves can contain all the original mechanism and structural information of evolution. In the next section, I will use the Omega Metric to analyze the 4D results of vapor-deposition of phase-separating alloy film.

5.5.3 The Analysis Results of Omega Metric of Vapor-Deposition of Phase-Separating Alloy Film.

When I use the whole film simulation results of blue phase at contact angle=0 to calculate its evolution Omega Metric from n=1, 2, 3, 4, 6 and 8, the results of Omega Metric are easily shown that there are so many peaks and oscillation occur in Figure 5. 13. Since the definition of the Omega Metric is the summation value of absolute distance from the reference image, we can easily realize that the larger value of Omega value means the more different image compared with reference configuration will be. To proof this idea, I compare the image of reference point which is the start point at the origin when t=0 and the maximum peak point in Figure 5. 13. Since the image of reference and the maximum are totally different, this

situation induce me to explore the relation between images for every limit point to get more detail information. All the comparison are shown as Figure 5. 14.

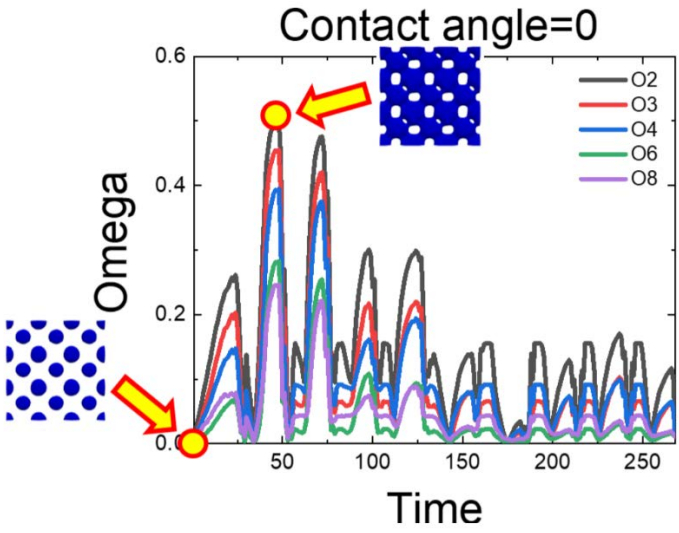

Figure 5. 13 The Results Shown the Evolution for Theta= 0 case. It Turns Out That the Omega n for Different n Yield Consistent Measure of the Microstructural Space.

I enlarge the scope of curve of Figure 5. 13 from t=8 to 80 to have more detailed data points to investigate the image of each limit point. From Figure 5. 14, we can detect that every lower points near the Omega value=0 have similar microstructure with reference's one. On the country, the peaks' microstructure are totally opposite to the configuration of reference. From this circumstance, I can understand the trend of Omega function is thoroughly depends on its reference's microstructure. If the curves of Omega Metric have decreasing tendency with x coordinate (time) shown as Figure 5. 15, the whole evolution system shall has similar microstructure with the reference's configuration vice versa. Since the curves of Figure 5. 15 have decreasing tendency, so the probability of hillock growth is pretty high because the all peak points are not far always from the reference point and all the images' microstructure shall be similar. In the Figure 5. 15, since the reference image we choose has more vacant space, it reveals that the whole system must has more opportunity to have vacant space which is also known as hillock in the film. In order to research relationship of hillock growth between

different angles, I also calculate the results of Omega Metric for these 3 different angles in Figure 5. 16. The decreasing tendency is chartered for all the angle but the whole result of angle=0 has the lowest orange tendency curve. In other words, the smaller contact angle, the more hillock will be produce.

The conclusion of Omega Metric of Figure 5. 16 can also reflect the conclusion of film's simulation "when the contact angle between 2 phases is large, the shorter hillocks will be generated because the stronger interfacial energy exists".

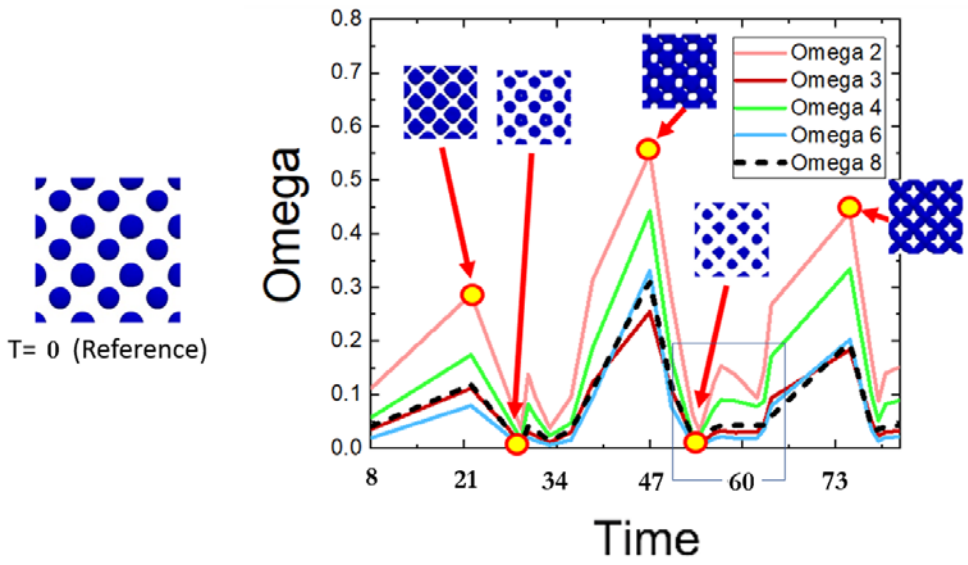

Figure 5. 14 The Image of Every Limit point at Domain from Time=8 to Time=80.

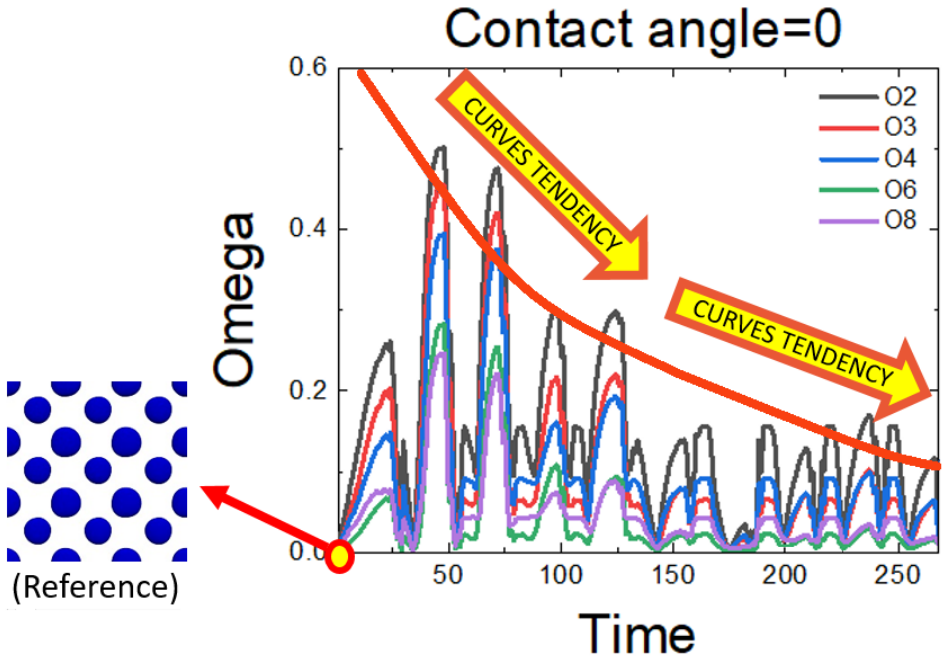

Figure 5. 15 The Tendency of Curves.

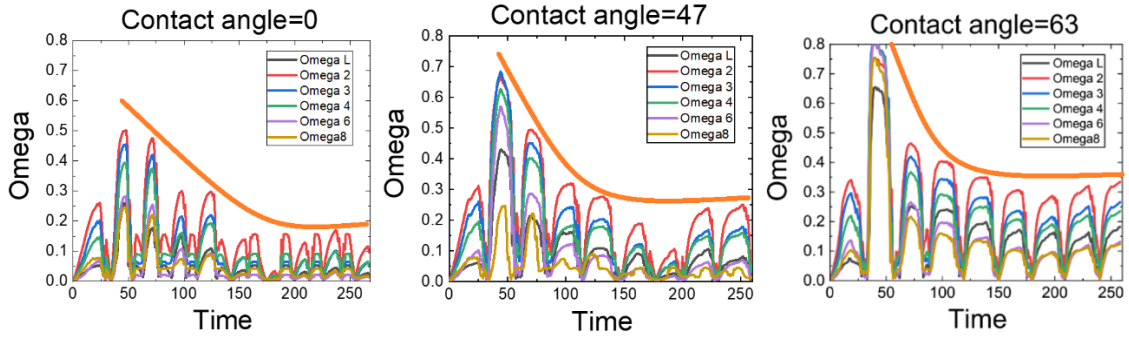

Figure 5. 16 The Decreasing Tendency of Curves of Film at Different Angles.

From the last paragraph, we realize that the chosen reference image and the tendency of its Omega Metric curve play an important role for evolution quantification. In order to investigate the relation between reference image and the tendency of its Omega Metric curve, I will try to change the reference image to execute Omega Metric calculation to extract the characteristics from the evolution process directly and see if its final results can provide us more information or not. Take the results of vapor-decomposition film for example, I prefer choose the connected microstructure opposite to the reference image of Figure 5. 13 as the

reference one because the connectivity of configuration severely affect the yield rate of the chip.

The whole results of curves of Omega Metric shown in Figure 5. 17 which use connected image as reference image also correctly corresponds to Figure 5. 16's result which set the sparse phase image as the reference configuration. In Figure 5. 17, you can see the tendency of Omega Metric is increasing with respect to x coordinate. In other words, it means that the whole system at contact angle=0 rarely contains the connected microstructure.

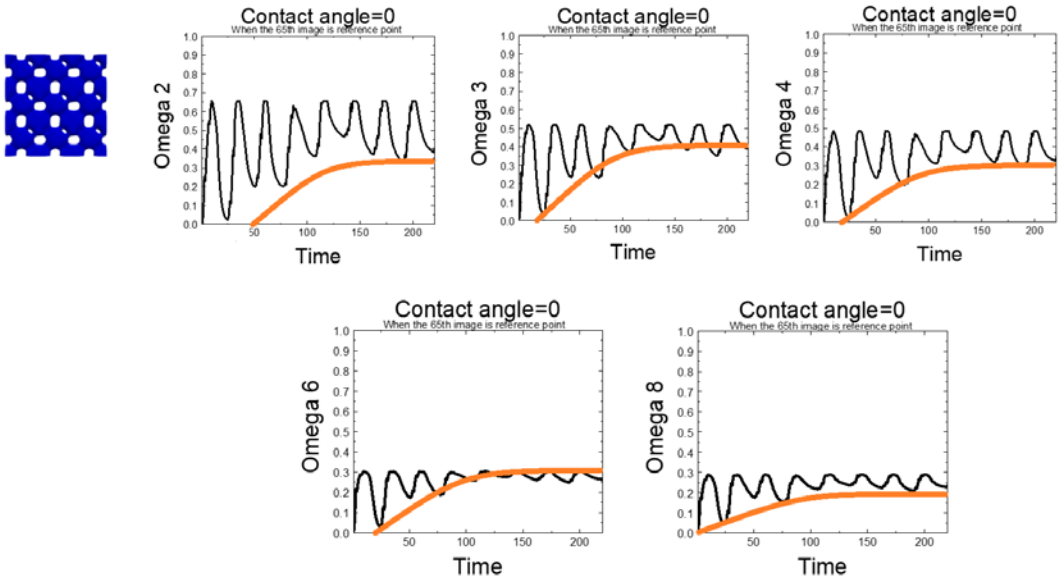

Figure 5. 17 The Curve Tendency Results of Omega Metric Which Use Connected Image as the Reference Image

From the process of changing the reference image, its results offer a brand new idea and concept about that changing the reference image can help and provide engineers or designers a prediction to select the most suitable contact angle to design the chip with the least hillocks by reference image's related curve tendency of Omega Metric. Maybe someone shall ask that how can we get the optimal design by using Omega Metric? The suggested procedure

is that one can choose the required or wanted pattern as the reference image to substitute the P_n (r; t=0) term in Omega Metric formula and use all the calculated P_n functions data from different angle to distinguish which angle's Omega Metric curve has decreasing tendency and the angle with the lowest tendency line shall be the best angle for vapor-deposition process.

For the chip design made from other different material, one can use professor's contact angle formula to get the evolving images and their P_n functions at arbitrary angle. After that one select the designed pattern as reference image then repeat the Omega Metric procedure, one can get the best contact angle for optimal design.

5.5.3 Differential Omega Matric.

Actually, the processes of evolution of vapor-deposition film is a kind of diffusion-controlled system which contains different drug delivery systems caused by the energy of assorted interface and phases. Besides, it predominantly controls the diffusion of vapor-deposition to let the phases seductively diffuse from one place to other place. That is why the vapor-deposition alloy film which is formed by diffusion-controlled system can be classified as a product of the heterogeneous material.

If the deposition rate of vapor-deposition film is really high, its microstructure will also change itself dramatically. Under this circumstance, the curve of Omega Metric may lost some characteristic feature of microstructure and cannot easily to reveal more detail information of evolution. In order to prevent this issue to be occurred, A Differential Omega Metric can be used to exam this exceptional case. The Differential Omega Metric is defined as

$$D\Omega n(t) = \Sigma r \left| P_n (r; t) - P_n (r; t=t-1) \right| \qquad (5.4)$$

According to the formula of Differential Omega Metric (DOM), we can obviously understand the difference between the Omega Metric and DOM is that the reference point of

DOM is its previous stage' image rather than the fixed reference point which used by the Omega Metric formula. The results of DOM will be the absolute distance between every time interval. The peak of Differential Omega Metric curves means the changing rate of phase/microstructure/volume fraction at the indexed interval. By using the DOM, we can decide that if the evolving system is converged to the steady state or not by observing the curve of DOM. If the results of DOM's curve only disclose minor oscillation or repeated pattern, the evolving system is under the steady state or periodic pattern and all the outcomes and optimal design of Omega Metric are valid and convinced. On the other hand, one need to adjust the time interval to put more images into Omega function to obtain more optimal curve which can contain more microstructure data. The repeated pattern of DOM is shown in Figure 5. 18.

As I have mentioned before, the vapor-deposition film is only a case of diffusion controlled system. Actually, Omega Metric and DOM have significantly potential ability to be applied to other diffusion controlled fields for quantification or optimal design purposes.

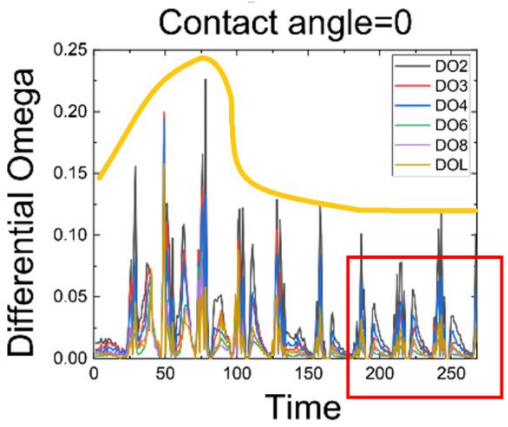

Figure 5. 18 The Tendency of Curves of DOM for Vapor-Deposition Film at Angle=0.

CHAPTER 6

DISCUSSION AND FUTURE WORK

After I introduce and review the result of P_n functions' quantification which is the subset of S_n functions, P_n functions' reconstruction which adopts YT reconstruction procedure and Omega Metric/Differential Omega Metric which can be used for analyzing material's evolution more efficiently, we can easily understand that these methods are valid, concise, expressive, universal and interpretable for analyzing heterogeneous materials. Although these quantification methods are useful, there are some important factors needed to be considered.

The first factor is that when I use P_n functions rather than S_n functions to save calculation time and facilitate quantification process for seriously irregular shape of particle, it may cause some extended error of quantification. Though the occurred error is existing because of the geometric shape of particle, the computed results with this allowable error can still help us to analyze the microstructure of heterogeneous materials by checking the P_n vs r curve shown in the chapter 3. Actually, according to the computational results and our observation in chapter 3, P_n functions which is the subset of the S_n functions do can provide a valid, and reliable algorism of quantification.

The second factor is that when I reconstruct the model from its obtained P_n functions, how many P_n functions should I put into YT reconstruction procedure to reconstruct the simulated results. According to the conclusion and observation of chapter 4, more involved data set of P_n functions doesn't means the better simulation results we will get.

In chapter 4, I have examined a wide spectrum of different material with distinct geometrical and topological features and found that incorporating more data set into the reconstruction calculation also significantly increases the complexity and roughness of P_n

functions of the associated energy landscape for the underlying stochastic optimization. Finally, it makes the result of simulation is difficult to be converged numerically. It indicates that for certain complex systems, successively incorporating higher order correlation functions in a linear fashion might not be the best strategy to be executed, as one can significantly increase the computational cost without incorporating too much useful additional morphological information. In the future work for this concern, one can develop an alternative approach to decide how many sensitive and necessary P_n functions should be considered to be put into the YT reconstruction procedure to compute the more accurate simulation result.

The third factor is that I only use 2D model to quantify and reconstruct the cross-section images in this dissertation to prove that the P_n functions and YT reconstruction procedure are practicable. However, actually the reconstruction for 2D and 3D cases for some circumstances should need to be more deliberated because 2D reconstruction only includes the connectivity of 2 axis. Under some situation, the relationship of connectivity of one plan cannot thoroughly describe the features of the structure. Although one can X-ray the object of target and get finite 2D images to quantify the materials, the combined results of the total 2D reconstruction may has error to the real 3D model. In the future work, the best way is to X-ray the target and restore the location of all the interested phases as 3D digital matrix and create regular 3D templates to compute the related 3D P_n functions which will possesses the relationship of special connectivity between each interested phases. Since 3D P_n functions has more insight about geometric and connected relationship than 2D P_n functions, it can be predictable and reasonable that 3D reconstruction will has more accurate reconstruction results.

The final factor is that if we can obtain the 3D P_n functions results from interesting object's 3D phase matrix, theoretically Omega Metric/Differential Omega Metric can reveal

more realistic result. Since this field is still unexplored, it can be further be researched and discussed.

Although I just present several theoretical and real example of P_n function and its applied functions such as P_n function's reconstruction and Omega Metric/Differential Omega Metric, all the quantitation methods can be utilized in medical, industrial, educational, military, technology field etc. For the future work, one also can execute these methods in different field for more sophisticated cases which cannot easily be distinguished by our naked eyes or instruments.

REFERENCES

[1] Salvatore Torquato. Random Heterogeneous Materials: Microstructure and Macroscopic Properties. New York: Springer, 2002. Print.

[2] M. Sahimi. *Heterogeneous Materials I: Linear Transport and Optical Properties*. New York: Springer, 2003. Print.

[3] K. Thornton, H.F. Poulsen. "Three-Dimensional Materials Science: An Intersection of Three-Dimensional Reconstructions and Simulations." *MRS Bull 33* (2008): 587-595. Print.

[4] L. Babout, E. Maire, J.Y. Buffière and R. Fougères. "Characterization by X-ray computed tomography of decohesion, porosity growth and coalescence in model metal matrix composites." *Acta Materialia* 49 (2001): 2055-2063. Print.

[5] A. Weck, D.S. Wilkinson, E. Maire and H. Toda, "Visualization by X-ray tomography of void growth and coalescence leading to fracture in model materials." *Acta Materialia* 56 (2008): 2919-2928. Print.

[6] H. Toda, S. Yamamoto, M. Kobayashi, K. Uesugi and H. Zhang, "Direct measurement procedure for three-dimensional local crack driving force using synchrotron X-ray microtomography." *Acta Materialia* 56 (2008): 6027-6039. Print.

[7] J.J. Williams, Z. Flom, A.A. Amell, N. Chawla, X. Xiao, F. De Carlo, "Damage evolution in SiC particle reinforced Al alloy matrix composites by X-ray synchrotron tomography. " *Acta Materialia* 58 (2010): 6194-6205. Print.

[8] J.J. Williams, K.E. Yazzie, N.C. Phillips, N. Chawla, X. Xiao, F. De Carlo, N. Iyyer and M. Kittur, "On the correlation between fatigue striation spacing and crack growth rate: a three-dimensional (3-D) X-ray synchrotron tomography study." *Metallurgical and Materials Transactions* A 42 (2011): 3845-3848. Print.

[9] Williams, J., K. Yazzie, E. Padilla, N. Chawla, X. Xiao, and F. De Carlo, "Understanding fatigue crack growth in aluminum alloys by in situ X-ray synchrotron tomography." *International Journal of Fatigue* 57 (2013): 79-85. Print.

[10] Singh, S., J. Williams, M. Lin, X. Xiao, F. De Carlo, and N. Chawla, "In situ investigation of high humidity stress corrosion cracking of 7075 aluminum alloy by

three-dimensional (3D) X-ray synchrotron tomography." *Materials Research Letters* 4 (2014): 217-220. Print.

[11] McDowell, D., V. Sundaraghavan, and J.A. Scott, "Advanced Computation and Data in Materials and Manufacturing: Core Knowledge Gaps and Opportunities." *TMS Technical Report* (2018) Print.

[12] Kalidindi, S.R., *Hierarchical Materials Informatics: Novel Analytics for Materials Data.* Elsevier (2015) Print.

[13] Kalidindi, S.R., J.A. Gomberg, Z.T. Trautt, and C.A. Becker, "Application of data science tools to quantify and distinguish between structures and models in molecular dynamics datasets." *Nanotechnology* 34 (2015):344006. Print.

[14] Steinmetz, P., Y.C. Yabansu, J. Hötzer, M. Jainta, B. Nestler, and S.R. Kalidindi, "Analytics for microstructure datasets produced by phase-field simulations." *Acta Materialia* 103 (2016): 192-203. Print.

[15] Xu, H., Y. Li, C. Brinson, and W. Chen, "A Descriptor-Based Design Methodology for Developing Heterogeneous Microstructural Materials System." *Journal of Mechanical Design* 5 (2014): 051007. Print.

[16] Fullwood, D.T., S.R. Niezgoda, B.L. Adams, and S.R. Kalidindi, "Microstructure sensitive design for performance optimization." *Progress in Materials Science* 6 (2010): 477-562. Print.

[17] Jain, A., J.R. Errington, and T.M. Truskett, "Dimensionality and design of isotropic interactions that stabilize honeycomb, square, simple cubic, and diamond lattices." *Physical Review X* 3 (2014): 031049. Print.

[18] Sharma, V., C. Wang, R.G. Lorenzini, R. Ma, Q. Zhu, D.W. Sinkovits, G. Pilania, A.R. Oganov, S. Kumar, and G.A. Sotzing, "Rational design of all organic polymer dielectrics." *Nature communications* 5 (2014): 4845. Print.

[19] Baldwin, A.F., T.D. Huan, R. Ma, A. Mannodi-Kanakkithodi, M. Tefferi, N. Katz, Y. Cao, R. Ramprasad, and G.A. Sotzing, "Rational Design of Organotin Polyesters." *Macromolecules* 8 (2015): 2422-2428. Print.

[20] Gupta, A., A. Cecen, S. Goyal, A.K. Singh, and S.R. Kalidindi, "Structure–property linkages using a data science approach: Application to a non-metallic inclusion/steel composite system." *Acta Materialia* 91 (2015): 239-254. Print.

[21] Kaczmarowski, A., S. Yang, I. Szlufarska, and D. Morgan, "Genetic algorithm optimization of defect clusters in crystalline materials." *Computational Materials Science* 98 (2015): 234-244. Print.

[22] Xu, H., R. Liu, A. Choudhary, and W. Chen, "A Machine Learning-Based Design Representation Method for Designing Heterogeneous Microstructures." *Journal of Mechanical Design* 5 (2015): 051403. Print.

[23] Kirklin, S., J.E. Saal, V.I. Hegde, and C. Wolverton, "High-throughput computational search for strengthening precipitates in alloys." *Acta Materialia* 102 (2016): 125-135. Print.

[24] Torquato, S. and G. Stell, Microstructure of two-phase random media. I. "The n-point probability functions." *The Journal of Chemical Physics* 4 (1982): 2071-2077. Print.

[25] Torquato, S. and G. Stell, "Microstructure of two-phase random media. III. The n-point matrix probability functions for fully penetrable spheres." *The Journal of chemical physics* 79 (1983): 1505-1510. Print.

[26] Torquato, S. and G. Stell, "Microstructure of two-phase random media. V. The n-point matrix probability functions for impenetrable spheres." *The Journal of chemical physics* 82 (1985): 980-987. Print.

[27] Jiao, Y., E. Padilla, and N. Chawla, "Modeling and predicting microstructure evolution in lead/tin alloy via correlation functions and stochastic material reconstruction." *Acta Materialia* 61 (2013): 3370-3377. Print.

[28] Guo, E.-Y., N. Chawla, T. Jing, S. Torquato, and Y. Jiao, "Accurate modeling and reconstruction of three-dimensional percolating filamentary microstructures from two-dimensional micrographs via dilation-erosion method." *Materials Characterization* 89 (2014): 33-42. Print.

[29] Jiao, Y. and N. Chawla, "Three dimensional modeling of complex heterogeneous materials via statistical microstructural descriptors." *Integrating Materials and Manufacturing Innovation* 3 (2014): 1-19. Print.

[30] Jiao, Y. and N. Chawla, "Modeling and characterizing anisotropic inclusion orientation in heterogeneous material via directional cluster functions and stochastic microstructure reconstruction." *Journal of Applied Physics* 115 (2014): 093511. Print.

[31] Chen, S., H. Li, and Y. Jiao, "Dynamic reconstruction of heterogeneous materials and microstructure evolution." *Physical Review E* 92 (2015): 023301. Print.

[32] Chen, S., A. Kirubanandham, N. Chawla, and Y. Jiao, "Stochastic Multi-Scale Reconstruction of 3D Microstructure Consisting of Polycrystalline Grains and Second-Phase Particles from 2D Micrographs." *Metallurgical and Materials Transactions A* 47 (2016): 1-11. Print.

[33] Li, H., S. Singh, N. Chawla, and Y. Jiao, "Direct Extraction of Spatial Correlation Functions from Limited X-ray Tomography Data for Microstructure Quantification." *Materials Characterization* 140 (2016):265-274.Print.

[34] Li, H., P.-E. Chen, and Y. Jiao, "Accurate Reconstruction of Porous Materials via Stochastic Fusion of Limited Bimodal Microstructural Data." *Transport in Porous Media* (2017): 1-18. Print.

[35] Gommes, C., Y. Jiao, and S. Torquato, "Density of states for a specified correlation function and the energy landscape." *Physical review letters* 108 (2012): 080601. Print.

[36] Gommes, C.J., Y. Jiao, and S. Torquato, "Microstructural degeneracy associated with a two-point correlation function and its information content." *Physical Review E* 85 (2012): 051140. Print.

[37] Jiao, Y., F. Stillinger, and S. Torquato, "Geometrical ambiguity of pair statistics: Point configurations." *Physical Review E* 81 (2010): 011105. Print.

[38] Jiao, Y., F.H. Stillinger, and S. Torquato," Geometrical ambiguity of pair statistics. II. Heterogeneous media." *Physical Review E* 82 (2010): 011106. Print.

[39] Jiao, Y., F. Stillinger, and S. Torquato, "A superior descriptor of random textures and its predictive capacity." *Proceedings of the National Academy of Sciences* 106 (2009): 17634-17639. Print.

[40] Cinlar, E. and S. Torquato," Exact determination of the two-point cluster function for one-dimensional continuum percolation." *Journal of statistical physics* 78 (1995): 827-839. Print.

[41] Prager, S., "Interphase transfer in stationary two-phase media." *Chemical Engineering Science* 18 (1963): 227-231. Print.

[42] Torquato, S., "Interfacial surface statistics arising in diffusion and flow problems in porous media." *The Journal of chemical physics* 85 (1986): 4622-4628. Print.

[43] Niezgoda SR, Fullwood DT and Kalidindi SR. "Delineation of the space of 2-point correlations in a composite material system." *Acta Mater* 56 (2008): 5285-92. Print.

[44] Lu B and Torquato S. "Lineal-path function for random heterogeneous materials." *Phys Rev A* 45 (1992): 922-9. Print.

[45] Torquato S, Beasley JD and Chiew YC. "Two-point cluster function for continuum percolation." *J Chem Phys* 88 (1988): 6540-47. Print.

[46] Malmir, H., M. Sahimi, and Y. Jiao, "Higher-order correlation functions in disordered media: Computational algorithms and application to two-phase heterogeneous materials." *Physical Review E* 98 (2018): 063317. Print.

[47] Zachary CE and Torquato S. "Improved reconstructions of random media using dilation and erosion processes." *Phys Rev E* 84 (2011): 056102. Print.

[48] Torquato, S. and Y. Jiao, "Dense packings of the Platonic and Archimedean solids." "*Nature* 460 (2009): 876. Print.

[49] D. Brandon and W.D. Kaplan, *Microstructural Characterization of Materials, 2nd Ed.* Wiley; 2008. Print.

[50] J. Baruchel, P. Bleuet, A. Bravin, P. Coan, E. Lima, A. Madsen, W. Ludwig, P. Pernot and J. Susini, "Advances in synchrotron hard X-ray based imaging." *Comptes rendus-Physique* 9 (2008): 624-641. Print.

[51] J.H. Kinney and M.C. Nichols. "X-ray tomographic microscopy (XTM) using synchrotron radiation." *Annual Review of Materials Science* 22 (1992): 121-152. Print.

[52] A. Kak and M. Slaney. *Principles of Computerized Tomographic Imaging*. SIAM, 1988. Print.

[53] L.A. Feldkamp, L.C. Davis and J.W. Kress, "Practical cone-beam algorithm." *Journal of the Optical Society of America A* 1 (1984): 612-619. Print.

[54] A. Kupsch, A. Lange and M.P. Hentschel, "Enhanced spatial resolution in 2D CT-reconstruction without filtered back projection." *17th World Conference on Nondestructive Testing at Shan*ghai, China (2008). Web.

[55] Pei-En,Chen. Wenxiang, Xu. Nikhilesh Chawla.Yi Ren. Yang Jiao. "Hierarchical n-point polytope functions for quantitative representation of complex heterogeneous materials and microstructural evolution." *Acta Materialia* 179(2019):317-327. . Print.

[56] A. Borbély, F.F. Csikor, S. Zabler, P. Cloetens and H. Biermann," Three-dimensional characterization of the microstructure of a metal-matrix composite by holotomography." *Material Science & Engineering A* 367 (2004): 40-50. Print.

[57] P. Kenesei, H. Biermann and A. Borbély, "Structure-property relationship in particle reinforced metal-matrix composites based on holotomography." *Scripta Materialia* 53 (2005): 787-791. Print.

[58] Jiao, Y., F. Stillinger, and S. Torquato, "Modeling heterogeneous materials via two-point correlation functions: Basic principles." *Physical Review E* 76 (2007): 031110. Print.

[59] Pei-En, Chen. Wenxiang, Xu. Yi, Ren. and Yang, Jiao. "Probing information content of hierarchical n-point polytope functions for quantifying and reconstructing disordered systems." *Physical Review E* 102(2020):013305. Print.

[60] Jiao, Y., F. Stillinger, and S. Torquato, "Modeling heterogeneous materials via two-point correlation functions. II. Algorithmic details and applications." *Physical Review E* 77 (2008): p. 031135. Print.

[61] Yeong CLY and Torquato S. "Reconstructing random media." *Phys Rev E* 57(1998): 495-506. Print.

[62] Yeong CLY and Torquato S. "Reconstructing random media II. Three-dimensional media from two-dimensional cuts." *Phys Rev E* 58 (1998): 224-33. Print.

[63] Roberts AP. "Statistical reconstruction of three-dimensional porous media from two-dimensional images." *Phys Rev E* 56 (1997): 3203-12. Print.

[64] Fullwood DT, Niezgoda SR and Kalidindi SR. "Microstructure reconstructions from 2-point statistics using phase-recovery algorithms." *Acta Mater* 56 (2008): 942-48. Print.

[65]Tahmasebi P and Sahimi M. "Cross-correlation function for accurate reconstruction of heterogeneous media." *Phys Rev Lett* 110 (2013): 078002. Print.

[66] Kirkpatrick S, Gelatt CD and Vecchi MP. "Optimization by simulated annealing." *Science* 220 (1983): 671-80. Print.

[67] D. Li, G. Saheli, M. Khaleel and H. Garmestani, "Quantitative prediction of effective conductivity in anisotropic heterogeneous media using two-point correlation functions." *Computational Materials Sciance* 38 (2006): 45-50. Print.

[68] A. Mikdam, A. Makradi, S. Ahzi, H. Garmestani, D. Li and Y. Remond, "Effective conductivity in isotropic heterogeneous media using a strong-contrast statistical continuum theory." *Journal of the Mechanics and Physics of Solids* 57 (2009): 76-86. Print.

[69] M. Safdari, M. Baniassadi, H. Garmestani and M.S. Al-Haik, "A modified strong-contrast expansion for estimating the effective thermal conductivity of multiphase heterogeneous materials." *Journal of Applied Physics* 112 (2012): 114318. Print.

[70] A. Mikdam, R. Belouettar, D. Fiorelli, H. Hu and A. Makradi, "A tool for design of heterogeneous materials with desired physical properties using statistical continuum" Materials Science and Engineering A 564(2013): 493-500. Print.

[71] S. Torquato, "Exact expression for the effective elastic tensor of disordered composites." *Physical review letters* 79 (1997): 681. Print.

[72] S. Torquato, "Effective stiffness tensor of composite media—I. Exact series expansions." *Journal of the Mechanics and Physics of Solids* 45 (1997): 1421-1448. . Print.

[73] Gommes, C.J., Y. Jiao, A.P. Roberts, and D. Jeulin," Chord-length distributions cannot generally be obtained from small-angle scattering." *Journal of Applied Crystallography* 53 (2020):127-132. Print.

[74] H. Xu, M.S. Greene, H. Deng, D. Dikin, C. Brinson, W.K. Liu, C. Burkhart,G. Papakonstantopoulos, M. Poldneff, W. Chen, "Stochastic reassembly strategy for managing information complexity in heterogeneous materials analysis and design."*J. Mech. Des* 135 (2013): 101010. Print.

[75] H. Okabe, M.J. Blunt, "Pore space reconstruction using multiple-point statistics." *J. Pet. Sci. Eng.* 46 (2005): 121-137. Print.

[76] Kirkpatrick, S., C.D. Gelatt, and M.P. Vecchi, "Optimization by simulated annealing." *Science* 220 (1983): 671-680. Print.

[77] Hwang, C.-R., "Simulated annealing: theory and applications." *Acta Applicandae Mathematicae* 12 (1988): 108-111. Print.

[78] Torquato, S. and Y. Jiao, "Effect of dimensionality on the continuum percolation of overlapping hyperspheres and hypercubes. II. Simulation results and analyses." *The Journal of chemical physics* 137 (2012): 074106. Print.

[79] Sahimi, M. *Applications of percolation theory*. CRC Press, 1994. Print.

[80] Cang, R., H. Li, H. Yao, Y. Jiao, and Y. Ren, "Improving direct physical properties prediction of heterogeneous materials from imaging data via convolutional neural network and a morphology-aware generative model." *Computational Materials Science* 150 (2018): 212-221. Print.

[81] Cang, R., Y. Xu, S. Chen, Y. Liu, Y. Jiao, and M.Y. Ren, "Microstructure Representation and Reconstruction of Heterogeneous Materials via Deep Belief Network for Computational Material Design." *Journal of Mechanical Design* 139 (2017): 071404. Print.

[82] Kamrava, S., P. Tahmasebi, and M. Sahimi, "Linking morphology of porous media to their macroscopic permeability by deep learning." *Transport in Porous Media* 131 (2020): 427-448. Print.

[83] P. Chaudhari. "Hillock growth in thin films." *J. Appl. Phys.* 45 (1974): 4339-4346. Print.

[84] S. K. Lahiri. "Stress relief and hillock formation in thin lead films." *J. Appl. Phys.* 41 (1970): 3172-3176. Print.

[85] K. C. Cadien, D. L. Losee. "A method for eliminating hillocks in integratedcircuit metallizations," J. *Vac. Sci. Technol. B* 2 (1984): 82-83. Print.

[86] C. Y. Chang, R. W. Vook, Y. C. Lee, I. Hoshi. "Isothermal annealing of hillocks in Al-Cu films." *Thin Solid Films* 181 (1989): 57-63. Print.

[87] M. S. Jackson, L. Che-yu. "Stress relaxation and hillock growth in thin films." *Acta Metall.* 30 (11) (1982): 1993-2000. Print.

[88] S.-J. Hwang, Y.-D. Lee, Y.-B. Park, J.-H. Lee, C.-O. Jeong, Y.-C. Joo. "In situ study of stress relaxation mechanisms of pure Al thin films during isothermal annealing." *Scr.Mater.* 54 (2006): 1841-1846. Print.

[89] M. Powers, B. Derby, E. Raeker, N. Champion, A. Misra. "Hillock formation in codeposited thin films of immiscible metal alloy systems." *Thin Solid Films* 693 (2020): 137692. Print.

[90] R. Raghavan, A. Mukherjee, K. Ankit. "Nanostructural evolution in vapor deposited phase-separating binary alloy films of non-equimolar compositions: Insights from a 3D phase-field approach." *J. Appl. Phys.* 128 (2020): 175303. Print.

[91] L. Vitos, A. V. Ruban, H. L. Skriver, J. Koll_ar. "The surface energy of metals." *Surf. Sci.* 411 (1998): 186-202. Print.

[92] A. Hashibon, C. Elsasser, Y. Mishin, P. Gumbsch. "First-principles study of thermodynamical and mechanical stabilities of thin copper film on tantalum". *Phys. Rev. B* 76 (2007): 1-9. Print.

[93] L. A. Zotti, S. Sanvito, D. D. O'Regan. "A simple descriptor for energetics at fcc-bcc metal interfaces." *Mater. Des.* 142 (2018): 158-165. Print.

[94] B. Derby, Y. Cui, J. Baldwin, A. Misra. "Effects of substrate temperature and depositionrate on the phase separated morphology of co-sputtered, Cu-Mo thin films." *Thin Solid Films* 647 (2018): 50-56. Print

[95] K. Ankit, B. Derby, R. Raghavan, A. Misra, M. J. Demkowicz. "3D phase-field simulations of self-organized composite morphologies in physical vapor deposited phase separating binary alloys." *J. Appl. Phys.* 126 (2019). Print